Magnetic Resonance Techniques for Sensitive Assessment of Microscopic Properties of Muscular and Adipose Tissue

Dissertation

der Mathematisch-Naturwissenschaftlichen Fakultät
der Eberhard Karls Universität Tübingen
zur Erlangung des Grades eines
Doktors der Naturwissenschaften
(Dr. rer. nat.)

vorgelegt von
Günter Steidle
aus Balingen

Tübingen
2012

Tag der mündlichen Qualifikation:	06.11.2012
Dekan:	Prof. Dr. Wolfgang Rosenstiel
1. Berichterstatter:	Prof. Dr. Dr. Fritz Schick
2. Berichterstatter:	Prof. Dr. Klaus Scheffler

Contents

Introduction 1

Summary 2

Zusammenfassung 3

1 Basics of Magnetic Resonance 5

1.1 Spin Dynamics 5

1.1.1 Single Spin 5

1.1.2 Ensemble of Spins 7

1.1.3 Excitation 9

1.1.4 Relaxation 10

1.2 Bloch equations 11

1.3 *In vivo* Magnetic Resonance Imaging 12

1.3.1 Magnetic Field Gradients 13

1.3.2 Slice Selection 13

1.3.3 Spatial Frequency Space 14

1.3.4 MRI Sequences 16

1.4 Contrasts in MRI 16

1.4.1 Relaxation Times 16

1.4.2 Diffusion 18

1.4.3 Diffusion Tensor Imaging 20

1.5 *In vivo* Magnetic Resonance Spectroscopy 21

References 23

2 Magnetic Field Distribution of IMCL and EMCL in Lower Leg Muscles 25

2.1 Introduction 26

2.2 Theory 28

2.3 Methods . . . 30
2.3.1 *In Vitro* Examinations . . . 31
2.3.2 *In Vivo* Examinations . . . 31
2.4 Results . . . 35
2.4.1 *In Vitro* Examinations . . . 35
2.4.2 *In Vivo* Examinations . . . 37
2.5 Discussion . . . 40
References . . . 43

3 Echo Planar Diffusion Tensor Imaging of the Lower Leg Muscles 47
3.1 Introduction . . . 47
3.2 Material and Methods . . . 50
3.2.1 Eddy Current Correction . . . 50
3.2.2 Optimization of Diffusion Preparation . . . 52
3.2.3 Sequence Parameters . . . 55
3.2.4 Measurements . . . 56
3.2.5 Post-Processing . . . 57
3.3 Results . . . 59
3.3.1 Eddy Current Correction . . . 59
3.3.2 Parameter Maps . . . 60
3.3.3 Workload Study . . . 64
3.4 Discussion . . . 65
3.5 Conclusions . . . 70
References . . . 71

4 Diffusion Imaging of Adipose Tissue in the Lower Leg 77
4.1 Introduction . . . 78
4.2 Material and Methods . . . 80
4.2.1 Experimental . . . 80
4.2.2 *In Vitro* Studies . . . 81

4.2.3 *In Vivo* Studies 82
4.2.4 Post-Processing 84
4.3 Results 84
4.4 Discussion and Conclusions 88
References 94

5 General Discussion **99**

Appendix **101**

List of Publications **105**

Danksagungen **111**

Curriculum Vitae **113**

Introduction

> *'... in the winter of our first experiments, just seven years ago, looking on snow with new eyes. There the snow lay around my doorstep - great heaps of protons quietly precessing in the Earth's magnetic field. To see the world for a moment as something rich and strange is the private reward of many a discovery.'*
>
> (Edward M. Purcell, Nobel Lecture, December 11, 1952)

In December 1945, Edward M. Purcell, Henry C. Torrey and Robert V. Pound detected weak radio frequency signals generated by the nuclei of atoms in paraffin wax. Almost simultaneously, Felix Bloch, William W. Hansen, and Martin E. Packard independently performed a different experiment, in which they observed radio signals from the atomic nuclei in water. These two experiments were the birth of the field we now know as nuclear magnetic resonance (NMR). Whereas up to this moment physicists have had only the possibility to get information about atomic nuclei through experiments on exotic states of matter in particle beams or energetic collisions in accelerators, it was now possible to detect atomic nuclei with nothing else but a strong magnet and a couple of homely electronic components. Over the last 50 years NMR has developed into one of the most important techniques for determining the structure and dynamics of molecules.

In the 1970s Paul C. Lauterbur introduced magnetic gradient fields to create a two-dimensional image of his test sample and Sir Peter Mansfield provided imaginative leaps in a series of papers to turn NMR into a useful imaging tool. NMR imaging is particularly useful in medicine, where it has become a non-invasive and non-destructive routine diagnostic tool, especially for conditions of the brain, nervous system, and soft tissues of the body. NMR imaging allows the radiologist to visualize the interior of the human body, without any damaging high-energy radia-

tion. NMR imaging is usually known to the public as *magnetic resonance imaging* (MRI) (omitting the term *nuclear* in order to avoid scaring any patients). In German-speaking areas the term *Kernspinresonanztomographie* or shorter *Kernspintomographie* for MR imaging was originally used, however for the same reason, *Magnetresonanztomographie* has become more and more common in the last years.

Since the 1970s, not only MRI but also *in vivo* NMR spectroscopy (MRS) has been established as a diagnostic tool in medical research providing a wealth of non-invasive, spectroscopic information on metabolites and lipids in healthy or pathological tissue. However, in spite of its great potential, *in vivo* MRS has not gained the same importance in medical diagnostics as MRI due to more challenging, technical aspects concerning, for instance, lower sensitivity *in vivo*, spatial localization, water suppression or spectral overlap leading to a low temporal and spatial resolution in MRS.

Measurement of self-diffusion or Brownian motion of molecules is the target of diffusion weighted (DW) MRI and diffusion tensor imaging (DTI). So far, DW MRI and DTI has mainly been applied to brain tissue for detection of acute ischaemic damage and fibre tracking, respectively. However, both, DW MRI and DTI, gain more and more potential for studying other organ tissue.

Whereas DW MRI has become a powerful tool for non-invasive diagnosis of diffuse diseases as for example liver fibrosis or liver cirrhosis and for diagnosis and grading of tumours, DTI is an instrument to study microarchitecture of skeletal musculature.

Summary

Aim of this work was the development of new methods for a better characterization of tissue by means of MRI. The first chapter deals with the basics of magnetic res-

onance. In the second chapter a method for a better separation of the overlapping intra- and extramyocellular lipid signals in ^{1}H MR spectra by means of the calculation of the magnetic field distribution in the examined tissue area is described. The third chapter reports on echo planar imaging (EPI) adapted and optimized for diffusion weighted imaging of lower leg musculature in order to gain maximal signal and to avoid image distortions caused by eddy currents induced in the scanner by switching gradients for diffusion weighting. The fourth chapter focuses on a method implemented for measurement of diffusion of fat in the lower leg. All major results of this work are discussed in chapter five in a general framework.

Zusammenfassung

Ziel dieser Arbeit war die Entwicklung neuer Methoden zur besseren Charakterisierung von Gewebeeigenschaften mit der Magnetresonanztomographie. Das erste Kapitel dieser Arbeit befasst sich mit den Grundlagen der Magnetresonanz. Im zweiten Kapitel wird eine Methodik vorgestellt, mit der die Magnetfeldverteilung von intra- und extramyozellulären Lipidsignalen aus der menschlichen Unterschenkelmuskulatur bestimmt werden kann zur genaueren Trennung der beiden überlappenden Signale in ^{1}H MR Spektren. Im dritten Kapitel wird eine EPI-Sequenz für Diffusionsmessungen am Unterschenkel für eine maximale Signalausbeute optimiert. Dabei werden zusätzlich die durch das Schalten der zur Diffusionsgewichtung verwendeten Gradienten im Magnetresonanz-Tomographen erzeugten Wirbelströme und die damit verbundenen Bildartefakte minimiert. Im vierten Kapitel wird eine Methodik zur Messung der Diffusion von Fett im menschlichen Unterschenkel beschrieben. Die Ergebnisse dieser Arbeit werden in Kapitel 5 in einem allgemeinen Rahmen diskutiert.

1 Basics of Magnetic Resonance*

1.1 Spin Dynamics

1.1.1 Single Spin

One fundamental principle in quantum mechanics is that the intrinsic angular momentum or *spin I* of elementary particles can only have specific values, namely integer values $(0, 1, 2, \dots)$ or half-integer values $(1/2, 3/2, \dots)$. Particles with half-integer spins are called *fermions*, while particles with integer spins are called *bosons*. For example, protons, neutrons and electrons are fermions with spin $1/2$ and photons are bosons with spin 1.

For nuclei, consisting of protons and neutrons, I cannot simply be deduced by summation of its individual components, but following rules are valid:

(i) For nuclei with an odd mass number, I is half-integral (e.g., ^{1}H, ^{13}C).

(ii) For nuclei with an even mass number and an odd charge number, I is an integral number (e.g., ^{2}H, ^{14}N).

(iii) For nuclei with an even mass number and an even charge number, I is zero (e.g., ^{12}C, ^{16}O).

The operators for the three components of the spin observable $\hat{\boldsymbol{I}}$ are denoted by $\hat{I}_x$, $\hat{I}_y$ and $\hat{I}_z$, and have the cyclic commutation relationships:

$$[\hat{I}_x, \hat{I}_y] = i\hbar\hat{I}_z \ ,$$
$$[\hat{I}_y, \hat{I}_z] = i\hbar\hat{I}_x \ ,$$
$$[\hat{I}_z, \hat{I}_x] = i\hbar\hat{I}_y \ .$$

*The textbooks about nuclear magnetic resonance quoted as references [1–4] were used as sources for this chapter.

If I is the nuclear spin number, then the operator $\hat{\boldsymbol{I}}$ has $2I + 1$ eigenstates $|I, M\rangle$ with

$$\hat{I}_z|I, M\rangle = \hbar M|I, M\rangle \ ,$$

where the azimuthal quantum number M takes one of the $2I+1$ values $M = -I, -I+1, -I+2, \ldots, +I$. For the square angular momentum operator $\hat{\boldsymbol{I}}^2 := \hat{I}_x^2 + \hat{I}_y^2 + \hat{I}_z^2$ it holds

$$\hat{\boldsymbol{I}}^2|I, M\rangle = \hbar^2 I(I + 1)|I, M\rangle \ .$$

In the absence of an external magnetic field, each of the $2I + 1$ states with the same value of I, but different values of M, is *degenerate* that is it has the same energy.

Connected with the spin is a *magnetic moment* $\hat{\mu}$ with $\hat{\boldsymbol{\mu}} = \gamma\hat{\boldsymbol{I}}$ where γ is the *gyromagnetic* ratio, whose value depends on the nucleus. For example for a proton it is $\gamma = 267.522 \times 10^6$ rad·s^{-1}·T^{-1}.

In an external magnetic field the degeneracy is broken and the $2I + 1$ states split into sublevels with different energies depending on M (*Zeemann effect*).

For an external field $\boldsymbol{B}$ with magnitude B_0 and direction along the z-axis the spin Hamiltonian of the magnetic energy $\hat{H}$ is proportional to $\hat{I}_z$:

$$\hat{H} = -\hat{\boldsymbol{\mu}} \cdot \boldsymbol{B} = \boldsymbol{\omega} \cdot \hat{\boldsymbol{I}} = \omega_0 \hat{I}_z$$

and for the energy states it holds

$$\hat{H}|I, M\rangle \ = \hbar\omega_0 M|I, M\rangle$$

with $\boldsymbol{\omega} = -\gamma\boldsymbol{B}$ and the *Larmor frequency* $\omega_0 = -\gamma B_0$.

1.1.2 Ensemble of Spins

Turning from a single spin system to a *spin ensemble*, states are described by *spin density operators* $\hat{\rho}$. Especially the *thermal equilibrium state* $\hat{\rho}_{\mathrm{eq}}$ is given by

$$\hat{\rho}_{\mathrm{eq}} = \frac{\exp\left(-\frac{\hat{H}}{k_B T}\right)}{\mathrm{tr}\left(\exp\left(-\frac{\hat{H}}{k_B T}\right)\right)}$$

(*Boltzmann distribution*), where tr(.) denotes the trace of an operator, or in the *high-temperature approximation* ($|\hbar\omega_0| \ll k_B T$):

$$\hat{\rho}_{\mathrm{eq}} = \frac{1}{2I+1}\left(1 - \frac{\omega_0}{k_B T}\hat{I}_z\right) = \frac{1}{2I+1}\left(1 - \frac{\hat{H}}{k_B T}\right) ,$$

where k_B is the *Boltzmann constant* and T the absolute temperature. Using this approximation and neglecting any interactions between the spins, one obtains for the total magnetization M_0 in the equilibrium state

$$M_0 \cong N\mathrm{tr}(\hat{\rho}_{\mathrm{eq}}\hat{\mu}_z) = \frac{N\gamma^2\hbar^2 I(I+1)B_0}{3k_B T} ,$$

where N is the number of spins in the ensemble, that is there will be a net component of magnetization parallel with B_0 along the $+z$ axis.

The Heisenberg dynamics for an observable $\hat{\mu}$ of the spin ensemble is described by the commutator equation

$$\frac{\mathrm{d}\hat{\mu}}{\mathrm{d}t} = \frac{i}{\hbar}[\hat{H}, \hat{\mu}]$$

with the solution

$$\hat{\mu}(t) = \hat{R}_z(-\omega_0 t)\hat{\mu}\hat{R}_z(\omega_0 t) ,$$

where the complex exponentials of the spin operators

$$\hat{R}_x(\theta) = \exp(-i\theta\hat{I}_x/\hbar) ,$$
$$\hat{R}_y(\theta) = \exp(-i\theta\hat{I}_y/\hbar) ,$$
$$\hat{R}_z(\theta) = \exp(-i\theta\hat{I}_z/\hbar)$$

are called *rotation operators*. They are not only needed to describe the time behaviour of the spin observables (or states in the Schrödinger picture), but also the action of radio frequency pulses on the observables of the spin ensemble (see subsection 1.1.3).

Using the cyclic commutation relationships for the spin operators, the time evolution of the spin operators can be explicitly calculated and is given by:

$$\begin{aligned}
\hat{R}_z(-\omega_0 t)\hat{I}_x\hat{R}_z(\omega_0 t) &= \hat{I}_x\cos(\omega_0 t) - \hat{I}_y\sin(\omega_0 t)\ , \\
\hat{R}_z(-\omega_0 t)\hat{I}_y\hat{R}_z(\omega_0 t) &= \hat{I}_y\cos(\omega_0 t) + \hat{I}_x\sin(\omega_0 t)\ , \\
\hat{R}_z(-\omega_0 t)\hat{I}_z\hat{R}_z(\omega_0 t) &= \hat{I}_z\ .
\end{aligned}$$

That means that the spin observable will precess around the external magnetic field as in the classical case.

In the same manner, for rotations with angle θ about the x-axis or y-axis one obtains the expressions:

$$\begin{aligned}
\hat{R}_x(-\theta)\hat{I}_x\hat{R}_x(\theta) &= \hat{I}_x\ , \\
\hat{R}_x(-\theta)\hat{I}_y\hat{R}_x(\theta) &= \hat{I}_y\cos(\theta) - \hat{I}_z\sin(\theta)\ , \\
\hat{R}_x(-\theta)\hat{I}_z\hat{R}_x(\theta) &= \hat{I}_z\cos(\theta) + \hat{I}_y\sin(\theta)
\end{aligned}$$

or

$$\begin{aligned}
\hat{R}_y(-\theta)\hat{I}_x\hat{R}_y(\theta) &= \hat{I}_x\cos(\theta) + \hat{I}_z\sin(\theta)\ , \\
\hat{R}_y(-\theta)\hat{I}_y\hat{R}_y(\theta) &= \hat{I}_y\ , \\
\hat{R}_y(-\theta)\hat{I}_z\hat{R}_y(\theta) &= \hat{I}_z\cos(\theta) - \hat{I}_x\sin(\theta)\ ,
\end{aligned}$$

respectively.

Changing to the Schrödinger picture, the time evolution of the ensemble states is determined by the commutator equation

$$\frac{\mathrm{d}\hat{\rho}}{\mathrm{d}t} = \frac{i}{\hbar}[\hat{\rho}, \hat{H}]\ .$$

Especially (and only) for a spin-1/2-ensemble the spin density operator can generally be written as

$$\hat{\rho} = \frac{1}{2} - \frac{1}{4}\frac{\hbar\omega_0}{k_B T}\boldsymbol{m}\cdot\hat{\boldsymbol{\sigma}} ,$$

where $\hat{\boldsymbol{\sigma}} = (\hat{\sigma}_x, \hat{\sigma}_y, \hat{\sigma}_z)^{\mathrm{T}}$ are the Pauli spin matrices and $\boldsymbol{m}$ is a unit vector along the direction of the magnetization ($\cdot$ denotes the scalar product of two vectors).

Using the relations $\hat{\boldsymbol{I}} = \frac{\hbar}{2}\hat{\boldsymbol{\sigma}}$ or $\hat{H} = -\frac{\gamma\hbar}{2}\boldsymbol{B}\cdot\hat{\boldsymbol{\sigma}}$, respectively, and the identity

$$[\boldsymbol{m}\cdot\hat{\boldsymbol{\sigma}}, \boldsymbol{B}\cdot\hat{\boldsymbol{\sigma}}] = 2i\boldsymbol{m}\times\boldsymbol{B}\cdot\hat{\boldsymbol{\sigma}} ,$$

it can be shown that from

$$\frac{\mathrm{d}\hat{\rho}}{\mathrm{d}t} = \frac{i}{\hbar}[\hat{\rho}, \hat{H}] ,$$

it follows

$$\frac{\mathrm{d}\boldsymbol{m}}{\mathrm{d}t}\cdot\hat{\boldsymbol{\sigma}} = \gamma\boldsymbol{m}\times\boldsymbol{B}\cdot\hat{\boldsymbol{\sigma}}$$

or

$$\frac{\mathrm{d}\boldsymbol{m}}{\mathrm{d}t} = \gamma\boldsymbol{m}\times\boldsymbol{B} , \tag{1.1}$$

which is in correspondence to the classical description for the precession of a magnetic dipole or more generally the resultant of magnetic dipoles that is magnetization in an external magnetic field B_0.

1.1.3 Excitation

In MRI or MRS magnetization is usually detected via precession. Therefore, the thermal equilibrium has to be disturbed by rotating the longitudinal equilibrium magnetization towards the transverse plane that is by creating *transverse magnetization*.

This can be done by switching on an additional magnetic field $B_1(t)$ for a certain time in the transverse plane oscillating with a radio frequency (RF) ω in the range of the Larmor frequency ω_0 (see Eq. (1.1)). During application of this so called *RF*

pulse, the magnetization will precess about B_0 and B_1 in a rather complex manner in the laboratory frame (see Fig. 1). In a *rotating frame* oscillating about B_0 with

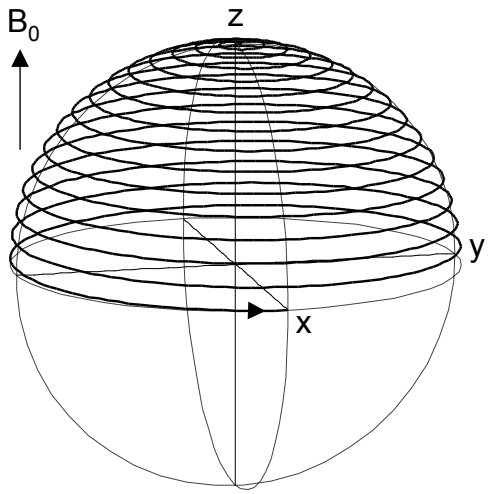

Figure 1: *Excitation of magnetization in the laboratory frame. The initial longitudinal magnetization precesses about the resultant of B_0 and the RF field B_1, which rotates in the xy-plane. RF field B_1 and RF duration were calibrated to turn M_0 by 90°.*

frequency ω_0 instead of the laboratory frame, the description of this motion can be simplified, since B_1 is static in this frame.

Especially for the *on-resonant* case (i.e., $\omega = \omega_0$), the magnetization simply rotates about B_1 with frequency $\omega_1 = -\gamma B_1$ in the rotating frame.

1.1.4 Relaxation

If the sample is rapidly brought into an external field or an applied RF pulse is switched off, the spin ensemble approaches the new equilibrium state not instantaneously, but macroscopic magnetization only gradually changes through interactions of the spins with rapidly fluctuating microscopic magnetic fields caused by thermal motion of charges in the environment.

Therefore, spins will be permanently excited and deexcited exchanging energy with the thermal surroundings.

The build up curve of the macroscopic magnetization belonging to the new equilibrium state is usually approximately exponential with a characteristic time constant

$T1$ and

$$M_z(t) = M_{\text{eq}} + (M_0 - M_{\text{eq}}) \cdot \exp(-t/T1) \ .$$

This process that is returning to thermal equilibrium in an exponential manner, is called *longitudinal relaxation* and $T1$ is the *spin-lattice relaxation constant* or *longitudinal relaxation time constant*.

The relaxation time constant $T1$ depends on the strength of the static magnetic field B_0, the nucleus and the sample, including parameters such as temperature, electrical conductivity and viscosity in case of fluids. Typical values of $T1$ are in the range of msec to sec.

Fluctuating microscopic magnetic fields are not only responsible for relaxation of the macroscopic (longitudinal) magnetization, but also for relaxation of the transverse magnetization. Immediately after excitation, the magnetic dipoles are all in phase or *coherent*. However, due to the fluctuations, the single precessing spins gradually get out of phase and after a certain time, coherence of the spin states will be nearly completely destroyed. This process is described by the equation

$$M_{\text{tr}}(t) = M_{\text{tr},0} \cdot \exp(-t/T2) \ ,$$

where $T2$ is the *spin-spin relaxation time constant* or *transverse relaxation time constant*. Theoretically, it holds $T2 \leq 2T1$, but in most practical cases $T2$ is smaller than $T1$ [1].

1.2 Bloch equations

As shown in the former section, magnetization $\vec{M}$[†] in an external magnetic field $\vec{B}$ will precess around the direction of $\vec{B}$. Combining precession and relaxation

[†]In the following sections, vectors will be denoted by arrows instead of bold characters.

processes leads to the famous *Bloch equations* [5]:

$$\frac{\mathrm{d}\vec{M}}{\mathrm{d}t}(t) = \hat{A}(t)\vec{M}(t) + R1 \cdot \vec{M}_{\mathrm{eq}}$$

with

$$\hat{A}(t) := \begin{pmatrix} -R2 & \gamma B_z(t) & -\gamma B_y(t) \\ -\gamma B_z(t) & -R2 & \gamma B_x(t) \\ \gamma B_y(t) & -\gamma B_x(t) & -R1 \end{pmatrix} ,$$

$\vec{M}_{\mathrm{eq}} := (0, 0, M_{\mathrm{eq}})^{\mathrm{T}}$, $R1 := 1/T1$ and $R2 := 1/T2$.

In the rotating frame this can be rewritten as

$$\hat{A}(t) = \begin{pmatrix} -R2 & \gamma\Delta\omega(t) & -\gamma b_y(t) \\ -\gamma\Delta\omega(t) & -R2 & \gamma b_x(t) \\ \gamma b_y(t) & -\gamma b_x(t) & -R1 \end{pmatrix}$$

where $\Delta\omega$ is the offset frequency and $\vec{b}(t) = (b_x(t), b_y(t))^T$ the RF pulse in the rotating frame representation.

1.3 *In vivo* Magnetic Resonance Imaging

In 1973, Lauterbur [6] reported the first generation of a proton spin density image using *magnetic field gradients* and in the same year Mansfield and Granell [7] independently showed the relationship between the spin density and the MR signal acquired in the presence of magnetic field gradients.

Nowadays, MRI has proven to be an important and powerful tool in diagnostic radiology allowing the non-invasive and non-destructive generation of images of living biological objects. Especially the excellent soft tissue contrast and the fact that it works without ionizing radiation turn MRI into an indispensable imaging modality besides computed tomography (CT), single-photon emission computed tomography (SPECT) or positron emission tomography (PET).

1.3.1 Magnetic Field Gradients

The essential concept of any MRI experiment is the general resonance condition $\omega_0 = -\gamma B_0$ in combination with magnetic field gradients. The resonance frequency is made position-dependent with aid of additional, linear magnetic field gradients

$$B_z(\vec{r}) = \vec{r} \cdot \vec{G} \,,$$

where the quantities

$$G_x = \frac{\partial B_z}{\partial x}, G_y = \frac{\partial B_z}{\partial y}, G_z = \frac{\partial B_z}{\partial z}$$

are constant in each case. Therefore, the resonance condition

$$\omega(\vec{r}) = -\gamma B(\vec{r}) = -\gamma B_0 - \gamma \vec{r} \cdot \vec{G}$$

becomes dependent on position $\vec{r}$.

1.3.2 Slice Selection

Generating MR images by encoding with magnetic field gradients, it has to be distinguished between 3D and 2D techniques. 3D MR imaging by encoding all three directions could be a time-consuming procedure. Therefore, one often reduces the problem to two dimensions by selecting a spatial slice out of a three-dimensional object.

To excite only the slice with a slice position z_0 and thickness Δz (without loss of generality in *xy*-plane), an RF pulse exciting only a selective frequency range $\Delta\omega$ is simultaneously applied with a magnetic field gradient G_{SL} or G_z. The slice thickness is then given by

$$\Delta z = \frac{\Delta\omega}{\gamma G_z} \quad .$$

With a fixed gradient strength and a constant RF pulse, the slice position is determined by the transmitter frequency according to

$$\omega(z_0) = -\gamma B_0 - \gamma z_0 G_z \quad .$$

1.3.3 Spatial Frequency Space

In general, the observed magnetization $M_{\mathrm{tr}}(t)$ after the time t and in the presence of magnetic field gradients $\vec{G}(t)$ (ignoring transverse relaxation) is given by

$$M_{\mathrm{tr}}(t) = \int_{-\infty}^{+\infty} \rho_{\mathrm{s}}(\vec{r}) \cdot \exp\left(-2\pi i \vec{k}(t) \cdot \vec{r}\right) \mathrm{d}^3 r \quad \text{with}$$

$$\vec{k}(t) = \gamma \int_0^t \vec{G}(t')\mathrm{d}t' \ .$$

The vector space spanned by the wave numbers $\vec{k} = (k_x, k_y, k_z)^{\mathrm{T}}$ is called *spatial frequency space* or *k-space*. Particularly, the observed time-domain signal M_{tr} equals the Fourier transformation of the spin density ρ_{s}.

In 2D MR imaging, k-space is also reduced to two dimensions (e.g., the xy-plane), and the trajectory of $\vec{k}(t)$ is usually realized by applying two distinct gradients (see Fig. 2):

- a *phase-encoding* gradient G_{PH} or $G_y = \left(n_y - \frac{N_y - 1}{2}\right) \Delta G_y$, $n_y = 0, \ldots, N_y - 1$ of duration τ_y incremented in subsequent acquisitions by ΔG_y before signal recording and
- a *frequency encoding* gradient G_{RO} or G_x of duration $T_{\mathrm{aq}} = N_x \Delta t$ applied during signal recording with step size Δt between subsequent readout points (spin-warp imaging).

Since the recorded signal is discretised, the transverse magnetization reads as

$$M_{\mathrm{tr}}(m_x, m_y) = \int_0^{L_x} \int_0^{L_y} \rho_{\mathrm{s}}(\vec{r}) \cdot \exp\left(-2\pi i (m_x \Delta k_x \cdot x + m_y \Delta k_y \cdot y)\right) \mathrm{d}x\mathrm{d}y \ ,$$

where

$$\Delta k_x = \Delta k_{\mathrm{RO}} = \gamma G_x \Delta t \ ,$$
$$\Delta k_y = \Delta k_{\mathrm{PH}} = \gamma \Delta G_y \tau_y$$

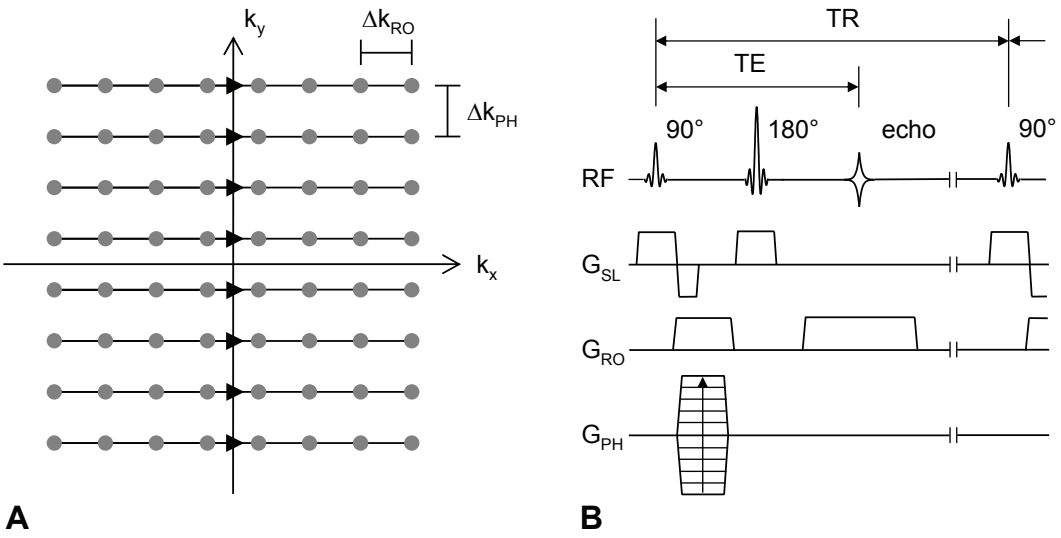

Figure 2: *K-space trajectory (A) and sequence diagram for spin-warp imaging.*

and L_x and L_y are the dimensions of the excited slice (*field of view*) in x- and y-direction, respectively. With N_x representing the number of readout points and N_y the number of phase encoding steps, a 2D inverse discrete Fourier transformation of M_{tr},

$$\hat{\rho}_{\mathrm{s}}(n_x, n_y) = \frac{1}{N_x N_y} \sum_{m_x=0}^{N_x-1} \sum_{m_y=0}^{N_y-1} M_{\mathrm{tr}}(m_x, m_y) \cdot \exp\left(2\pi i (m_x n_x / N_x + m_y n_y / N_y)\right)$$

yields the MR pixel image, where for the pixel size or the resolution of the MR image, it holds

$$\Delta x = \frac{1}{\gamma G_x T_{\mathrm{aq}}} ,$$
$$\Delta y = \frac{1}{\gamma N_y \Delta G_y \tau_y}$$

and

$$L_x = N_x \Delta x = 1/\Delta k_x ,$$
$$L_y = N_y \Delta y = 1/\Delta k_y$$

according to the *Nyquist sampling theorem*.

1.3.4 MRI Sequences

In Fig. 2 the basic design of the conventional spin-warp spin-echo sequence with the corresponding *k*-space trajectory is depicted. Disadvantage of this sequence is the rather long acquisition time due to the necessary waiting time for equilibrium between subsequent excitations. Therefore, often more advanced and faster trajectories are chosen to shorten the time at which the transverse magnetization is sampled. This can be reached by forming more than one echo from a single excitation using the *Turbo Spin-Echo* (TSE) method for T2-weighted scans as shown in Fig. 3A. With TSE, measuring time can be shortened by the so called *turbo factor* denoting the number of spin-echoes generated after single excitation. However, there are also drawbacks of TSE. Imperfections in phase relation of the pulses or unbalanced readout gradients can lead to pronounced ghost artefacts in phase encoding direction. Furthermore, several fast applied refocusing pulses may drastically increase *specific absorption rate* (SAR) leading to unwanted tissue heating.

Instead of refocusing pulses for generating several (spin-)echoes after excitation, alternating gradients can be applied during readout to create several gradient echoes when moving around in *k*-space. This principle is used in *Echo Planar Imaging* (EPI) where only one pulse for excitation is applied and afterwards the whole *k*-space is sampled (see Fig. 3B). EPI is a very fast MRI sequence, sampling whole *k*-space in a few milliseconds, but is very prone to field inhomogeneities causing severe ghosts blurring and ringing.

1.4 Contrasts in MRI

1.4.1 Relaxation Times

One of the most demanding tasks in *in vivo* MRI is the creation of an appropriate contrast to differentiate areas of interest concerning structure and function of the

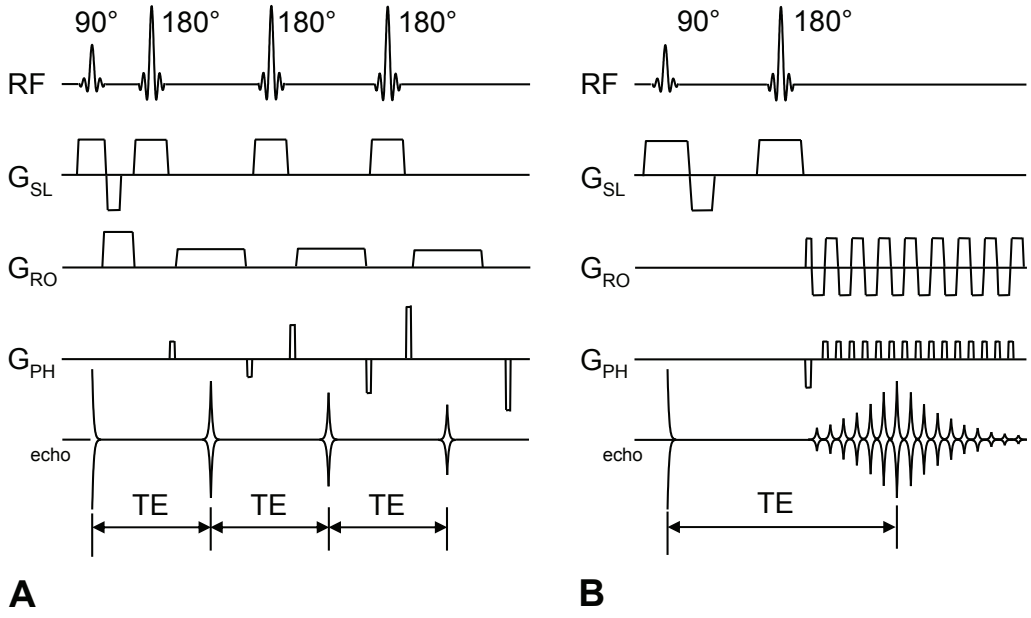

Figure 3: *Sequence diagram of a turbo spin-echo (TSE) sequence (A) and an echo planar imaging (EPI) sequence (B).*

examined tissue. The most common contrast parameters used in clinical routine are spin density ρ_s, longitudinal relaxation time $T1$, and transverse relaxation time $T2$. Sequence parameters as the echo time TE and the repetition time TR can be varied, and transverse magnetization is always a function of these tissue parameters. For example for a common spin echo sequence, transverse magnetization at echo time TE equals

$$M_{tr}(TR, TE) = M_{eq}(1 - \exp(-TR/T1)) \cdot \exp(-TE/T2) \ .$$

Further contrasts can be generated by *magnetization transfer* from protons in biological structures such as proteins and membranes, which are not directly visible in *i*n vivo MRI due to their very short relaxation times, to protons of mobile water. Another important contrast parameter is the *apparent diffusion coefficient* (ADC), which describes self-diffusion of water or other molecules in biological tissue and its restriction by the tissue's microstructure.

1.4.2 Diffusion

Self-diffusion or Brownian motion of water molecules is the target of *diffusion weighted imaging* (DWI). Prime example for application of DWI is detection of acute ischaemic damage in the brain having a strong impact in the management of stroke, although water mobility in tissue is a very complex process. A detailed mathematical framework of free Brownian motion was first published by Albert Einstein in 1905 [8] leading to the two equations

$$\left\langle \Delta r^2 \right\rangle = 6D\Delta t \ , \tag{1.2}$$

where $\left\langle \Delta r^2 \right\rangle$ represents the mean square displacement of a particle within a time interval Δt and D the (self) diffusion coefficient, and

$$D = \frac{k_B T}{6\pi\eta R_H} \ , \tag{1.3}$$

the Stokes-Einstein equation, where k_B is Boltzmann's constant, T the absolute temperature, η the viscosity and R_H the hydrodynamic radius.

Mathematically, self-diffusion is described by the partial differential equation

$$\frac{\partial P}{\partial t} = \nabla \cdot (D \nabla P) \ ,$$

where $P(\vec{r}, t)$ is the probability density to find a particle, which was at the origin for $t = 0$, at location $\vec{r}$ and time t.

In *in vivo* DWI not the self-diffusion coefficient D itself, but the restriction of diffusion by cellular and subcellular impediments inside the cells and outside by cellular compartmentalization or macromolecules is measured. In general water molecules are not allowed to diffuse freely *in vivo*. To confirm this statement, consider the scale of molecular displacement over a given time interval Δt of for example 30 msec in pure water. For a body temperature of 37°C, self-diffusion coefficient D of water is approximately $D = 3 \times 10^{-3}$ mm^2/s leading to an average displacement of 30 μm, which is distinctly greater than cellular dimensions of a few microns.

A water molecule or spin that moves along a path $\vec{r}(t)$ in a gradient field $\vec{G}(t)$ accumulates phase ϕ according to

$$\phi(t) = -\gamma \int_0^t \vec{r}(t') \cdot \vec{G}(t') \mathrm{d}t' \ .$$

For an ensemble of spins having random trajectories caused by free self-diffusion, phases will have a Gaussian distribution. Signal attenuation S/S_0 for a *pulsed field gradient* (PFG) waveform for DWI (see Fig. 4) is given by

$$S(b)/S_0 = \langle \exp(i\phi) \rangle = \exp\left(-\frac{1}{2}\left\langle \phi^2 \right\rangle\right) = \exp(-bD), \quad \text{where}$$

$$b = \gamma^2 G^2 \left[\delta^2 \left(\Delta - \frac{1}{3}\delta\right) + \frac{1}{30}\varepsilon^3 - \frac{1}{6}\delta\varepsilon^2\right]$$

is the so called *b-value* (G, Δ, δ and ϵ are explained in Fig. 4). By means of this signal attenuation determined for different b-values, the diffusion coefficient D can be calculated.

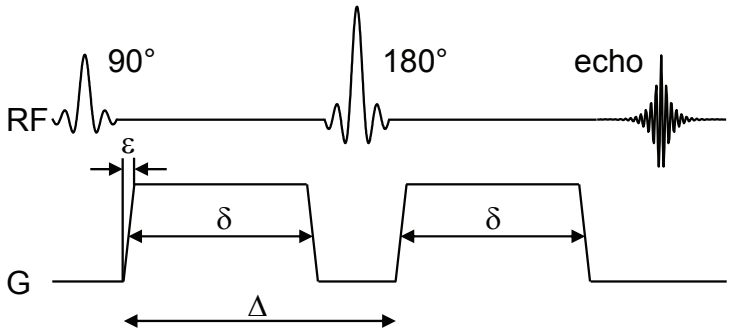

Figure 4: *Standard pulsed field gradient (PFG) waveform for diffusion weighted imaging. Due to the distribution of phases in a spin ensemble caused by self-diffusion, transverse magnetization will not be fully rephased by the field gradient after the 180°-pulse leading to a signal attenuation.*

1.4.3 Diffusion Tensor Imaging

According to Eq. 1.2, isotropic diffusion can geometrically be described by a sphere defined by

$$x^2 + y^2 + z^2 = 6D\Delta t \ .$$

Defining

$$\hat{D}_{\text{iso}} = \begin{pmatrix} D & 0 & 0 \\ 0 & D & 0 \\ 0 & 0 & D \end{pmatrix} ,$$

this equation can be rewritten as

$$\vec{r}^{\,\text{T}} \cdot \hat{D}_{\text{iso}}^{-1} \vec{r} = 6\Delta t \ ,$$

where $\vec{r}$ is the position vector. For a more quantitative description of restricted or hindered diffusion, the scalar diffusion coefficient D is replaced by a general symmetric positive definite tensor $\hat{D}$

$$\hat{D} = \begin{pmatrix} D_{xx} & D_{xy} & D_{xz} \\ D_{yx} & D_{yy} & D_{yz} \\ D_{zx} & D_{zy} & D_{zz} \end{pmatrix} \quad .$$

Geometrically, $\hat{D}$ describes an arbitrarily oriented (elongated) ellipsoid by the equation (see Fig. 5)

$$\vec{r}^{\,\text{T}} \cdot \hat{D}^{-1} \vec{r} = 6\Delta t \quad .$$

The eigenvalues λ_1, λ_2, λ_3 and eigenvectors $\vec{e}_1$, $\vec{e}_2$, $\vec{e}_3$ of $\hat{D}$ define the principal directions of the ellipsoid and the corresponding equatorial radii $A = \sqrt{6\lambda_1\Delta t}$, $B = \sqrt{6\lambda_2\Delta t}$ and $C = \sqrt{6\lambda_3\Delta t}$ considering the possible anisotropy of diffusion *in vivo*.

In case of orientation dependent eigenvalues, signal attenuation is also anisotropic or orientation-dependent. If $\vec{n}$ is the direction of the diffusion gradient $\vec{G} = G\vec{n}$, it holds

$$S(b, \vec{n})/S_0 = \exp(-bD_{\vec{n}}), \quad \text{where} \quad D_{\vec{n}} = \vec{n} \cdot \hat{D}\vec{n} \ .$$

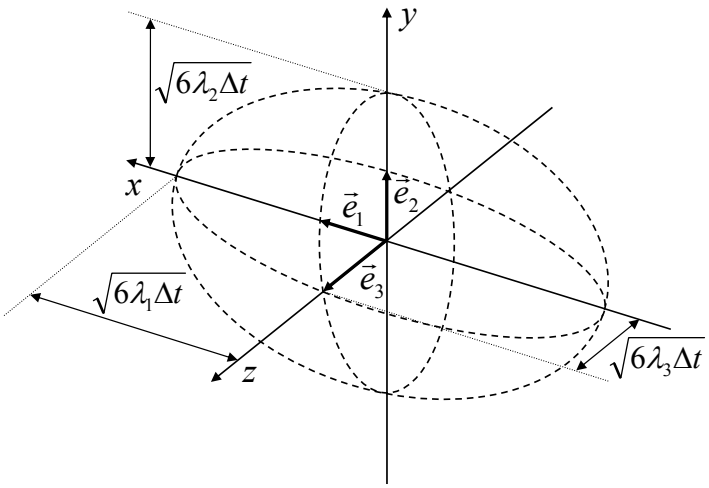

Figure 5: *Diffusion ellipsoid.*

To fully determine the diffusion tensor with DWI measurements, (at least) six non-collinear diffusion directions have to be chosen[‡].

1.5 *In vivo* Magnetic Resonance Spectroscopy

In principle magnetic resonance spectroscopy is feasible on any nucleus with a magnetic moment, whereas for *in vivo* applications the most interesting nuclei are hydrogen (^{1}H), carbon (^{13}C), phosphorus (^{31}P) and sodium (^{23}Na), whereas the latter nucleus is also used for MRI. Each of this nuclei can provide different information about various metabolic processes in biological tissues. However, the proton nucleus is the most sensitive nucleus for MR concerning high MR sensitivity and high natural abundance.

Before any localization technique for *in vivo* MRS can be applied, the spatial boundaries and the distribution of different tissues under investigation have to be known. For this purpose, the techniques of *magnetic resonance imaging* are applied, as described in the foregoing subsection.

[‡]An introduction to *in vivo* MR diffusion imaging in the body can be found in [9].

For an adequate tissue characterization, spatial localization techniques have to be employed to gain only MR signal out of a special region of interest. Two of the most common localization or *single-voxel* techniques are the PRESS (Point RESolved Spectroscopy) technique and the STEAM (Stimulated Echo Acquisition Mode) technique, both based on the principle of slice selection by frequency-selective RF pulses in the presence of magnetic field gradients (see Fig. 6).

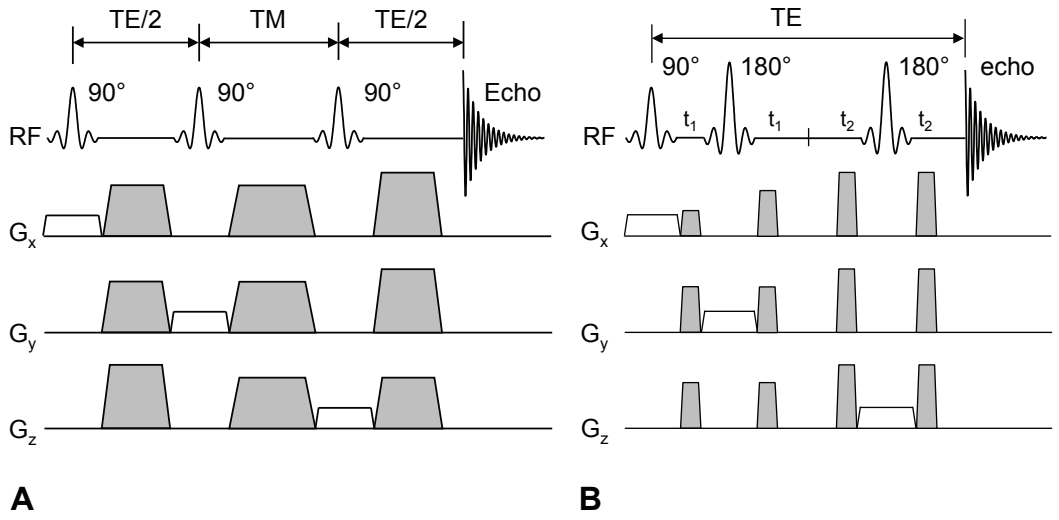

Figure 6: *Sequence diagram of a STEAM sequence (A) and of a PRESS sequence (B). In both sequences spoiler gradients (grey shaded) of sufficient strength are necessary to remove unwanted coherences and to achieve accurate localization.*

In place of the many textbooks concerning basics of MR, MR imaging and MR spectroscopy, an assortment of four excellent books will be quoted as references, which were also used as sources for this Chapter [1–4].

References

[1] Levitt, M. H.: *Spin dynamics: basics of nuclear magnetic resonance*. John Wiley & Sons Ltd., 2001.

[2] de Graaf, R.A.: *In* vivo *NMR spectroscopy*. John Wiley & Sons Ltd., 1998.

[3] Haacke, E. M.: *Magnetic resonance imaging: physical principles and sequence design*. John Wiley & Sons Ltd., 1999.

[4] Vlaardingerbroek, M. T. and J. A. den Boer: *Magnetic resonance imaging: theory and practice*. Springer-Verlag, third edition, 2003.

[5] Bloch, F.: *Nuclear Induction*. Phys. Rev., 70:460–474, 1946.

[6] Lauterbur, P. C.: *Image formation by induced local interactions: examples employing nuclear magnetic resonance*. Nature, 242:190–191, 1973.

[7] Mansfield, P. and P. K. Grannell: *NMR 'diffraction' in solids?* J. Phys. C, 6:L422–L426, 1973.

[8] Einstein, A.: *Über die von der molekularkinetischen Theorie der Wärme geforderte Bewegung von in ruhenden Flüssigkeiten suspendierten Teilchen*. Annalen der Physik, 322(8):549–560, 1905.

[9] Koh, D. M. and H. C. Thoeny (editors): *Diffusion weighted MR imaging Applications in the Body*. Springer-Verlag, 2010.

2 Magnetic Field Distribution of IMCL and EMCL in Lower Leg Muscles*

In skeletal muscles intra- (IMCL) and extramyocellular lipids (EMCL) are stored in different geometric formations and experience different magnetic field strengths due to geometrical susceptibility effects. The effect is strong enough to at least partly separate IMCL- and EMCL-contributions in ^{1}H MR spectroscopy, despite IMCL and EMCL consist of the same substances. The assessment of IMCL stores in skeletal musculature by ^{1}H MR spectroscopy plays an important role for studying physiological and pathological aspects of lipid metabolism. Therefore, a method using mathematical tools of Fourier analysis is developed to obtain the magnetic field distribution (MFD) from the measured spectra by deconvolution. A reference lipid spectrum is required, which can be recorded in tibial yellow bone marrow. It is shown that the separation of IMCL contributions can be performed more precisely – compared to other methods – based on the MFD. Examples of deconvolution in model systems elucidate this principle. Applications of the proposed approach on *in vivo* examinations in muscle soleus and muscle tibialis anterior are presented. Fitting the IMCL part of the MFD by a Gaussian lineshape with a linewidth kept fixed with respect to the linewidth of creatine and with the assumption of a smooth but not necessarily symmetrical shape for the EMCL part, the only free fit parameter, the amplitude of the IMCL part, is definite and subtraction leads to the EMCL part in the MFD. This procedure is especially justified for the muscle soleus showing a severely asymmetrical distribution, which might lead to a marked overestimation of IMCL using common line fitting procedures.

*This Chapter was adapted from: Steidle G, Machann J, Claussen CD, Schick F. Separation of intra- and extramyocellular lipid signals in proton MR-spectra by determination of their magnetic field distribution. J Magn Reson 2002;154:228-235.

2.1 Introduction

Volume selective ^{1}H MR spectroscopy has been shown to be a non-invasive tool, which allows to assess the lipid content of human skeletal muscles [1–3]. The signal consists of components from intramyocellular (IMCL) and extramyocellular lipids (EMCL) leading to a relatively complex signal pattern in the recorded spectra [2–4]. Since IMCL are actively involved in lipid metabolism with turnover rates of several hours for substrate utilization, an accurate assessment of the IMCL signal by ^{1}H MR spectroscopy is desirable for studying physiological and pathological aspects of lipid metabolism. In clinical studies, a negative correlation between IMCL content and insulin resistance was found recently [5–7]. Since decreased insulin sensitivity is an important predictor for type 2 diabetes, ^{1}H MR measurements of IMCL will be a helpful tool for a primary recognition. Additionally, IMCL serve as an energy depot for workload depending on duration and intensity of exercise [3, 8, 9] and for this reason the regulation of IMCL is also of interest in sports medicine.

IMCL show relatively homogeneous spatial distribution in musculature, whereas EMCL are more inhomogeneously located in the septa between the muscle bundles [10]. The latter are relatively inert in lipid metabolism and can only serve as a long-term fat depot. IMCL are settled as little droplets with a diameter of about 0.5 μm in close position to mitochondria in the cytoplasm of myocytes [3]. Since the droplets have a rather spherical shape with a homogeneous distribution throughout muscle fibres, signals of IMCL are independent of muscle orientation relative to the magnetic field and show a regular symmetrical distribution of the experienced magnetic field. In contrast, different geometrical arrangements of EMCL relative to the magnetic field lead to orientation dependent anisotropic susceptibility effects [3, 11, 12]. The EMCL compartments are mainly determined by the more tubular structures of muscle fibres. For this reason, the compartments of EMCL can show a rather inhomogeneous and even asymmetrical distribution of the magnetic field due to a tube-like geometry combined with anisotropic susceptibility effects as it

was also reported regarding geometric models of trabecular bone [13] and lung tissue [14].

The lipid signal positions in spectra from musculature depend on both, the chemical shifts and the local magnetic field distribution caused by bulk magnetic susceptibility (BMS) effects. The difference of the mean Larmor frequency in IMCL and EMCL compartments is relatively small and amounts to approximately 0.15 ppm for the muscle soleus (SOL) and 0.25 ppm for the muscle tibialis anterior (TA). It depends on the muscle fibre orientation relative to the static magnetic field and is maximal in the case of the orientation of the fibres is parallel to the magnetic field [3, 4]. The superposition of the IMCL and EMCL signal components in the spectra hinders an accurate quantitative evaluation of both portions. Usually, strategies to assess IMCL signals comprise integration of the spectral signal intensity within fixed frequency ranges or signal fitting with Gaussian and/or Lorentzian lineshapes. However, both methods will be critical for a pronounced asymmetrical field distribution.

The aim of the present study was to develop a new approach using the fact that the muscular lipid signals can be described as the convolution between the magnetic field distribution (MFD) of the lipid compartments and a characteristic line pattern of lipids describing chemical shift modulations. This approach is reasonable, because from a biochemical point of view it is clear that the mentioned characteristic line pattern of lipids must exist: IMCL, EMCL and adipose tissue as subcutaneous fat tissue or tibial bone marrow lipids (BM) are known to consist mainly of the same composition of fatty acid triglycerides [15–17]. For this reason, spectra of yellow bone marrow recorded with identical measurement parameters can be used to assess the required characteristic line pattern of lipids. Mathematical tools of Fourier analysis were used to calculate the underlying MFD of lipids in skeletal musculature. The aim of this work is to show that an easier interpretation and determination of IMCL and EMCL components in the pattern of the MFD is possible rather than in

the more complicated lipid signals in the recorded spectra.

2.2 Theory

In contrast to aqueous solutions with one single compartment, tissues show several intra- and extracellular compartments with variable geometry, volume, concentrations of substances and magnetic susceptibilities. The frequency shifts in a spectrum recorded *in vivo* depend, firstly on the characteristic chemical shifts and secondly on the distribution of the magnetic field experienced by the substance of interest. If it were possible to record a spectrum of the substance in a homogeneous magnetic field, the frequency shifts in the spectrum would only depend on the chemical shifts and the linewidth would be minimal. These minimal linewidths $\Delta\omega_{\text{min}}$ are determined by $\Delta\omega_{\text{min}} = 1/(\pi \cdot T2)$. This theoretical spectrum of the substance expressing only chemical shift modulations will be called Θ. In terms of Fourier analysis, the recorded spectral signals of a substance in tissue (E) can be written as the convolution ($*$) between the magnetic field distribution (MFD) experienced by the substance of interest and Θ:

$$E = \text{MFD} * \Theta \quad . \tag{2.1}$$

In contrast to Θ, expressing the chemical shift modulations, the MFD describes frequency shifts caused by BMS effects. If it is possible to determine Θ indirectly by recording a reference spectrum (R) out of a compartment with the same chemical composition as the substance of interest but with a rather homogeneous magnetic field distribution, calculation of the MFD from a recorded spectrum of a substance will be feasible. Since *in vivo* conditions do not provide an ideal homogeneous field, the linewidths in R are broadened and a normal distribution (G) for variation of the magnetic field is assumed. This leads to

$$R = G * \Theta \quad . \tag{2.2}$$

The inverse Fourier transform of G again yields a Gaussian function (up to a scal-

ing factor) with time constant T_g depending on the line broadening in R and the quality of shimming. T_g can numerically be determined with aid of T2 and the measured linewidth $\Delta\omega$ of a dominating peak in a reference spectrum in homogeneous compartments (e.g., the methylene group ($(-CH_2)_n$) of lipids in BM). Using the well-known convolution theorem of Fourier analysis that is convolution in the frequency domain corresponds to multiplication in time domain, inverse Fourier

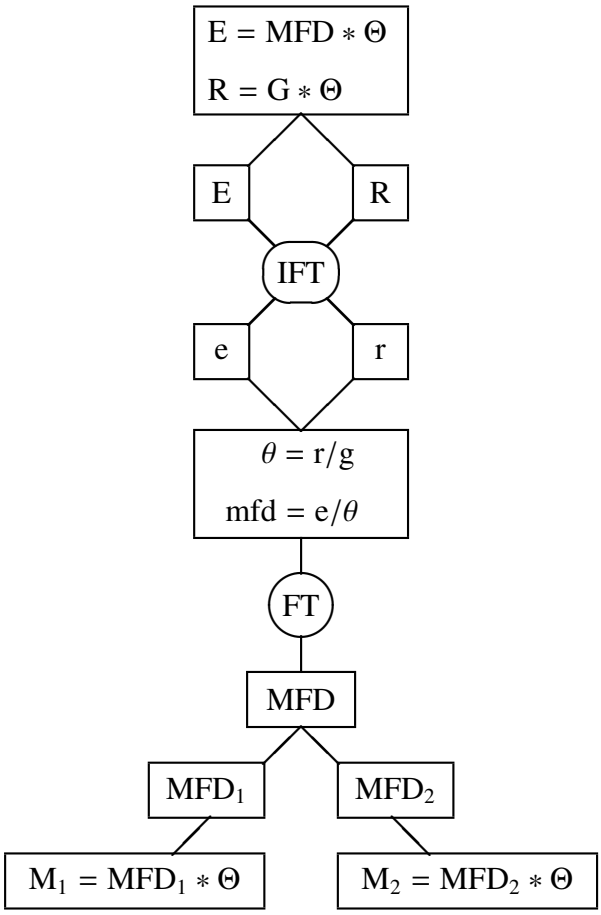

Figure 1: *Scheme of the procedure for calculation of the magnetic field distribution. MFD: magnetic field distribution, E: lipid signals for evaluation, R: reference lipid signals, G: Gaussian distribution, Θ: theoretical lipid signals, FT: Fourier transform, IFT: inverse Fourier transform, MFD_1 and MFD_2 portions of MFD, M_1 and M_2 portions of M*

transformation of Eq. (2.1) and (2.2) leads to

$$e = \frac{1}{N} \cdot \mathrm{MFD} \cdot \theta \tag{2.3}$$

and

$$r = \frac{1}{N} \cdot g \cdot \theta \tag{2.4}$$

in the time domain, where the small letters denote the inverse Fourier transforms of the corresponding capital letters and N is a scaling factor depending on definition of Fourier transformation. Combination of Eq. (2.3) and (2.4) leads to

$$\mathrm{mfd} = N \cdot \frac{e}{\theta} = g \cdot \frac{e}{r} \quad . \tag{2.5}$$

No problem will occur, if the magnitude of r approaches zero. Since, both e and r, can be written as a sum of functions which decays exponentially with a linear argument in time, the Gaussian function g with an exponential decay quadratic in time dominates the behaviour of mfd for large times for which the function mfd converges to zero. Fourier transformation of mfd yields the desired magnetic field distribution MFD. Fig. 1 shows the whole procedure schematically.

2.3 Methods

Spectroscopic *in vitro* and *in vivo* experiments were carried out in order to test the proposed method for the assessment of the MFD. All measurements were performed on a 1.5 Tesla whole body system (Magnetom Vision, Siemens Healthcare, Erlangen, Germany). For volume selection, a single voxel STEAM sequence (TR = 2000 ms, TE = 10 ms, TM = 15 ms) was applied. Data processing was executed on a personal computer using the Matlab Signal Processing Toolbox (The MathWorks, Inc., Natick, MA, USA). The recorded time domain signals from the investigated spectrum E and the reference spectrum R of both, *in vitro* and *in vivo* examinations, were filtered by a Gaussian function with a half width of 150 ms and underwent a fast Fourier transformation followed by baseline correction and constant and linear phase correction.

2.3.1 *In Vitro* Examinations

A glass sphere with a diameter of 100 mm was filled with vegetable oil providing a rather homogeneous magnetic field for recording a reference spectrum. For simulation of several different lipid compartments with more inhomogeneous field distribution, two glass tubes with a diameter of 8 mm were filled with vegetable oil and closed at both ends with silicone. The tubes were hanged with nylon threads in a Plexiglas frame and surrounded by air. One of the tubes with a length of 20 cm was always positioned parallel to the static magnetic field B_0 and the other one with a length of 15 cm was positioned under different angles (α = 45°, 60°, 75° and 90°) to B_0 and different vertical distances (d = 0 mm, 5 mm and 10 mm) to the first tube at the crossing (see Fig. 3b). The spectra were measured using the standard head coil of the manufacturer for radio frequency (RF) irradiation and signal acquisition. Voxel size was chosen to 20 x 20 x 40 mm^3. Voxel position was at the centre of the glass sphere, or at the crossing of the two tubes, respectively. For the signals from the oil-filled sphere serving as reference for lipids, T2 of the dominating methylene groups ($(–CH_2)_n$) at 1.5 Tesla was determined by the aid of a multi-spin-echo sequence and amounted to T2 = 68 ms. The corresponding linewidth $\Delta\omega$ = 7.5 Hz of the methylene groups in the spectrum of R leads to a time constant T_g = 166 ms for g. Calculation of the MFD yields the field distributions MFD_1 and MFD_2 of both tubes, which could be easily separated. Convolution of MFD_1 or MFD_2 and the reference spectrum R gave the contribution of each tube to the measured spectrum.

2.3.2 *In Vivo* Examinations

A frequency selective prepulse was used for suppression of the water signal. Additionally, a reference spectrum was recorded from tibial bone marrow (BM). Voxel size was always chosen to 11 x 11 x 20 mm^3, with the 20 mm extent along the leg

axis. All derivations in the Theory part were based on the assumption that only signals from one interesting substance occur in the spectra. This precondition is not fulfilled for the entire spectra recorded *in vivo*. Muscular spectra also show signals from water, creatine and choline and marrow spectra can show additional water signals. For this reason, it is necessary to restrict the calculations on lipids to the chemical shift range between 0.5 and 2.5 ppm containing the main signals of fatty acid triglycerides and no further signal components. Irrelevant parts of the spectra were cut-off after baseline and phase correction. The cut-off was done smoothly by fitting the flanks at 0.5 and 2.5 ppm with an exponential function as shown in Fig. 2 by examples from bone marrow and musculature. Since the molecular composition of the lipids (fatty acids and triglycerides in the chemical shift range of 0.5 - 2.5 ppm) in IMCL, EMCL and BM are nearly identical and BM is located in a

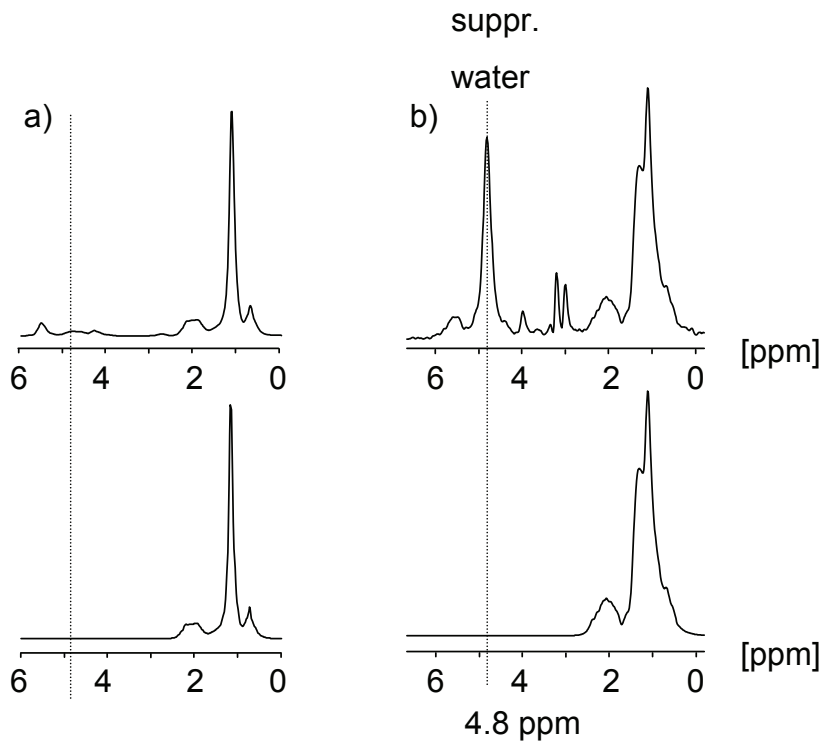

Figure 2: *Spectra acquired from tibial bone marrow (a) and m. soleus (b), upper row: original spectra, lower row: cut-off spectra.*

Table 1: *Mean values and standard deviations of the reproducibility measurements of the IMCL content of three subjects (A, B, C) for the muscle tibialis anterior (TA) and muscle soleus (SOL) evaluated with Method 1 and Method 2, respectively, as described under Methods.*

	TA		SOL	
	Method 1	Method 2	Method 1	Method 2
A	1.57 ± 0.25	1.60 ± 0.26	6.25 ± 1.19	3.32 ± 0.18
B	1.94 ± 0.52	1.77 ± 0.53	4.95 ± 1.48	2.13 ± 0.04
C	2.13 ± 0.04	1.95 ± 0.14	6.80 ± 1.48	4.32 ± 0.38

Note: *The IMCL content was normalized to the creatine content determined by a fit with a Lorentzian lineshape.*

rather homogeneous field, the procedure described in the Theory part can be used to calculate the MFD of lipids in TA and SOL. For the signals from BM serving as reference for lipids, T2 of the dominating methylene groups ($(-CH_2)_n$) at 1.5 Tesla is known and amounts to T2 = 80 ms [18]. The corresponding linewidth $\Delta\omega = 8$ Hz of the methylene groups in the spectrum of BM leads to $T_g = 70$ ms.

This allows to calculate the total MFD of lipids in musculature by the proposed procedure. To separate IMCL and EMCL in the MFD, prior knowledge is necessary because of the overlapping of the two peaks. Two methods were used to split up both parts:

Method 1:
The IMCL and EMCL part were separated by fitting the MFD with two Gaussian lineshapes without further restrictions about amplitude and linewidth.

Method 2:
In spectra out of SOL and TA with a dominating IMCL signal, a linear correlation was found between the linewidth of the methylene peak of IMCL ($\Delta\omega_{\mathrm{IMCL}}$) and Creatine ($\Delta\omega_{\mathrm{Cr}}$) which amounts to $\Delta\omega_{\mathrm{Cr}}/\Delta\omega_{\mathrm{IMCL}} = 0.91 \pm 0.03$. Therefore, demanding

Table 2: *The full widths at half-maximum $\Delta\omega_1$ and $\Delta\omega_2$ (ppm) in both tubes and the mean frequency difference $\Delta\nu$ (ppm) assessed for different orientations (α) and distances (d) in the arrangement*

	d = 0 mm			d = 5 mm			d = 10 mm		
α	$\Delta\omega_1$	$\Delta\omega_2$	$\Delta\nu$	$\Delta\omega_1$	$\Delta\omega_2$	$\Delta\nu$	$\Delta\omega_1$	$\Delta\omega_2$	$\Delta\nu$
45°	0.06	0.47	1.80	0.07	0.26	1.99	0.07	0.09	2.12
60°	0.07	0.76	2.88	0.07	0.37	3.03	0.07	0.12	2.99
75°	0.07	0.84	3.29	0.06	0.27	3.59	0.06	0.17	3.65
90°	0.06	0.84	3.79	0.07	0.32	3.82	0.07	0.13	3.88

a smooth but not necessarily symmetrical decay at the right side of the EMCL part and the linewidths of the IMCL part kept fixed with respect to creatine, the IMCL part is fitted by a Gaussian lineshape, varying one free fit parameter for the amplitude until the difference between the MFD and the Gaussian lineshape gets an as smooth as possible decay. Although a disadvantage of this method may be the subjective and visual view of the smoothness, this fit procedure is rather stable due to the fact that the amplitude is the only free fit parameter resulting in clearly smaller deviations as demonstrated in Table 1. Both methods worked well for TA. For SOL, however, the first fitting procedure lead to clearly larger linewidths in the IMCL part compared to the IMCL part in TA. In some cases, the residual of fitting even contained a distinct additional signal towards higher frequencies on the right side of the IMCL peak in the MFD. Assuming a narrow Gaussian distribution for the IMCL, this additional signal must belong to the EMCL part, since there are only lipid signals present in this frequency range (1.5 - 0.5 ppm). In this case, the IMCL part is located within the right slope of the EMCL part. For the determination of intra- and inter-individual reproducibility, spectra out of the muscle tibialis anterior (TA) and the muscle soleus (SOL) of three subjects were measured three consecutive times with a break of about 15 minutes between the first and second measurement and a break of one week between the second and third measurement. The voxel was set

at identical positions in the muscles for all three measurements. All subjects gave their informed consent before the investigation.

2.4 Results

2.4.1 *In Vitro* Examinations

The spectra from the spherical oil sample were well resolved (Fig. 3a). The experiments with crossing tubes showed a marked variability of the spectral pattern depending on the orientation of the tubes and on the distance between the tubes at the crossing. Decreasing distance of the tubes at the crossing points led to a more

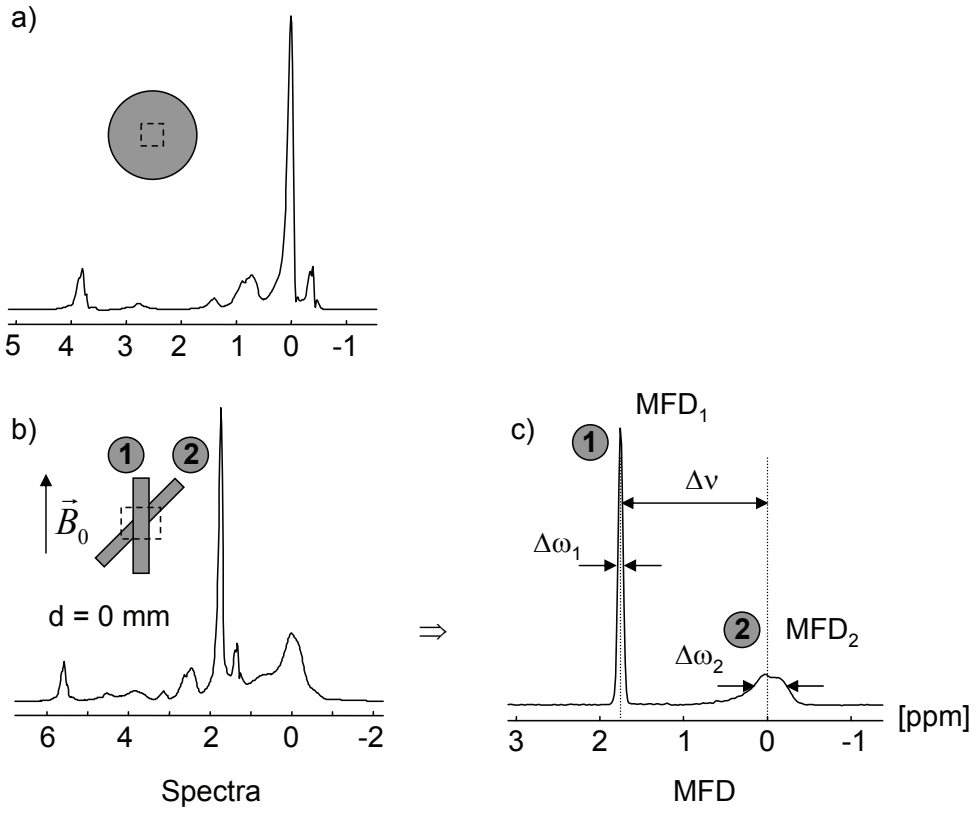

Figure 3: *Spectra acquired from the sphere (a), the tubes for the case α = 45° and d = 0 mm (b) and the corresponding MFD (c).*

inhomogeneous field distribution, especially in the tube oblique to B_0. The mean Larmor frequency difference of both tubes was increasing with the orientation angle of the second tube with a maximum at 90°. Fig. 3b shows an example of spectra from a voxel covering both tubes at the crossing point. The proposed deconvolution procedure for a spectrum from the crossing tubes (E) was applied using the spectrum from the sphere as reference. Fig. 3c shows the resulting total MFD of E. The field distributions MFD_1 and MFD_2 of both tubes are well separated. The full widths at half maximum $\Delta\omega_1$ and $\Delta\omega_2$ in both tubes and the mean frequency

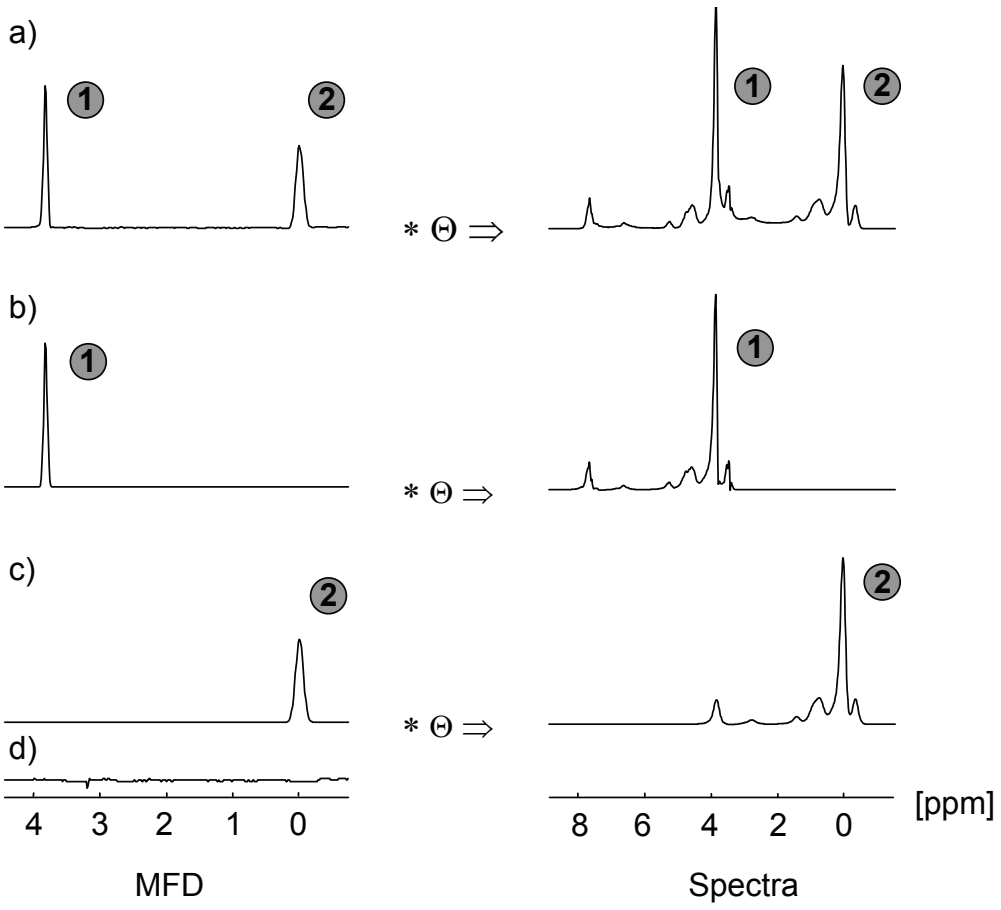

Figure 4: *Convolution of the total MFD (a), MFD_1 (b) and MFD_2 (c) with reference spectrum R for the case $\alpha = 90°$ and $d = 10$ mm. The residual of fitting the MFD is shown in (d).*

difference $\Delta\nu$ assessed for different orientations (α) and distances (d) in the tube arrangement are listed in Table 2. Calculating the convolution of only one part of the total MFD (MFD_1 or MFD_2) and the reference spectrum R, the contribution of each tube to the measured spectrum can be simulated as shown in Fig. 4.

2.4.2 *In Vivo* Examinations

The MFD for lipids in skeletal musculature was assessed by spectra from the muscle tibialis anterior (TA) and the muscle soleus (SOL), using the lipid spectrum from tibial bone marrow (BM) as reference R. Fig. 5 shows a recorded spectrum R serving for referencing, muscular spectra E and calculated MFD. The assignment of the partial MFDs of IMCL (MFD_{IMCL}) and EMCL (MFD_{EMCL}) was based on the prior knowledge about a narrow and symmetrical shape of MFD_{IMCL} due to its spherical geometry. The remainder of the MFD is expected to represent MFD_{EMCL}. Especially MFD_{EMCL} in SOL shows an asymmetrical distribution in Fig. 5d which was similar in other examples. Furthermore, most spectra from SOL confirmed MFD_{IMCL} to be symmetrical and narrow, and located inside the range of MFD_{EMCL}.

Convolution of only MFD_{IMCL} or MFD_{EMCL} and the function Θ leads to a selective presentation of the IMCL or EMCL contributions in the measured spectrum. This simulation of "partial spectra" is demonstrated in Fig. 6 for a measured spectrum from the muscle soleus for both, Method 1 and Method 2. In the muscle soleus the superposition of EMCL signals on IMCL signals was found to be clearly more pronounced than expected. The reason is the asymmetrical lineshape of MFD_{EMCL} with a broad slope towards lower magnetic field (Fig. 6b). This phenomenon is hidden in the recorded spectra. For this reason, most IMCL values from SOL derived by fixed integration borders or by fitting with symmetrical line shapes are overestimated which is demonstrated in Table 1 showing the results of the intra- and inter-individual studies. The IMCL in the muscle soleus could be measured with a

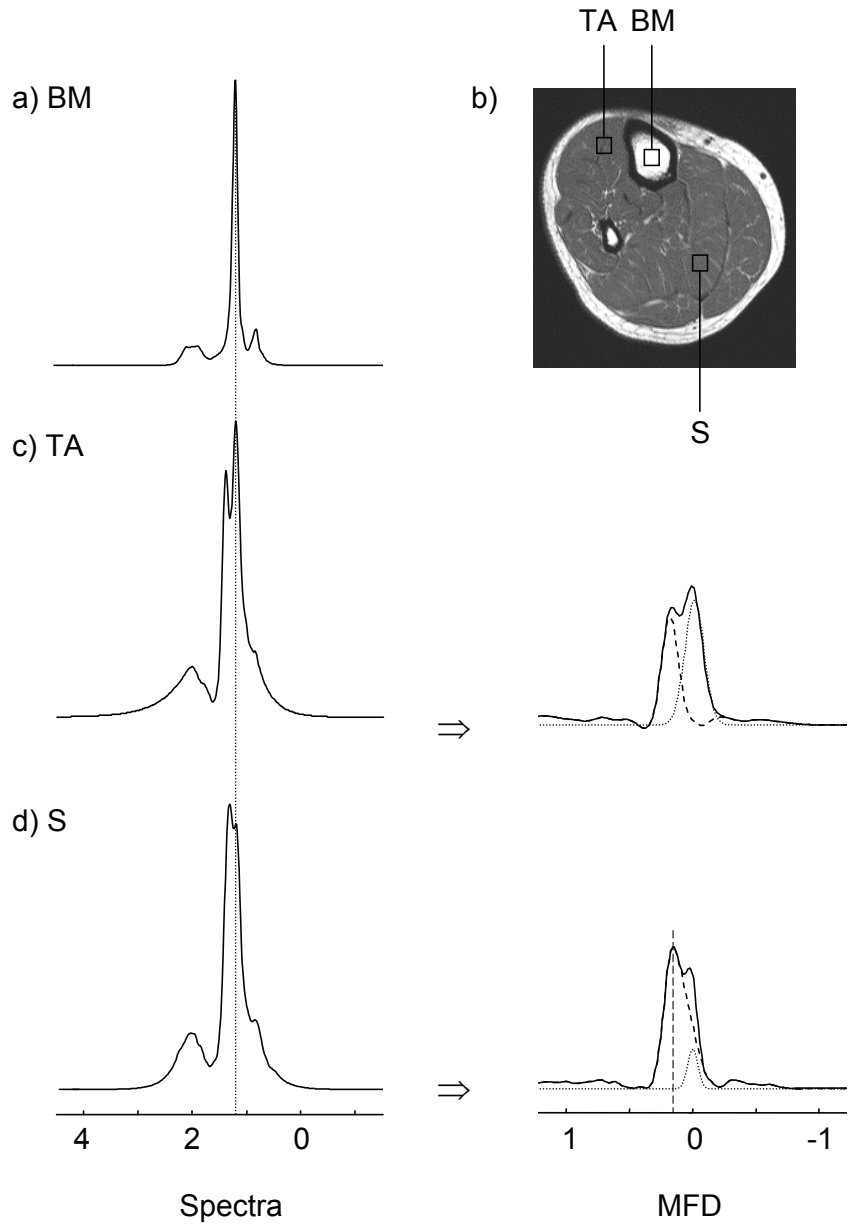

Figure 5: *Cut–off spectra acquired from tibial bone marrow (a), m. tibialis anterior (c) and m. soleus (d) of the voxels shown in (b). In the right column of (c) and (d) the corresponding total MFD (solid line), the MFD_{EMCL} (dashed line) and the MFD_{IMCL} (dotted line) are depicted. The vertical dashed line elucidates the asymmetrical lineshape of MFD_{EMCL}*

better reproducibility as shown by the distinctly smaller standard deviations and a clearly lower content in comparison to the method with Gaussian fitting. In contrast,

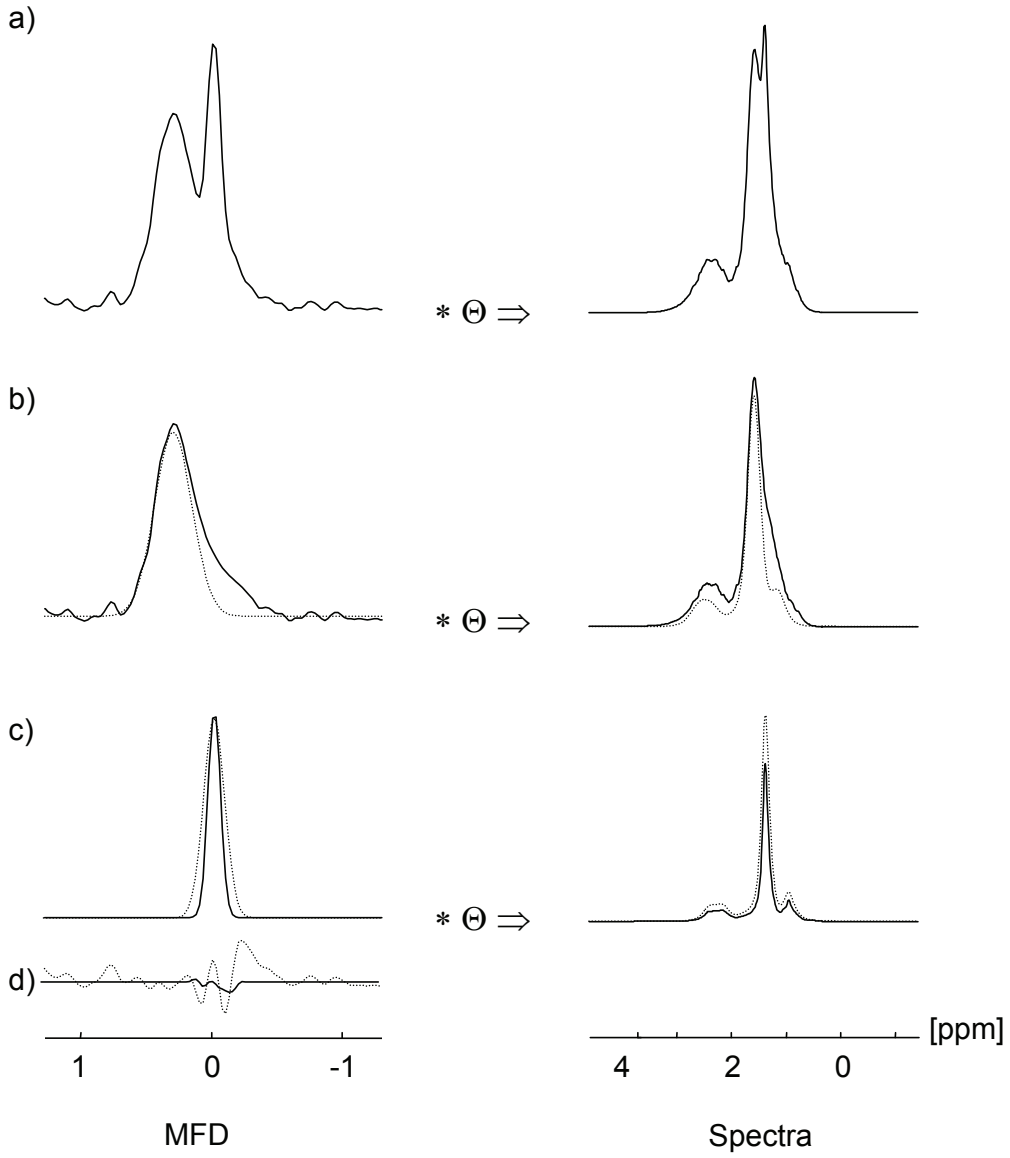

Figure 6: *In the left column the total MFD (a), the MFD_{EMCL} (b), the MFD_{IMCL} (c) and the residual of fitting the MFD (d) are depicted. In the right column, the corresponding convolutions with theoretical lipid spectrum Θ are shown. The dashed lines in (b), (c) and (d) show the fit with Method 1 (two Gaussians) and the solid lines the fit with Method 2.*

the IMCL content in the muscle tibialis anterior shows no significant difference for both methods.

2.5 Discussion

In a former work, the principle of deconvolution has been used for measuring the contribution of trabecular bone structure and density of the upper femur to the effective transverse relaxation time in trabecular yellow bone marrow [17]. Using a signal out of subcutaneous tissue as a reference and assuming a line broadening function with an exponential decay, line broadening could be estimated by division and fitting in time domain. The work presented here applies a similar procedure assuming a corresponding spectral composition of EMCL, IMCL and tibial bone marrow lipids. As in [17], the assumption of a similar chemical composition of the muscle lipids and the lipids in BM is crucial for the procedure. However, it is known that the chemical composition of muscle lipids and adipose tissue as subcutaneous fat or tibial bone marrow lipids is nearly the same [15–17]. No trabecular structures exist in the mid-tibia in contrast to the upper femur and only fatty acid triglycerides are measured in rather homogeneous surroundings. This indicates that all requirements in the Theory part are fulfilled. The presented work focused on the explicit lineshape of the MFD experienced by a substance in living tissue rather than $T2^*$ measurements, which would only provide a very unspecific and rough information about line broadening caused by both lipid compartments together. To the knowledge of the author, this is the first direct demonstration of the MFD of a substance in living tissue, allowing a pure visualization of susceptibility effects.

The aim for the development of the deconvolution procedure was to simplify the evaluation and interpretation of spectra recorded from human musculature. It is known from earlier studies that musculature shows at least two different lipid containing compartments with a clearly visible frequency shift in the spectra of about

0.2 ppm [2, 3]. The reason for the different magnetic field strength was shown to be the geometric arrangement of the IMCL and EMCL compartments and the various susceptibilities of the surrounding tissue components [3]. Original spectra recorded from musculature showed a line pattern depending on the MFD and on the chemical shift as well, and distinguishing of IMCL and EMCL components is not trivial. Even sophisticated, especially edited one-dimensional or two-dimensional, techniques of localized ^{1}H MR spectroscopy, which provide more details about the composition of musculature *in vivo* [19], do not allow to distinguish between portions of EMCL and IMCL, since the molecular composition in these tissue compartments is nearly identical.

For both the proposed method and standard fitting methods, acquisition and post processing of the data has to be performed carefully. Since water is the dominating signal in muscle tissue, water suppression is essential. The voxel has to be chosen carefully such that contaminating components of subcutaneous fat tissue or macroscopic fatty septa are excluded or minimized and mainly muscle tissue is included. A local shim is necessary to get optimized homogeneity within the voxel and high signal intensity to avoid problems with signal-to-noise ratio. Furthermore, thorough phase correction for both, the muscle spectrum and the bone marrow spectrum, has to be done to avoid a mixture of real and imaginary part. The signals from residual water, choline, creatine and other metabolites are excluded by a cut-off procedure as described in the Methods part.

Both portions, EMCL and IMCL, can be distinguished in the simpler shaped MFD. Two main peaks of both contributions are visible. It was confirmed that the field distribution of IMCL is nearly symmetrical and narrow for all muscle groups and voxel positions examined. In contrast, for EMCL a frequently asymmetrical distribution of the magnetic field is revealed by the MFD that is most of the EMCL experience a higher magnetic field as neighbouring IMCL, but there are some EMCL portions with the same or even a lower magnetic field strength, compared to the IMCL in the

examined voxel. The asymmetry of the field distribution of EMCL was pronounced in the SOL, but not so evident in the TA. However, asymmetrical lineshapes seem to be rather the rule than the exception as several models for heterogeneous tissue show [13, 14]. Highly resolved muscular spectra recorded *in vivo* at 4 Tesla confirmed the mentioned asymmetry of EMCL signals in SOL [20, 21]. In contrast to EMCL layers and muscle fibres in the TA orientated nearly parallel to the axis of the leg and the static magnetic field B_0, the oblique arrangements of the muscle fibre bundles and the EMCL compartments in SOL are expected to be the reason for the marked asymmetry in the feathered muscle soleus with many fibre intersections.

The results show that usual fitting procedures with defined line shapes are not suitable for an adequate and quantitative assessment of IMCL and EMCL portions with their partly irregular and asymmetrical field distributions and the proposed technique with deconvolution of the spectral line pattern by a reference spectrum worked well in musculature. However, it should be mentioned that several conditions have to be fulfilled for a correct application: all signals in the analysed frequency range in the spectrum of interest and in the reference spectrum must stem from material with same chemical components. This precondition seems to be fulfilled with very good approximation for the fatty acid triglycerides in IMCL, EMCL and fatty bone marrow. A potential problem could be additional signal contributions from proteins or lactate in musculature. However, there is no evidence in the literature that considerable signal components from metabolites other than lipids occur in human muscle spectra in the chemical shift range between 0.5 and 2.5 ppm.

One may ask whether such effort is worthwhile in order to assess the content of lipids in myocytes more precisely. But as described in the introduction a number of metabolic studies have shown IMCL being involved in the pathogenesis of type 2 diabetes [5–7]. The turnover of IMCL during one bout of long lasting and submaximal exercise [8, 9] or lipid infusion under high insulin levels [22] was shown to be often more than 50%. These dramatic signal changes could be assessed un-

doubtedly, indicating the relevance of muscular lipids in endocrinology and sports medicine. The next step for future studies is the assessment of lipid metabolism under more physiological conditions. For testing smaller effects of nutrition, training, or short-term workload, clearly smaller changes in the IMCL content must be measurable with minimal errors. Usual techniques are quite critical and a precision better than 10% in the IMCL content is often hard to obtain, if the voxel position (and the EMCL contribution in the spectrum) has slightly changed. For this reason, an increased precision in the quantitative analysis of IMCL leads to a better applicability of MR muscle spectroscopy in a clinical environment.

References

[1] Bruhn, H., J. Frahm, M.L. Gyngell, K.D. Merboldt, W. Hänicke and R. Sauter: *Localized proton NMR spectroscopy using stimulated echoes: applications to human skeletal muscle* In vivo. Magn. Reson. Med., 17:82–94, 1991.

[2] Schick, F., B. Eismann, W.I. Jung, H. Bongers, M. Bunse and O. Lutz: *Comparison of localized proton NMR signals of skeletal muscle and fat tissue* in vivo*: two lipid compartments in muscle tissue*. Magn. Reson. Med., 29:158–167, 1993.

[3] Boesch, C., J. Slotboom, H. Hoppeler and R. Kreis: In vivo *determination of intramyocellular lipids in human muscle by means of localized* ^{1}*H-MR-spectroscopy*. Magn. Reson. Med., 37:484–493, 1999.

[4] Szczepaniak, L., E.E. Babcock, F. Schick, R.L. Dobbins, A. Garg, D.K. Burns, J.D. McGarry and D.T. Stein: *Measurement of intracellular triglycerides stores by H-1 spectroscopy: validation* in vivo. Am. J. Physiol., 276:E977–E989, 1999.

[5] Krššák, M., K. Falk Petersen, A. Dresner, L. DiPietro, S.M. Vogel, D.L. Rothman, G.I. Shulman and M. Roden: *Intramyocellular lipid concentrations are correlated with insulin sensitivity in humans: a 1H NMR spectroscopy study*. Diabetologia, 42:113–116, 1999.

[6] Jacob, S., J. Machann, K. Rett, K. Brechtel, A. Volk, W. Renn, E. Maerker, S. Matthaei, F. Schick, C.D. Claussen and H.-U. Häring: *Association of increased intramyocellular lipid content with insulin resistance in lean nondiabetic offspring of type 2 diabetic subjects*. Diabetes, 48:1113–1119, 1999.

[7] Perseghin, G., P. Scifo, F. de Cobelli, E. Pagliato, A. Battezzati, C. Arcelloni, A. Vanzulli, G. Testolin, G. Pozza, A. del Maschio and L. Luzi: *Intramyocellular triglyceride content is a determinant of* in vivo *insulin resistance in humans - a* ^{1}H–^{13}C *nuclear magnetic resonance spectroscopy assessment in offspring of type 2 diabetic parents*. Diabetes, 48:1600–1606, 1999.

[8] Brechtel, K., A. Niess, J. Machann, S. Jacob, H.-U. Häring, H.H. Dickhuth, C.D. Claussen and F. Schick: *Direct assessment of intramyocellular lipids (IMCL) during exercise in well trained male runners. a* ^{1}H*-MRS study*. Horm. Metab. Res., 33:63–66, 2001.

[9] Krššák, M., K.F. Petrsen, R. Bergeron, T. Price, D. Laurent, D.L. Rothman, M. Roden and G.I. Shulman: *Intramuscular glycogen and intramyocellular lipid utilization during prolonged exercise and recovery in man: a* ^{13}C *and* ^{1}H *nuclear magnetic resonance spectroscopy study*. J. Clin. Endocrinol. Metab., 85(2):748–754, 2000.

[10] Brechtel, K., J. Machann, S. Jacob, A. Strempfer, F. Schick, H.U. Häring and C.D. Claussen: In-vivo ^{1}H*-MR spectroscopy. The determination of the intra- and extramyocellular lipid content depending on the insulin effect in the direct offspring of type-2 diabetics*. Rofo. Fortschr. Geb. Rontgenstr. Neuen. Bildgeb. Verfahr., 171(2):113–120, 1999.

[11] KREIS, R. and C. BOESCH: *Liquid crystal-like structure of human muscle demonstrated by* in vivo *observation of direct dipolar coupling in localized proton magnetic resonance spectroscopy*. J. Magn. Reson. Series B, 104:189–192, 1994.

[12] SZCZEPANIAK, L.S. and D.T. STEIN: *Bulk magnetic susceptibility effects on the assessment of intra- and extracellular lipids* in vivo. Proc. Intl. Soc. Mag. Reson. Med., 7:1571, 1999.

[13] FORD, J.C., F.W. WEHRLI and H.W. CHUNG: *Magnetic field distribution in models of trabecular bone*. Magn. Reson. Med., 30:373–379, 1993.

[14] CHRISTMAN, R.A., D.C. AILION, T.A. CASE, C.H. DURNEY, A.G. CUTILLO S. SHIOYA, K.C. GOODRICH and A.H. MORRIS: *Comparison of calculated and experimental NMR spectral broadening for lung tissue*. Magn. Reson. Med., 35:6–13, 1996.

[15] ONTKO, J. A.: *Lipid metabolism in muscle*. In ENGEL, A.G. and C. FRANZINI-ARMSTRONG (editors): *Myology*, pages 665–682. McGraw-Hill Inc, New York, 1994.

[16] TAVASSOLI, M., D.N. HOUCHIN and P. JACOBS: *Fatty acid composition of adipose cells in red and yellow marrow: a possible determinant of haematopoietic potential*. Scand. J. Haematol., 18(1):47–53, 1977.

[17] WEHRLI, F.W., J. MA, J.A. HOPKINS and H.K. SONG: *Measurement of* R_2' *in the presence of multiple spectral components using reference spectrum deconvolution*. J. Magn. Reson., 131:61–68, 1998.

[18] MACHANN, J., F. SCHICK, S. JACOB, O. LUTZ and C.D. CLAUSSEN: *An interleaved sampling strategy for MR spectroscopy* in vivo*: applications on human calf musculature*. Magn. Reson. Imaging, 18:189–197, 2000.

[19] Kreis, R. and C. Boesch: *Spatially localized, one- and two-dimensional NMR spectroscopy and* in vivo *application to human muscle*. J. Magn. Reson. Series B, 113:103–118, 1996.

[20] Hwang, J.H., J.W. Pan, H.P. Hetherington and D.T. Stein: *Regional differences in intramyocellular lipids detected by ^1H spectroscopic imaging at 4T: enhanced spectral/spatial resolution*. Proc. Intl. Soc. Mag. Reson. Med., 8:30, 2000.

[21] Krššák, M., M. Krebs, H. Stingl, V. Mlynárik, S. Gruber, E. Moser and M. Rod: *Intramyocellular lipid (IMCL) stores before and after lipid infusion*. Proc. Intl. Soc. Mag. Reson. Med., 8:1883, 2000.

[22] Dahl, D.B., O.P. Bachmann, K. Brechtel, J. Machann, T. Meier, M. Nielsen, F. Schick, W. Renn, C.D. Claussen, H.-U. Häring and S. Jacob: *Effects of acute elevation of FFA and/or hyperinsulinemia on intramyocellular lipid content (IMCL)*. Diabetes, 49:1233, 2000.

3 Echo Planar Diffusion Tensor Imaging of the Lower Leg Muscles*

A sequence for echo planar diffusion tensor imaging of skeletal musculature was developed using a stimulated echo preparation. The strategy was optimized in order to obtain reliable diffusion tensor data in a short measuring time. Image distortion problems due to eddy currents arising from long lasting diffusion sensitizing gradients could be overcome by insertion of additional gradient pulses in the mixing time (TM) interval of the stimulated echo preparation. In contrast to former approaches with similar intention, the proposed strategy does not influence the stimulated echo signal itself and does not lead to prolonged echo time as in the case of spin echo methods. Phantom measurements were performed to compare eddy current induced distortion effects in diffusion weighted images. The diffusion tensor in the musculature of the lower leg was investigated in four healthy subjects and maps of the trace and the three eigenvalues of the diffusion tensor, fractional anisotropy maps, and angle maps were calculated from examinations before and after tiptoe exercises.

3.1 Introduction

MR diffusion tensor imaging (DTI) has been widely used over the past decade in order to measure molecular water diffusion *in vivo* [1–13] and has been proven to be a powerful non-invasive tool for providing additional information about microstructure and pathology of tissues.

In human tissues, diffusion is partly restricted by barriers such as cell membranes or large protein molecules. Diffusion in white matter of the brain or skeletal muscu-

*This Chapter was adapted from: Steidle G, Schick F. Echoplanar diffusion tensor imaging of the lower leg musculature using eddy current nulled stimulated echo preparation. Magn Reson Med 2006;55:541-548.

lature is, therefore, not rotationally invariant but more enhanced in the direction of the longitudinal axis of the fibres compared to perpendicular directions. Although several tissue compartments with exchanging water molecules are involved, the diffusion behaviour of tissue is often described by a symmetric second rank tensor in a simplified model [2]. Diffusion tensor imaging (DTI) techniques assess the diffusion sensitive signal attenuations caused by diffusion sensitizing gradients along several independent directions. Since a symmetric second rank tensor is characterized by six independent components, at least six independent directions for the diffusion gradients have to be assessed in order to calculate the entire tensor.

If conventional techniques are used for diffusion weighted imaging, the final images will often show marked artefacts due to irregular motion induced phase shifts. Those problems can be solved by additional scans for phase correction [14]. In addition, diffusion tensor imaging with at least four or six diffusion directions tends to become time consuming. Single-shot echo planar imaging (EPI) is rather robust even under conditions involving slight motion of the tissue under investigation and is, therefore, mainly used for DTI examinations.

A few studies have been reported on DTI applications outside the brain. Those reports mainly focused on studies in kidney [6–8], skeletal musculature [9–12] and tongue [13]. Musculature has a much shorter T2/T1 ratio than brain, especially for higher magnetic fields (water in musculature at 1.5 Tesla: T1 $\approx$ 1100 ms [15], T2 $\approx$ 30 ms [16, 17]). For this reason, signal-to-noise ratio (SNR) in diffusion weighted images of musculature is rather poor for higher b-values, if common sequences with spin-echo (SE) preparation are applied leading, furthermore, to long echo times (often > 100 ms) for high b-values. This problem can be solved by replacing the common SE preparation by a stimulated echo (STE) preparation. The stimulated echo preparation allows increasing b-values by augmenting TM rather than TE, and relaxation dependent signal losses are clearly lower in the TM interval (only T1-sensitive) than during TE (T2-sensitive).

Long lasting diffusion gradient pulses with high intensity can induce distinct eddy currents (EC) even in systems with actively shielded gradient coils. Unfortunately, due to the low bandwidth of EPI sequences in phase-encoding direction, these ECs might cause significant spatial distortions in the images, dependent on the direction of the applied diffusion gradients. In DTI, misregistration artefacts occur in the calculated diffusion maps from multiple images with different diffusion gradient directions. In recent years, several methods have been implemented to reduce distortions caused by ECs [13,18–27]. In most work [18–25], post processing methods were used to account for the artefacts. In other studies, bipolar gradients were implemented within the sequence scheme to minimize eddy currents caused by the diffusion gradients [13, 26, 27]. While Alexander et al. [26] and Reese et al. [27] used this method in combination with SE preparation for DTI in brain, Gilbert et al. [13] measured DTI in human tongue and minimized eddy currents by using stimulated echoes and splitting the two long unipolar gradients into two shorter bipolar gradients separated by a 180° refocusing pulse. Bipolar gradient waveforms avoid marked EC effects, and additional post processing steps are often not necessary. However, in case of SE preparation, the minimal TE is further increased leading to unacceptable signal loss especially for tissues with short T2. A further approach to minimize image distortions in DTI may be the use of single-shot turbo spin echo (TSE) techniques instead of EPI which are much less sensitive to the effects of ECs [11,21]. However, the higher SAR, the lower SNR and the longer readout train make EPI preferable to TSE in most situations.

The methodical approach reported in the following includes an adapted STE preparation that drastically reduces eddy current-induced image distortions by insertion of additional gradients, but without an associated increase of echo time TE and without the need of additional refocusing pulses as in the work of Gilbert et al. [13].

Besides methodical developments, a further aim of the performed studies was a more precise determination of diffusion characteristics in skeletal musculature and,

especially, a sensitive assessment of exercise induced effects on muscular diffusion. It has been reported in the literature [16, 17, 28, 29] that T2 values in skeletal musculature are markedly prolonged after exhaustive exercises, but the reason and the involved compartment(s) containing the modified water (extracellular or intracellular) are not yet understood. For this purpose, changes in the diffusion tensor in working muscles were assessed parallel to T2-weighted imaging.

3.2 Material and Methods

3.2.1 Eddy Current Correction

Due to summing up of phase distortions during the readout in EPI sequences, such techniques are very sensitive to timely variable ECs as present after long lasting diffusion sensitizing gradients. On the other hand, EPI is very common for DTI because of its short measuring time, high signal-to-noise ratio, and insensitivity to patient motion. To compensate for the EC effects, a technique that was originally proposed for SE diffusion preparation [27] was adapted for the STE diffusion preparation. Additional gradient pulses were implemented within the mixing time TM in the STE preparation. In doing so – together with the diffusion gradients – two sets of bipolar gradient pulses are created around the second and third 90° RF pulse for minimizing the influence of ECs (Fig. 1). In contrast to the compensation of ECs in SE diffusion preparation [27], the proposed EC compensation in STE preparation does not result in any undesired prolongation of the sequence timing. Assuming a mono-exponential temporal decay of ECs with a time constant κ, the eddy currents for the two bipolar gradient pulses can be described by

$$J_1(\kappa) = J_0 \cdot \exp(-t/\kappa) \cdot \left[+1 - \exp(t_0/\kappa) - \exp((t_0 + s)/\kappa) + \exp((t_0 + s + t_1)/\kappa)\right] \quad (3.1)$$

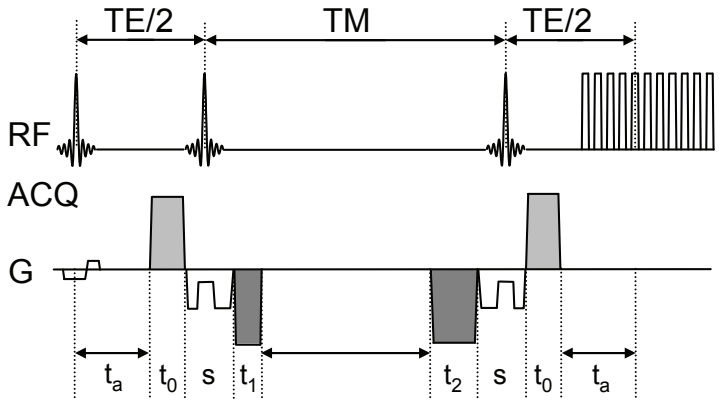

Figure 1: *EPI sequence with stimulated echo diffusion preparation. Additional gradient pulses (dark-grey shaded) in the mixing time TM were inserted for minimizing eddy current effects. Furthermore, asymmetrical TM and TE crusher gradients were arranged around the second and third slice selection gradients in order to avoid unwanted echoes, if small b-values are chosen.*

$$J_2(\kappa) = J_0 \cdot \exp(-t/\kappa) \cdot \left[-1 + \exp(t_2/\kappa) + \exp((t_2+s)/\kappa) - \exp((t_2+s+t_0)/\kappa)\right] \quad (3.2)$$

where J_0 is the initial eddy current amplitude for each transition. The time periods t_0, t_1, t_2, and s are indicated in Fig. 1. According to equations [3.1] and [3.2] eddy current effects proportional to $\exp(-t/\kappa)$ vanish, if

$$t_1(\kappa) = \kappa \cdot \ln\left[1 + \exp(-s/\kappa) - \exp(-(t_0+s)/\kappa)\right] \quad \text{and} \quad (3.3)$$

$$t_2(\kappa) = \kappa \cdot \ln\left[1/(1 + \exp(s/\kappa) - \exp((t_0+s)/\kappa)\right] \ . \quad (3.4)$$

If κ is much larger than t_0, κ can be approximated by infinity and the equations simplify to $t_1 = t_0$ and $t_2 = t_0$, respectively. However, ECs with other time constants κ would also be significantly reduced: The percentage residual eddy current for the time constants $\kappa = 100, 50, 30$ and 20 ms amounts to 1%, 2%, 7%, and 17%, respectively. Altogether, the proposed eddy currents compensation is not very sensitive on exact adjustments of the additional gradient pulses with duration t_1 and t_2

on the actual κ, and a marked reduction of EC effects can be expected even for only roughly adjusted compensation gradient pulses.

3.2.2 Optimization of Diffusion Preparation

Timing and Relaxation parameters

For an SE preparation, the b-value given by $b = \gamma^2 G^2(\delta^2(\Delta - \frac{1}{3}\delta) - \frac{1}{6}\epsilon^2\delta + \frac{1}{30}\epsilon^3)$ [30] depends only on TE (for a fixed ramp time ϵ of the diffusion gradients and a maximal possible diffusion gradient amplitude G) where δ is the duration of the diffusion gradient pair separated by a delay Δ and $\gamma = 267.522 \times 10^6$ rad·s^{-1}·T^{-1} is the gyromagnetic ratio for protons. For an STE preparation, the same b-value can be achieved for many suitable pairs of TE and TM with $TE = s + 2(\delta + \epsilon) + 2t_a$, $TM = \Delta - s - \epsilon - \delta$ and $t_0 = \delta + \epsilon$, where increasing TE will result in a decreasing TM and vice versa. The b-value can also be expressed in terms of TE and TM leading to

$$b = \gamma^2 G^2 \cdot [(TE/2 - \tau)^2 \cdot (TM + s + \epsilon) + \frac{2}{3}(TE/2 - \tau)^3 - \frac{1}{6}\epsilon^2(TE/2 - \tau) + \frac{1}{30}\epsilon^3] \,, \tag{3.5}$$

where τ is given by $\tau = t_a + \epsilon + s/2$. The signal intensity is $S = S_0 \cdot \exp(-TE/T2) \cdot \exp(-TM/T1) \cdot \exp(-bD)$, with S_0 being the signal intensity without diffusion and without T1 and T2 weighting. A maximum for S exists for a certain pair of TE and TM under the condition of a given fixed b-value and given relaxation properties T1 and T2. Solving this constraint extremal problem by the method of Lagrange multipliers, the pair of TE and TM that maximizes S has to fulfil the two conditions $T1/T2 = (\partial b/\partial TE)/(\partial b/\partial TM)$ and $b = b(TE, TM)$ for an arbitrary b-value function depending on TE and TM. In our case this leads to the condition

$$T1/T2 = \Delta/\delta - \frac{1}{12}(\epsilon/\delta)^2 \approx \Delta/\delta \,, \tag{3.6}$$

where the additional quadratic term in (ϵ/δ) can be neglected in comparison to Δ/δ.

Suitable b-values

In order to calculate the diffusion tensor $\hat{D}$, diffusion-sensitizing gradients were applied along six different directions indicated by the vectors $\vec{e}_1 = (1,0,1)$, $\vec{e}_2 = (-1,0,1)$, $\vec{e}_3 = (0,1,1)$, $\vec{e}_4 = (0,1,-1)$, $\vec{e}_5 = (1,1,0)$, and $\vec{e}_6 = (-1,1,0)$ leading to signal intensity equations $S_i = S_0 \cdot \exp(-bD_i)$ where $D_i = \vec{e}_i \cdot \hat{D}\vec{e}_i$. (The dot $\cdot$ denotes the scalar product of the vectors $\vec{e}_i$ and $\hat{D}\vec{e}_i$.) The diffusion coefficients $D_i = 1/b \cdot \ln(S_0/S_i)$ are used to calculate the matrix elements of the diffusion tensor:

$$
\begin{aligned}
D_{xx} &= 1/2 \cdot (+D_1 + D_2 - D_3 - D_4 + D_5 + D_6) \\
D_{yy} &= 1/2 \cdot (-D_1 - D_2 + D_3 + D_4 + D_5 + D_6) \\
D_{zz} &= 1/2 \cdot (+D_1 + D_2 + D_3 + D_4 - D_5 - D_6) \\
D_{xy} &= 1/2 \cdot (D_5 - D_6) \\
D_{xz} &= 1/2 \cdot (D_1 - D_2) \\
D_{yz} &= 1/2 \cdot (D_3 - D_4)\ .
\end{aligned}
\tag{3.7}
$$

The SNR of a diffusion coefficient D_i, (SNR_{D_i}) is given by

$$
\mathrm{SNR}_{D_i} = \mathrm{SNR}_0 \frac{bD_i}{\sqrt{1 + \exp(2bD)}}, \tag{3.8}
$$

where SNR_0 is the SNR for $b = 0$ (dependent on TE and TM). The b-value, which maximizes SNR_{D_i}, was determined by a numerical simulation and amounts to $b = 1.108/D$. The mean apparent diffusion coefficient (ADC) D_{av} defined as $D_{\mathrm{av}} = 1/3\mathrm{tr}(\hat{D})$ is equal to $1/6(D_1 + D_2 + D_3 + D_4 + D_5 + D_6)$. Therefore, the b-value should be chosen in the range of the inverse of D_{av} of the examined tissue to obtain optimal SNR in the diffusion tensor map. Using this relation for an ADC value of about $D_{\mathrm{av}} \approx 1.6 \times 10^{-3}$ mm^2/s [9], an optimal b-value of about 700 s/mm^2 is obtained.

SE versus STE Preparation

The echo signal for an SE preparation is given by $S_{\mathrm{SE}}(TE) = S_0 \cdot \exp(-TE/T2) \cdot$

$\exp(-bD)$ and for an STE preparation

$$S_{\mathrm{ST}}(TM) = 0.5 \cdot S_0 \cdot \exp(-TE_{\min}/T2) \cdot \exp(-TM/T1) \cdot \exp(-bD) \ .$$

Although an STE preparation provides only half of the basic signal of an SE preparation, the echo signal for an STE preparation exceeds the echo signal for an SE preparation for a certain b-value depending on the values of T1 and T2. In Fig. 2, the signal decays for both preparations are shown for the relaxation times of the human calf musculature T1 = 1100 ms [15] and T2 = 30 ms [16, 17]. For these parameters, the echo signal for an STE preparation will top the echo signal for an SE preparation for b-values higher than 300 s/mm^2.

Table 1: *TE values for a spin echo (SE) preparation (where the product sequence of Siemens with identical readout parameters was used) and TE and TM values for a stimulated echo (STE) preparation for different b-values, respectively. TE is always chosen minimal that is diffusion gradient amplitude G_{diff} reaches the maximal value of 35 mT/m. In case of STE preparation the ratio of TM/TE obeys the condition of Eq. 3.6 for T1 = 1100 ms and T2 = 30 ms. Corresponding signal values for the SE preparation and the STE preparation, respectively, are shown in Fig. 2.*

Spin Echo ([b] = 10^{-3} s/mm^2, [TE] = ms)												
b	=	36	105	206	301	421	529	610	700	849	903	1017
TE	=	41	48	54	58	62	65	67	69	72	73	75
Stimulated Echo ([b] = 10^{-3} s/mm^2, [TE, TM] = ms)												
b	=	53	91	142	210	299	407	541	699	885	1101	
TE	=	28	29	30	31	32	33	34	35	36	37	
TM	=	90	109	127	145	164	182	201	219	237	255	

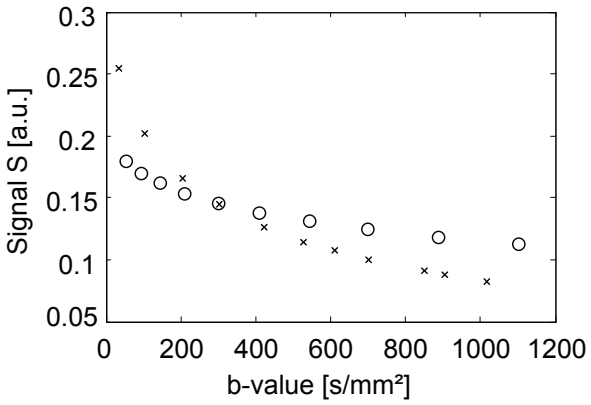

Figure 2: *Relaxation dependent signal loss for an SE (crosses) and an STE (circles) preparation as a function of the b-value. The basis for the simulation was T1 = 1100 ms and T2 = 30 ms. The signal yield using the STE preparation is better for b-values higher than approx. 300 s/mm^2. Corresponding TE values for the SE preparation and TE and TM values for the STE preparation, respectively, are shown in Table 1. (Signal losses due to diffusion that is the factor* $\exp(-bD)$ *were omitted for a more distinct illustration of the signal differences.)*

3.2.3 Sequence Parameters

Measurements were performed on a 1.5 T whole-body MR unit (Magnetom Sonata, Siemens Healthcare, Erlangen, Germany). For signal detection, a transmit/receive extremity coil of the manufacturer was employed. Diffusion images were acquired with a diffusion weighted STE-EPI sequence with a fractional readout of 6/8 to minimize TE. The image matrix was 64 × 64 and the field of view was 200 mm × 200 mm leading to a nominal voxel size of 3.1 mm × 3.1 mm. Further imaging parameters were: receiver bandwidth 2004 Hz per pixel, slice thickness 7 mm, transverse slice orientation. Maximum gradient strength was 35 mT/m and the maximal slew rate was 180 mT/(m·ms). Parameters TE, TM and b-value were optimized as described above leading to the sequence parameters TE = 33 ms, TM = 182 ms and b = 700 s/mm^2. The corresponding time variables introduced in Fig. 1 for the

chosen TE and TM are t_0 = 5.26 ms, t_1 = 4.81 ms, t_2 = 5.79 ms, s = 4.0 ms and t_a = 9.24 ms where the same EC time constant κ of 100 ms as in [27] was chosen.

3.2.4 Measurements

Phantom Measurements

Distortion effects caused by eddy currents due to diffusion gradients were tested in STE-EPI sequences and for the purpose of comparison in SE-EPI sequences without and with EC correction using a water-filled bottle phantom of the manufacturer. The diffusion sensitizing in the SE sequence without EC correction was built by two diffusion gradients flanking the refocusing RF pulse. The SE sequence with implemented EC correction was a double spin-echo sequence with four diffusion gradients as introduced in [27] and implemented as a standard product sequence on the scanner.

The echo times for the SE-EPI sequences were TE = 62 ms for the SE sequence without EC correction and TE = 69 ms for the SE sequence with EC correction. For all four sequences a TR of 5000 ms and 8 averages were applied leading to a total measuring time of 4:45 min for recording a set of 7 images (one image without diffusion weighting and 6 diffusion weighted images for calculation of the tensor). The remaining sequence parameters were as described above. All measurements were repeated five times. The temperature within the magnet bore was 24 °C.

In Vivo *Measurements*

Four subjects were imaged with an STE-EPI sequence with EC correction as described above for measuring the diffusion tensor and derived diffusion parameters in a transversal slice of the lower leg. Additionally, a fat suppression pulse was applied before excitation. Five scans were averaged for each image. A TR of 2665 ms was applied leading to a total measuring time of 2 min.

(The reason for the choice of an total acquisition time of 2 min was the repeated application of the sequence in a protocol measuring the temporal course of diffusion before and after an exercise of the lower leg which is not part of this work.)

In order to investigate changes in diffusion characteristics, four subjects were examined before and after an intense exercise of the lower leg. The workload protocol consists of repeatedly standing on tiptoe on one leg with a frequency of 2 s. The exercise was executed until physical exhaustion leading to a mean duration of the exercise of approximately 1:30 min.

All subjects had given their informed consent prior to the examinations.

The reported diffusion weighted STE-EPI sequence and a T2-weighted multi-contrast turbo spin-echo sequence with seven echoes (measuring time 2 min.) were applied before the exercise. Immediately after the exercise, both sequences were alternately applied twenty times in order to derive the temporal course of the trace and the three eigenvalues of the diffusion tensor as well as the T2 values of the musculature of the calf. A control measurement was applied approximately two hours after the workload. The total pause between the conclusion of the measurements before the exercise and the beginning of the measurements after the exercise was approximately 6 min for all subjects.

3.2.5 Post-Processing

The diffusion weighted images were analysed offline on a PC workstation using home-made routines written with Matlab (The Mathworks, Inc., Natick, MA, USA). After signal averaging, noise correction was applied to the magnitude signal S_{orig} of each picture element with $S_{\mathrm{corr}} = \sqrt{\left|S_{\mathrm{orig}}^2 - \sigma^2\right|}$ where σ^2 is the variance of the noise [31]. For σ^2 an unbiased estimator with minimum variance can be derived by $\sigma^2 = \frac{1}{2}\left\langle R^2 \right\rangle$, where $\left\langle R^2 \right\rangle$ is the spatial average of the squared magnitude data out of a region in the image without MR proton signals [32]. This procedure is especially

Table 2: *Mean values of all four subjects for the apparent diffusion coefficient (ADC) and eigenvalues (λ_1, λ_2 and λ_3) of the diffusion tensor [$\times 10^{-3}$ mm^2/s], fractional anisotropy (FA) and pennation angles (PA) of the muscles gastrocnemius medialis (GM), gastrocnemius lateralis (GL), soleus (SOL) and tibialis anterior (TA).*

	GM	GL	SOL	TA
ADC	1.37 ± 0.09	1.30 ± 0.05	1.43 ± 0.05	1.39 ± 0.02
λ_1	1.87 ± 0.17	1.85 ± 0.11	1.89 ± 0.09	1.95 ± 0.05
λ_2	1.23 ± 0.08	1.21 ± 0.09	1.39 ± 0.14	1.25 ± 0.03
λ_3	1.01 ± 0.05	0.86 ± 0.09	1.03 ± 0.06	1.00 ± 0.01
FA	0.30 ± 0.05	0.34 ± 0.05	0.28 ± 0.03	0.37 ± 0.01
PA	22° ± 3°	12° ± 4°	37° ± 1°	11° ± 2°

Table 3: *Anisotropy values (standard deviation of the three eigenvalues of the diffusion tensor over the mean of the eigenvalues) of the muscles gastrocnemius medialis (GM), gastrocnemius lateralis (GL), soleus (SOL) and tibialis anterior (TA) for all four subjects (Sub). Anisotropy in GM and SOL was distinctly lower than in GL and TA.*

Sub	GM	GL	SOL	TA
#1	0.33 ± 0.03	0.41 ± 0.15	0.28 ± 0.04	0.37 ± 0.03
#2	0.25 ± 0.05	0.29 ± 0.04	0.26 ± 0.04	0.36 ± 0.05
#3	0.36 ± 0.03	0.35 ± 0.03	0.24 ± 0.03	0.39 ± 0.02
#4	0.29 ± 0.03	0.35 ± 0.03	0.34 ± 0.05	0.39 ± 0.03
mean	0.31 ± 0.05	0.35 ± 0.05	0.28 ± 0.04	0.38 ± 0.02

necessary for images with a relatively low signal because the formula for calculation of the b-value does not consider the background noise. To avoid artificial bright pixels in regions outside the lower leg, a binary filter was applied which considered only pixels containing tissue of the calf. The binary filter was defined by a polygon tracing the outer contours of the calf muscles. For the pixels outside the polygon,

the diffusion values were set to zero. The diffusion tensor was diagonalized that is the eigenvalues λ_1, λ_2 and λ_3 and the corresponding eigenvectors ν_1, ν_2 and ν_3 were calculated for each pixel. Fractional anisotropy (FA) maps and angle maps of the muscle fibres were derived from these data, where the direction of the muscle fibres relative to the magnet axis can be determined by the eigenvector corresponding to the largest eigenvalue that is the main diffusion direction.

3.3 Results

3.3.1 Eddy Current Correction

Geometric distortions caused by ECs were clearly visible in diffusion weighted subtraction images of the water phantom recorded without EC correction (Fig. 3a,c). In the diffusion weighted subtraction images acquired with the STE sequence, the distortion effects are less pronounced than in the images acquired with the SE sequence, but still with a maximal pixel displacement of 2-3 pixels. The strength and direction of the distortion depends on the direction of the diffusion gradient vectors. For the gradient vectors $\mathbf{e}_3$ and $\mathbf{e}_4$, a scaling effect can be observed in phase direction, whereas for the other directions mainly shearing effects due to field gradients in read-out direction are visible. The use of bipolar gradients in the STE-EPI sequence as described in the Methods section minimizes EC effects comparable to the SE-EPI sequence with EC correction (Fig. 3b,d). Average ADC and FA values were determined for both, the EC corrected SE-EPI and the STE-EPI sequences, to verify the accuracy and reproducibility of the new method. The average values of the ADC and FA are $2.27 \pm 0.02 \times 10^{-3}$ mm^2/s and 0.035 ± 0.008 for the SE-EPI sequence and 2.23 ± 0.02 mm^2/s and 0.033 ± 0.006 for the STE-EPI sequence at a magnet bore temperature of 24 °C. Distinct geometric distortions caused by ECs were visible in diffusion weighted images of the human calf musculature recorded without EC correction. For the diffusion gradients along the vectors $\mathbf{e}_1$ and $\mathbf{e}_2$ and $\mathbf{e}_5$ and

$\mathbf{e}_6$, respectively, significant differences in geometrical distortions can be observed in the images without EC correction as in Fig. 4a. Those effects occurred markedly in the lateral side of the calf. Effects of diffusion gradients along the vectors $\mathbf{e}_3$ and $\mathbf{e}_4$ were much less pronounced. Since the displacements of the tissue structures were clearly larger than the pixel size and the direction of the displacement depended on the applied orientation of diffusion sensitizing, proper calculation of diffusion maps was impossible using this approach. Corresponding images recorded with the proposed EC correction are demonstrated in Fig. 4b. Effects of remaining ECs are clearly less than the pixel size and do not disturb proper calculation of diffusion parameter maps.

Table 4: *Pennation angles of the muscles gastrocnemius medialis (GM), gastrocnemius lateralis (GL), soleus (SOL) and tibialis anterior (TA) for all four subjects (Sub). The values are in good agreement with literature [33, 34].*

Sub	GM	GL	SOL	TA
#1	26 ± 5	8 ± 4	36 ± 8	12 ± 4
#2	19 ± 7	17 ± 6	37 ± 8	12 ± 5
#3	24 ± 4	8 ± 3	36 ± 9	9 ± 3
#4	20 ± 7	13 ± 4	38 ± 7	9 ± 3

3.3.2 Parameter Maps

For anatomical orientation in the parameter maps, a corresponding T1-weighted image of the calf is shown in Fig. 5. Colour encoded FA maps calculated are presented in Fig. 6a. Representative FA values of the muscles GM, GL, SOL and TA of the four subjects are given in Table 3. The values were taken from one region of interest (ROI) in each muscle. The size of the ROIs varied from between 4 cm^2 to 9 cm^2. The positions of the ROIs were carefully chosen to avoid inclusion of vessels and not fully suppressed fat tissue. The FA seems to be slightly lower in

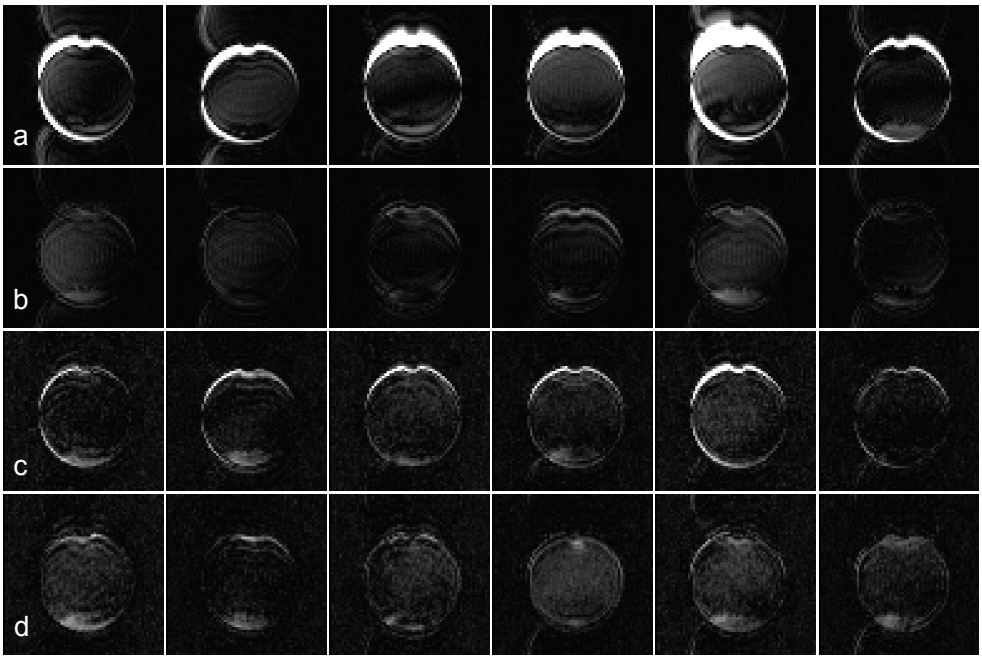

Figure 3: *Diffusion weighted images (b = 700 s/mm^2) and a non-weighted image (b = 0 s/mm^2) of a water phantom were acquired with an SE-EPI sequence without (a) and with EC correction (b) and with an STE-EPI sequence without (c) and with EC correction (d). All images were scaled to a range from 0 to 1 and the non-weighted image was subtracted from the corresponding weighted images. In (a)-(d) the absolute values of these subtraction images are depicted to illustrate the shift, scaling and shearing effects of the ECs depending on the diffusion gradient direction. The phase encoding direction was anterior - posterior. The vectors of the diffusion gradients were (1,0,1), (-1,0,1), (0,1,1), (0,1,-1), (1,1,0) and (-1,1,0) (from left to right). Eddy current induced distortion effects are less pronounced for the STE-EPI sequence in comparison to the SE-EPI sequence but nevertheless distinctive enough to hamper a correct calculation of the diffusion tensor and derived diffusion values.*

the muscles soleus and the gastrocnemius medialis compared to the other muscles in the human calf. Fibre orientation maps according to the main axis of the diffusion tensor in each pixel are shown in Fig. 6b and Fig. 6c. The orientation of

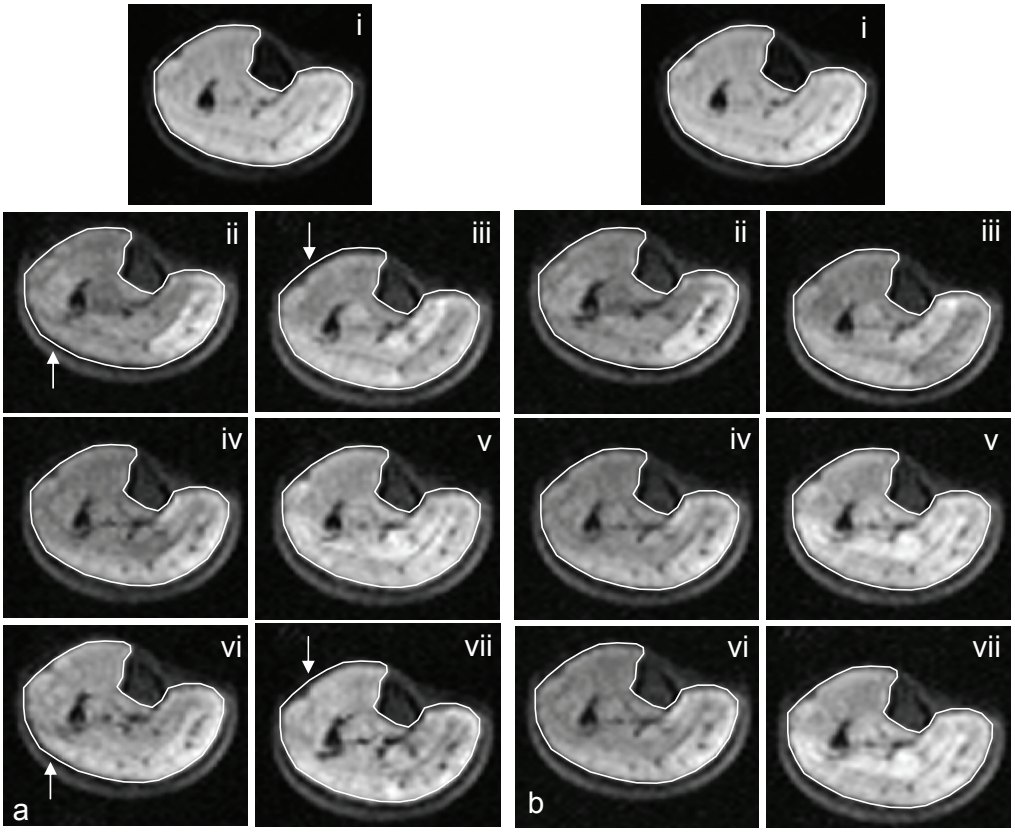

Figure 4: *Diffusion weighted images (b = 700 s/mm^2) (ii-vii) and a non-weighted image (b = 0 s/mm^2) (i) of human calf musculature obtained with an STE-EPI sequence without (a) and with (b) EC correction. Phase encoding direction was anterior – posterior. Diffusion directions were (1,0,1) (ii), (-1,0,1) (iii), (0,0,1) (iv), (0,0,-1) (v), (1,1,0) (vi), and (-1,1,0) (vii). The contour of the calf musculature of the corresponding image without diffusion weighting is indicated by a white line. EC correction is demonstrated in order to almost completely avoid undesired scaling distortions.*

the fibre is characterized by θ and ϕ maps, where θ and ϕ are the polar coordinates of the eigenvector v_1 belonging to the largest eigenvalue λ_1 of the diffusion tensor that is $v_1 = (\sin(\phi)\sin(\theta), \cos(\phi)\sin(\theta), \cos(\theta))$. The images reveal clear differences between the muscle groups for both, θ and ϕ angle of fibre orientations. With the aid of the angle θ, the pennation angle of each muscle can be determined. The pen-

Figure 5: *Transverse T1-weighted image of the human lower leg for anatomical orientation. The examined muscles are denoted by a white line. TA: M. tibialis anterior, GM: M. gastrocnemius medialis, GL: M gastrocnemius lateralis, SOL: M. soleus.*

nation angle denotes the angle between the line of action of the muscle - which is almost along the leg axis in the case of lower leg muscles - and the line of action of the fibres. The muscles SOL and GM have high pennation angles which allows them to produce more force for their size in comparison to the spindle shaped muscle TA, where the fibres are mainly parallel to the leg axis. Pennation angles of the TA, SOL, GM and GL of the four subjects are shown in Table 4 and are in good agreement with literature [33, 34]. Regarding the ϕ maps of fibre orientations, it is possible to further characterize the lower leg muscles. Whereas the fibres of the most leg muscles show a rather uniform orientation, the fibres of the SOL muscle are split up in two main sets of parallel fibres which are oriented in different planes approving the bipennate form of the SOL muscle.

Under rest conditions, the mean apparent diffusion coefficients were lowest in GL and highest in SOL. These deviations of GL and SOL are mainly based on a relatively low smallest eigenvalue λ_3 in GL and a distinctly high mean eigenvalue λ_2 in SOL for all volunteers. It should be noted that inter-individual deviations in the diffusion values of TA were relatively low for the four subjects, compared to the

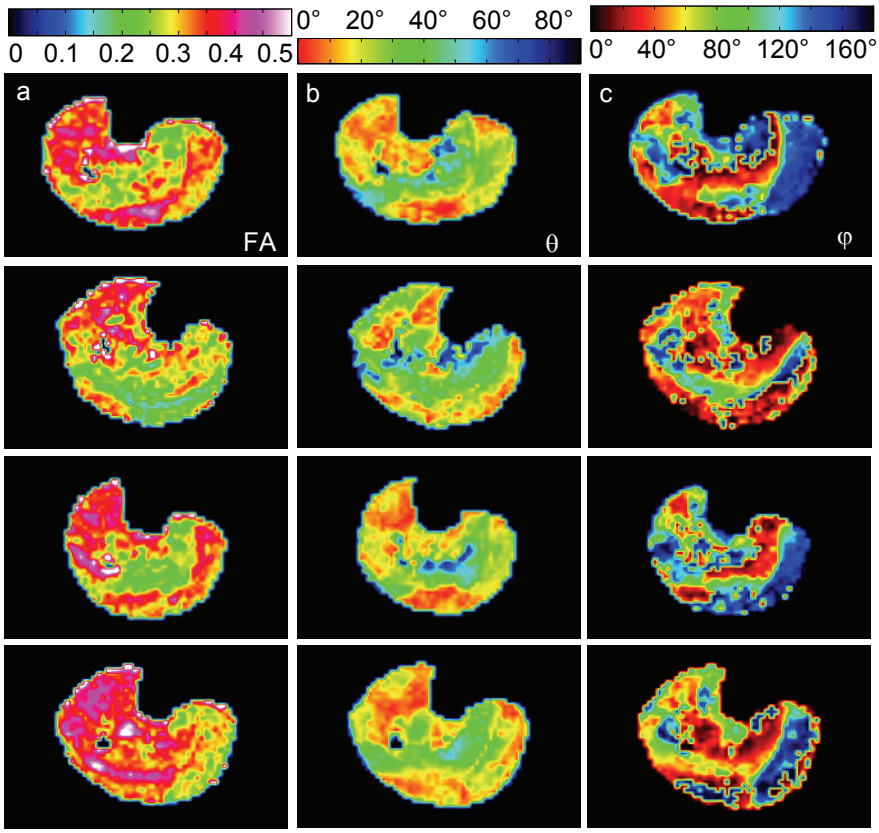

Figure 6: *FA and fibre orientation maps for all four subjects (rows). FA map (first column) expressed by* $FA = 3/2 \cdot \left((\lambda_1 - \lambda_{av})^2 + (\lambda_2 - \lambda_{av})^2 + (\lambda_3 - \lambda_{av})^2\right) / \sqrt{\lambda_1^2 + \lambda_2^2 + \lambda_3^2}$ *where* λ_{av} *denotes the mean value of the eigenvalues* λ_1, λ_2 *and* λ_3. *The FA is significantly lower in the SOL and GM in comparison to the other muscle groups. Fibre orientation maps* θ *(second column) and* ϕ *(third column) where* θ *denotes the angle between the fibre and the z axis and* ϕ *the angle in the xy plane between the fibre and the x axis.*

other muscles examined.

3.3.3 Workload Study

Effects of exhaustive exercise on diffusion properties and T2 relaxation times are summarized in Table A, which can be found in the Appendix. The trace and the

eigenvalues of the diffusion tensor for the muscles gastrocnemius medialis (GM), gastrocnemius lateralis (GL), soleus (SOL), and tibialis anterior (TA) are listed before and after exercise. For the GM, pronounced changes in both, the diffusion values and T2, could be observed after the exercise, whereas in the TA no significant modifications are visible after repeated standing on tiptoes. The temporal course of the ADC and of T2 during a period of 40 min. following the exercise and 2 hours after the exercise of one subject is shown in Fig. 7

The ADC seems to be not only influenced by the exercise itself but also by long lasting orthostatic regulation. This may explain the decrease of the ADC in the TA in period 2 and 3. Standard deviations of the values in the examined ROIs are indicated by error bars. All eigenvalues of the diffusion tensor of loaded muscles were significantly increased by 7-17% immediately after the exercise. Maximum increase (14-17%) was found in the smallest eigenvalue in muscles gastrocnemius lateralis and soleus.

3.4 Discussion

The proposed technique allows fast diffusion tensor imaging (DTI) of musculature with high quality. For this application, problems related to strong relaxation dependent signal losses in tissues with short T2 could be solved by introduction of an optimized stimulated echo diffusion preparation. Furthermore, variable distortions in single EPI diffusion images had to be avoided, since a pixel-wise evaluation of image series is necessary to calculate appropriate diffusion maps. A significant reduction of responsible eddy current effects of the stimulated echo preparation could be achieved by additional gradient pulses implemented during the mixing time TM. In contrast to former approaches with EC correction in spin echo preparations [26, 27], the compensation in the stimulated echo preparation works well without any disadvantages regarding prolonged sequence timing.

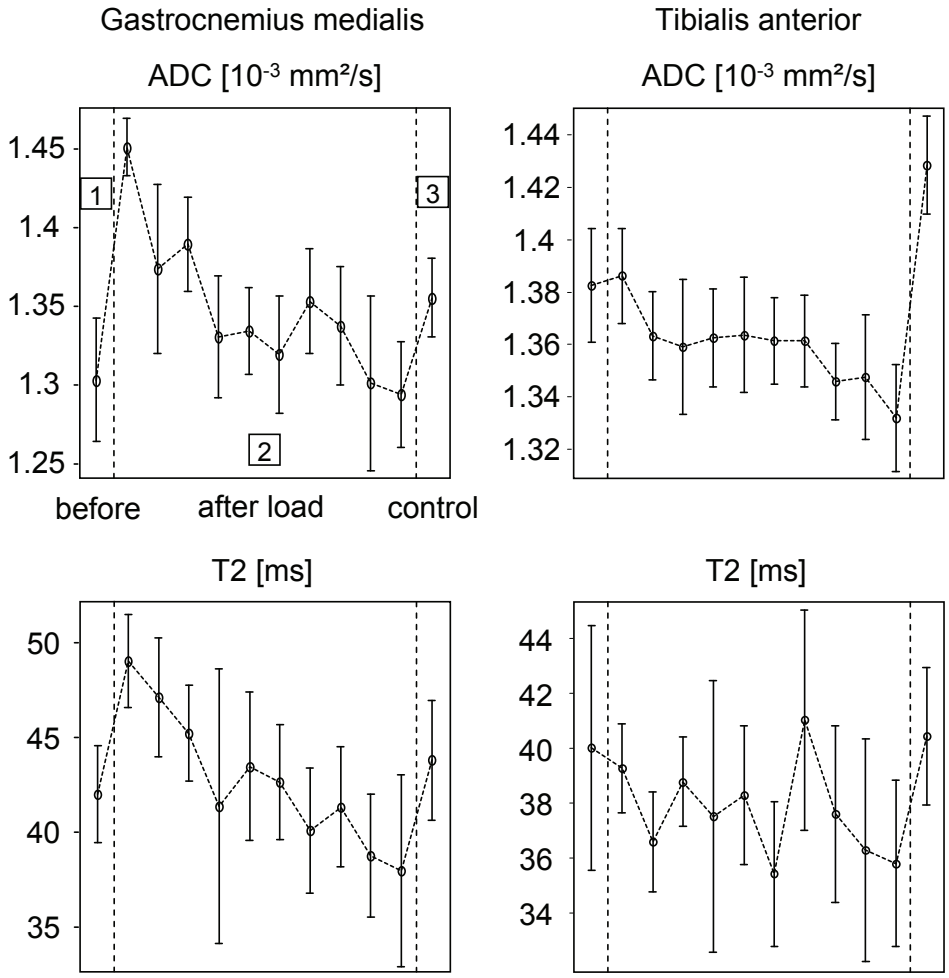

Figure 7: *The mean apparent diffusion coefficient (ADC) and T2 in the muscle gastrocnemius medialis (GM) and the muscle tibialis anterior (TA) for one subject before workload (1), during a period of 40 min following the exercise (2) and 2 hours after the exercise (3). The ADC seems to be not only influenced by the exercise itself but also by orthostatic regulation. This may explain the decrease of the ADC in the TA in period 2. Standard deviations of the values in the examined ROIs are indicated by error bars.*

Comparing the images of the phantom measurements acquired with the SE-EPI and the STE-EPI sequence without EC correction, it can be seen that the distortion effects for the STE sequence are less pronounced than for the SE sequence. An

explanation for this may be the clearly shorter duration of the diffusion gradients in the STE case compared with the SE case. For small durations of gradient switching, the EC induced by the rising ramp is partly eliminated by the corresponding EC with opposite sign induced by the falling ramp. Nevertheless, the distortions are strong enough to hamper an accurate calculation of the diffusion maps.

The extremity coil cannot be positioned in the centre of the bore, but has to be horizontally moved to clear a space for the other leg. Therefore, distortions mainly appear in the lateral outer part of the images. Since the coil is not only horizontally but also vertically positioned out of the centre because of constructional reasons, the distortions are more pronounced in the upper parts of the images. The ADC values determined with the SE-EPI and the STE-EPI are in good agreement among each other as well as with literature [9,35] considering a ~2.4% variation per degree Celsius change in temperature [36]. The FA values are also in the same range and too low to be differed from background noise as expected for an isotropic fluid.

In Sinha et al. [9], a tetrahedral diffusion gradient encoding scheme implemented in an SE-EPI was used to measure diffusion tensor in human calf musculature. The advantage of the tetrahedral encoding scheme is a gain of SNR per scan time by a factor of approximately 1.72 in comparison to an orthogonal encoding scheme. The SNR gain arises from the fact that the simultaneous application of the diffusion gradients along all three axes in comparison to along one axis provides an increase in effective gradient strength leading to an optimal b-value reached at a shorter TE. This method could be used for an STE preparation as well as in order to gain more SNR by a change from a cubic to a tetrahedral encoding scheme. However, for an STE preparation, the gain of SNR using a tetrahedral encoding scheme is much less pronounced than for an SE preparation. It was derived from Eqs. 3.5 and 3.6 that for the parameters T2 = 30 ms, T1 = 1100 ms and $D = 1.6 \times 10^{-3}$ mm^2/s and for the circumstances reported in the Methods, the SNR of the diffusion map reaches its maximum for the cubic encoding scheme at TE = 33 ms and TM = 182 ms and for

the tetrahedral encoding scheme at TE = 31 ms and TM = 145 ms (the latter would lead to a theoretical SNR gain of only 11%). Apart from this minimal gain in SNR, tetrahedral encoding cannot be used to determine the whole diffusion tensor but only the trace and the off-diagonal elements, since the condition of axial symmetry is not full-filled for the muscles of the lower leg as shown in Table 2.

While the θ maps expressing the angle between the muscle fibres and the leg axis show a good agreement between the four subjects, the variations of the FA and the angle ϕ are distinctly higher. Nevertheless, all three values seems to be rather homogeneous within the different muscle groups.

Fibre tracking using DTI can be successfully used to visualize white matter neuron bundles in the human brain [37]. Damon et al. [38] and Heemskerk et al. [33] have extended this technique to animal skeletal musculature and shown that DTI is a reliable tool to determine fibre geometry and orientation *in vivo*.

In a recent work [34], it was shown that the application of DTI-based fibre tracking is also suitable for human muscles. Galban et al. [34] measured changes in the pennation angle and fibre length due to contraction in the human SOL. The pennation angles for the SOL found in our work are comparable to the values in [34] and also the pennation angles for the TA, GM and GL of the four subjects shown in Table 4 are in good agreement with literature values [39, 40] obtained with ultrasonography.

A further aim of this work was the examination of exercise-induced changes of diffusion properties in human skeletal musculature and their temporal course after the exercise. For this purpose, the diffusion weighted STE-EPI sequence was optimized and a time resolution of less than two minutes could be obtained. Diffusion values increased significantly in the muscles of the posterior compartment of the lower leg, namely GM, GL and SOL. These muscles are mostly loaded for rapid movements during walking, running and jumping or, as in our case, for standing on tiptoe.

The TA muscle — together with other muscles in the anterior compartment of the lower leg — primarily extends the toes and dorsiflexes the ankle. For this reason, TA should not be markedly strained in the exercise and no significant changes of the diffusion values were found in this muscle with the exception of subject #3. It seems possible that this subject performed a slight dorsal flexion of the ankle during exercise.

Comparing the diffusion values for GM, GL and SOL in Table A of the Appendix, it is apparent that the induced increase of diffusion values in the particular muscles was not uniform in the four subjects. The high variation may be explained by the fact that modifications of the diffusion properties may be dependent on many factors such as gender, age, the individual training status and the individual fibre type composition of fast and slow twitch fibres of the different muscles. Moreover, the increase of the eigenvalues was not always isotropic. A distinct increase of the largest eigenvalue λ_1 that is an increase of the diffusion in direction of the muscle fibres could always be observed, whereas the mean eigenvalue λ_2 and/or the smallest eigenvalue λ_3 which both describe the diffusion perpendicular to the direction of the muscle fibres did not show a significant change especially for subjects #3 and #4.

As mentioned in the introduction, a workload exercise leads to the formation of a new distribution of water molecules in skeletal musculature. An animal model revealed a bi-exponential behaviour of T2 decay curves in oedematous muscle [28] with a fast relaxation time of approximately 20-40 ms and a slow relaxation time of about 150-400 ms, possibly assigned to intra- and extracellular water protons, respectively. Using only a mono-exponential fit procedure, the enlargement of the compartment with longer T2 may be the reason for the significant increase of signal intensity in T2-weighted images. In another study [29], a rat muscle oedema model was used to examine both diffusion and T2 relaxation decay in oedematous and normal muscle. Not only oedematous musculature showed bi-exponential T2-

decay, but also normal musculature.

In our study, the time course of the trace and the eigenvalues of the diffusion tensor were correlated with the temporal changes of the T2 values. Both effects showed very similar time courses supporting the hypothesis of similar underlying mechanisms for the changes of both, T2 relaxation and diffusion. Considering recent literature [28, 29] with bi-exponential diffusion and T2 relaxation decay in musculature, it seems reasonable that exercise leads to changed volume shares in two major tissue compartments with slow water exchange. However, further investigations are necessary to confirm this model.

Potential future applications of DTI studies in skeletal musculature may be the assessment of myopathologies and physiological regulation processes in muscles. Furthermore, short term and long term individual training effects on musculature could be studies using the proposed approach where the proposed STE-EPI approach is especially helpful for investigations with higher b-values.

3.5 Conclusions

A diffusion weighted EPI sequence with stimulated echo preparation has been presented, which significantly reduces eddy current induced image distortions without increase of measuring time or additional post processing for correction of acquired images. Diffusion parameters in calf musculature were investigated with this method. Parameter maps from the trace and the three eigenvalues of the diffusion tensor, FA maps and angle maps describing the orientation of the muscle fibres being identical with the diffusion direction of the largest eigenvalue could be derived. For both FA and muscle fibre orientation, obvious differences for the miscellaneous muscle groups could be observed, whereas the eigenvalues of the diffusion tensor seem to be rather homogeneous in the whole calf musculature. Potential clinical

applications of DTI studies in skeletal musculature may be the assessment of myopathologies and physiological regulation processes in muscles.

References

[1] Bihan, D. Le, R. Turner and J.R. Macfall: *Effects of intravoxel incoherent motions (IVIM) in steady-state free precession (SSFP) imaging: application to molecular diffusion imaging*. Magn. Reson. Med., 10:324–337, 1989.

[2] Pierpaoli, C., P. Jezzard, P.J. Basser, A. Barnett and G. Di Chiro: *Diffusion tensor MR imaging of the human brain*. Radiology, 201:637–648, 1996.

[3] Cleveland, G.G., D.C. Chang, C.F. Hazlewood and H.E. Rorschach: *Nuclear magnetic resonance measurement of skeletal muscle: anisotropy of the diffusion coefficient of the intracellular water*. Biophys. J., 16:1043–1053, 1976.

[4] Reese, T.G., R.M. Weisskoff, R.N. Smith, R. Rosen, R.E. Dinsmore and J. van Wedeen: *Imaging myocardial fiber architecture* in vivo *with magnetic resonance*. Magn. Reson. Med., 34:786–791, 1995.

[5] Doorn, A. van, P.H. Bovendeerd, K. Nicolay, M.R. Drost and J.D. Janssen: *Determination of muscle fiber orientation using diffusion weighted MRI*. Eur. J Morphol., 34:5–10, 1996.

[6] Müller, M.F., P.V. Prasad, B. Siewert and R.R. Edelman: *The* in-vivo *diffusion measurements of the liver, kidneys, spleen and m. erector with an echo-planar imaging system in normal subjects*. Rofo. Fortschr. Geb. Rontgenstr. Neuen. Bildgeb. Verfahr., 161(3):233–236, 1994.

[7] Müller, M.F., P.V. Prasad, D. Bimmler, A. Kaiser and R.R. Edelman: *Functional imaging of the kidney by means of measurement of the apparent diffusion coefficient*. Radiology, 193(3):711–715, 1994.

[8] Ries, M., R.A. Jones, F. Basseau, C.T.W. Moonen and N. Grenier: *Diffusion tensor MRI of the human kidney*. J. Magn. Reson. Imaging, 14:42–49, 2001.

[9] Sinha, U. and L. Yao: In vivo *diffusion tensor imaging of human calf muscle*. J. Magn. Reson. Imaging, 15:87–95, 2002.

[10] Vermathen, P., C. Boesch and R. Kreis: *Mapping fiber orientation in human muscle by proton MR spectroscopic imaging*. Magn. Reson. Med., 49:424–432, 2003.

[11] Dietrich, O., J.G. Raya, J. Sommer, M. Deimling, M.F. Reiser and A. Baur-Melnyk: *A comparative evaluation of a RARE-based single-shot pulse sequence for diffusion-weighted MRI of musculoskeletal soft-tissue tumors*. Eur. Radiol., 15:772–783, 2005.

[12] Morvan, D., A. Leroy-Willig, A. Malgouyres, C.A. Cuenod, P. Jehenson and A. Syrota: *Simultaneous temperature and regional blood volume measurements in human muscle using an MRI fast diffusion technique*. Magn. Reson. Med., 29:371–377, 1993.

[13] Gilbert, R.J. and V.J. Napadow: *Three-dimensional muscular architecture of the human tongue determined in vivo with diffusion tensor magnetic resonance imaging*. Dysphagia, 20:1–7, 2005.

[14] Mori, S. and P.C. Van-Zijl: *A motion correction scheme by twin-echo navigation for diffusion-weighted magnetic resonance imaging with multiple RF echo acquisition*. Magn. Reson. Med., 40:511–516, 1998.

[15] Schick, F., B. Eismann, W.-I. Jung, H. Bongers, M. Bunse and O. Lutz: *Comparison of localized proton NMR signals of skeletal muscle and fat tissue* in vivo*: two lipid compartments in muscle tissue*. Magn. Reson. Med., 29:158–167, 1993.

[16] Fisher, M.J, R.A. Meyer, G.R Adams, J.M. Foley and E.J. Potchen: *Direct relationship between proton T2 and exercise intensity in skeletal muscle MR images*. Invest. Radiol., 25:480–485, 1990.

[17] Ploutz-Snyder, L.L., S. Nyren, T.G. Cooper, E.J. Potchen and R.A. Meyer: *Different effects of exercise and edema on T2 relaxation in skeletal muscle*. Magn. Reson. Med., 37:676–682, 1997.

[18] Haselgrove, J.C. and J.R. Moore: *Correction for distortion of echo-planar images used to calculate the apparent diffusion coefficient*. Magn. Reson. Med., 36:960–964, 1996.

[19] Calamante, F., D.A. Porter, D.G. Gadian and A. Conelly: *Correction for eddy current induced B0 shifts in diffusion-weighted echo-planar imaging*. Magn. Reson. Med., 41:95–102, 1999.

[20] Papadakis, N.G., K.M. Martin, J.D. Pickard, L.D. Hall, T.A. Carpenter and C.L.-H. Huang: *Gradient preemphasis calibration in diffusion-weighted echo-planar imaging*. Magn. Reson. Med., 44:616–624, 2000.

[21] Koch, M. and D.G. Norris: *An assessment of eddy current sensitivity and correction in single-shot diffusion-weighted imaging*. Phys. Med. Biol., 45:3821–3832, 2000.

[22] Rohde, G.K., A.S. Barnett, P.J. Basser, S. Marenco and C. Pierpaoli: *Comprehensive Approach for correction of motion and distortion in diffusion-weighted MRI*. Magn. Reson. Med., 51:103–114, 2004.

[23] Shen, Y., D.J. Larkman, S. Counsell, I.M. Pu and D. Edwards J.V. Hajnal: *Correction of high-order eddy current induced geometric distortion in diffusion-weighted echo-planar images*. Magn. Reson. Med., 52:1184–1189, 2004.

[24] Bodammer, N., J. Kaufmann, M. Kanowski and C. Tempelmann: *Eddy current correction in diffusion-weighted imaging using pairs of images acquired with opposite diffusion gradient polarity*. Magn. Reson. Med., 51:188–193, 2004.

[25] Papadakis, N.G., T. Smponias, J. Berwick and J.E.W. Mayhew: *k-space correction of eddy-current-induced distortions in diffusion-weighted echo-planar imaging*. Magn. Reson. Med., 53:1103–1111, 2005.

[26] Alexander, A.L., J.S. Tsuruda and D.L. Parker: *Elimination of eddy current artifacts in diffusion-weighted echo-planar images: The use of bipolar gradients*. Magn. Reson. Med., 38:1016–1021, 1997.

[27] Reese, T.G., O. Heid, R.M. Weisskoff and V.J. Wedeen: *Reduction of eddy-current-induced distortion in diffusion MRI using a twice-refocused spin echo*. Magn. Reson. Med., 49:177–182, 2003.

[28] Gambarota, G., B.E. Cairns, C.B. Berde and R.V. Mulkern: *Osmotic effects on the T_2 relaxation decay of* in vivo *muscle*. Magn. Reson. Med., 46:592–599, 2001.

[29] Ababneh, Z., H. Beloeil, C.B. Berde, S.E. Maier and R.V. Mulkern: *Biexponential parametrization of diffusion and T2 relaxation decay curves in a rat muscle edema model*. 21th Annual Scientific Meeting of the ESMRMB, 16(Suppl 1):285, 2004. Electronic Supplement to MAGMA.

[30] Basser, P.J., J. Mattiello and D. Le Bihan: *MR diffusion tensor spectroscopy and imaging*. Biophys. J., 66:259–267, 1994.

[31] Gudbjartsson, H. and S. Patz: *The Rician distribution of noisy MRI data*. Magn. Reson. Med., 34:910–914, 1995.

[32] Sijbers, J., A.J. den Dekker, E. Raman and D. van Dyck: *Parameter estimation from magnitude MR images*. Int. J. Imag. Syst. Tech., 10:109–114, 1999.

[33] Heemskerk, A.M., G.J. Strijkers, A. Vilanova, M.R. Drost and K. Nicolay: *Determination of mouse skeletal muscle architecture using three-dimensional diffusion tensor imaging*. Magn. Reson. Med., 53:1333–1340, 2005.

[34] Galban, C.J., S. Maderwald, A. de Greiff, K. Uffmann and M.E. Ladd: *Calculation of muscle fiber orientation and length in human soleus by diffusion tensor imaging*. Proc. Intl. Soc. Mag. Reson. Med., 12:775, 2004.

[35] Mills, R.: *Self-diffusion in normal and heavy water in the range of 1-45°C*. J. Chem. Phys., 77:685–688, 1973.

[36] Bihan, D. Le, R. Delannoy and R.L. Levin: *Temperature mapping with MR imaging of molecular diffusion: application of hyperthermia*. Radiology, 171:853–857, 1989.

[37] Bihan, D. Le, J.F. Mangin, C. Poupon, C.A. Clark, S. Pappata, N. Molko and H. Chabriat: *Diffusion tensor imaging: concepts and applications*. J. Magn. Reson. Imaging, 13:534–546, 2001.

[38] Damon, B.M., Z. Ding, A.W. Anderson, A.S. Freyer and J.C. Gore: *Validation of diffusion tensor MRI-based muscle fiber tracking*. Magn. Reson. Med., 48:97–104, 2002.

[39] Maganaris, C.N.: *Force-length characteristics of in vivo human skeletal muscle*. Acta. Physiol. Scand., 172:279–285, 2001.

[40] Chow, R.S., M.K. Medri, D.C. Martin, R.N. Leekam, A.M. Agur and N.H. McKee: *Sonographic studies of human soleus and gastrocnemius muscle architecture: gender variability*. Eur. J. Appl. Physiol., 82:236–244, 2000.

4 Diffusion Imaging of Adipose Tissue in the Lower Leg*

Diffusion weighted spin-echo echo planar imaging was developed and applied for assessment of diffusion coefficients of adipose tissue in human lower leg on a 1.5 Tesla whole-body MR scanner. Due to the higher molecular weight of triglycerides, apparent diffusion coefficients (ADC) of adipose tissue are approximately two orders of magnitude smaller compared to water, leading to the necessity of using high b-values up to 50000 s/mm^2 and an echo time TE of 240 ms for sufficient diffusion-related signal attenuation. ADC maps of adipose tissue in the human lower leg were derived for diffusion encoding along orthogonal spatial directions in six healthy volunteers. Mean diffusion coefficients in the tibial bone marrow amounted to $(1.81 \pm 0.10) \times 10^{-5}$ mm^2/s (left-right), $(1.96 \pm 0.10) \times 10^{-5}$ mm^2/s (anterior-posterior) and $(1.96 \pm 0.20) \times 10^{-5}$ mm^2/s (head-feet), respectively. Pixel-wise calculated ADC values of subcutaneous adipose tissue showed a distinctly higher variation with the smallest ADC values similar to those measured for tibial bone marrow. Some subcutaneous adipose tissue regions showed increased signal attenuation at higher b-values resulting in ADC coefficients up to 4.2×10^{-5} mm^2/s. It must be noted that diffusion measurements with extremely high b-values *in vivo* are extremely sensitive to incoherent motion effects in tissue. Nonetheless, it could be shown that *in vivo* diffusion imaging of adipose tissue in human lower leg is possible at 1.5 Tesla in acceptable measurement time of a few minutes. Potential future applications of fat diffusion imaging are seen in temperature measurements in adipose tissue, detection of free fatty acids in white or brown adipose tissue in case of high lipolysis, differentiation of macro- and microvesicular steatosis or assessment of the mobility of intramyocellular lipids (IMCL).

*This Chapter was adapted from: Steidle G, Eibofner F, Schick F. Quantitative diffusion imaging of adipose tissue in the human lower leg at 1.5 T. Magn Reson Med 2011;65(4):1118-1124.

4.1 Introduction

MR diffusion weighted imaging (DWI) has widely been used over the past decades in order to measure molecular water diffusion *in vivo*. DWI has been proven a powerful non-invasive tool providing additional information about microscopic tissue compartments, structural anisotropy and pathology of tissues [1–12]. Additionally, diffusion properties of some metabolites with small molecular mass were shown to be accessible using diffusion weighted MR spectroscopy [13].

It is well known that MR imaging exclusively reflects signal contributions from water and fat molecules. In contrast to water containing tissues, adipose tissue does not show any relevant signal attenuation using common b-values up to 2000 s/mm^2. The reason for the low sensitivity of adipose tissue to diffusion preparation in MRI is the difference in molecular weight between water and fat: fatty compounds in adipose tissue consist mainly of triglyceride molecules with a molecular mass of approx. 900 - 1000 u, compared to only 18 u for water. In triglycerides, glycerol is esterified with three fatty acids of different chain lengths and degrees of saturation. The composition and the amount of free fatty acids with clearly lower molecular weight than triglycerides are potentially interesting features of adipose tissue [14].

Besides temperature, the diffusion coefficient of fat molecules mainly depends on the molecular mass. In general, the diffusion coefficient of triglycerides is about two orders of magnitude smaller than the diffusion coefficient of water. For this reason, relatively high maximum b-values of approx. 50000 s/mm^2 are necessary to provide a diffusion related signal attenuation of clearly more than 50 %. Doing so, accurate assessment of the diffusion properties of adipose tissue seems feasible.

To ensure accurate assessment of diffusion coefficients *in vivo*, techniques should be insensitive to motion artefacts. Single-shot echo planar imaging (EPI) is rather robust even under conditions involving slight coherent motion of the tissue under

investigation and is therefore mainly used for DWI examinations. An alternative method for diffusion weighted imaging is line scan diffusion imaging (LSDI) [15, 16], which was used for fat diffusion measurements in rat bone marrow by Ababneh et al. [17]. LSDI is also relatively insensitive to motion artifacts and even less sensitive to eddy current effects compared to EPI, but longer measurement time and limited signal-to-noise ratio (SNR) have to be taken into account. In another study [18], a diffusion weighted single-voxel spectroscopic stimulated echo acquisition mode (STEAM) technique with b-values up to 80000 s^2/mm was applied to measure diffusion properties of aliphatic organic compounds of fatty tissue in human bone marrow and of intra- and extracellular lipids in skeletal muscle.

Extended body compartments with pure adipose tissue suitable for diffusion sensitive MR examinations are (yellow) bone marrow of adults, subcutaneous and visceral fat. In the present work, a diffusion weighted twice-refocused spin echo EPI sequence as introduced by Reese et al. [19] was modified and adapted to diffusion imaging of adipose tissue of the lower leg in a 1.5 T whole body scanner. Additional studies *in vitro* on samples containing 1-butanol and oleic acid were conducted in order to test the methodical approach.

Diffusion imaging of fatty components could play a role in the field of characterization of white and brown adipose tissue and in temperature measurements. On the other hand, diseased organ parenchyma with high amount of fat (as in liver steatosis or in musculature with fatty degeneration) could be probably characterized regarding their microscopic spatial and chemical composition.

4.2 Material and Methods

4.2.1 Experimental

All experiments and examinations were performed on a 1.5 T whole-body MR unit (Magnetom Sonata, Siemens Healthcare, Erlangen, Germany). For signal detection, a transmit/receive extremity coil of the manufacturer was employed.

On a whole body scanner, long-lasting diffusion gradient pulses with high amplitudes are necessary to achieve b-values up to 50000 s/mm^2. Those gradient pulses induce distinct eddy currents (EC) even in systems with actively shielded gradient coils. Unfortunately, due to the low bandwidth of EPI sequences in phase encoding direction, those ECs might cause significant spatial distortions in the images, dependent on the direction of the applied diffusion gradients. To minimize such undesired image distortion effects, a twice-refocused spin-echo EPI sequence was applied as introduced in [19]. In this sequence, spin-echo diffusion sensitizing is performed by two 180° refocusing pulses and four diffusion sensitizing gradients with optimized durations: By appropriate adjustment of the timing of these diffusion sensitizing gradients, ECs with a certain exponential decay constant can be nulled, and ECs with similar decay constants can be significantly reduced. For water diffusion measurements with lower b-values, this approach has been shown to generate clearly less distortion in diffusion weighted images improving imaging quality of derived diffusion maps [19].

To avoid spatially shifted and disturbing signals caused by double bonds of fat molecules (and of water for lower b-values as present for *in vivo* measurements), all studies were performed using spectrally selective excitation. For this purpose, a series of six equidistant sinc pulses, separated by a delay of 2.4 ms, with an alternating binomial distribution of the flip angles and with monopolar switching of the slice gradients was used for spatial-spectral excitation in the chemical shift range

of methylene and methyl protons of fatty acids. The field of view was chosen sufficiently large to avoid intersections of disturbing signals caused by N/2 ghosts with the basic signal in all experiments.

For all measurements, partial Fourier technique in phase encoding direction was applied with a factor of 6/8 in order to decrease minimal echo time. Before averaging and Fourier transformation in phase direction, linear phase changes were automatically corrected in each raw data set by the customer's image reconstruction software using additional phase correction scans.

4.2.2 *In Vitro* Studies

Diffusion imaging was performed in two liquid organic compounds with different molecular weight filled in plastic bottles with a content of 1 liter and a diameter of 80 mm. Bottles were placed horizontally inside the extremity coil parallel to the scanner bore axis.

The two compounds were oleic acid ($CH_3(CH_2)_7CH{=}CH(CH_2)_7COOH$) and 1-butanol ($CH_3(CH_2)_3OH$) with chain lengths of 18 and 4, respectively, and molecular weight of 282 and 74 u, respectively. For all measurements, temperature was in the range between 22.2 °C and 22.5 °C.

For oleic acid, the sequence parameters used were according to the *in vivo* examinations as described below: pulse repetition time TR = 1500 ms, echo time TE = 240 ms, matrix 128 x 128, field of view (FoV) 256 x 256 mm^2, receiver bandwidth = 1502 Hz/pixel, and eight averages. Data were acquired with 16 equally spaced b-values from 0 to 50000 s/mm^2, with a maximal diffusion gradient strength of 32.2 mT/m. Since a twice-refocused sequence [19] was used for diffusion weighting (instead of a common Stejskal-Tanner sequence), the b-value depends on four different time elements δ_1, δ_2 ,δ_3 and δ_4, rather than the usual diffusion times δ and Δ. For a TE of 240 ms, following time elements were applied: δ_1 = 52.66 ms,

δ_2 = 51.18 ms, δ_3 = 68.82 ms and δ_4 = 35.02 ms. For this choice of timing, eddy currents with an exponential time constant of 100 ms and their effects can be nulled.

For 1-butanol with its lower molecular weight, the echo time TE was decreased to 140 ms and data were acquired with 16 equally spaced b-values from 0 to 5000 s/mm^2 with a maximal diffusion gradient strength of 29.9 mT/m. Resulting time elements for appropriate diffusion weighting were δ_1 = 20.00 ms, δ_2 = 33.84 ms, δ_3 = 36.16 ms and δ_4 = 17.68 ms.

One transverse slice with 6 mm thickness was chosen for all *in vitro* measurements. Three experiments were performed, each of them with the direction of the diffusion sensitizing gradients along one of the three orthogonal scanner axes. Total measurement time was 3:17 min for one diffusion direction.

For diffusion analysis, circular regions of interest (ROI) with a diameter of about 50 mm were centrally placed within the bottle and signal intensity against b-value curves were extracted for every pixel inside the ROI.

4.2.3 *In Vivo* Studies

Six healthy male volunteers (mean age 36 ± 9 years, body mass index 24.6 ± 3.2 kg/m^2) were scanned for *in vivo* diffusion measurements of adipose tissue in the lower leg. All volunteers gave written informed consent prior to the examinations.

As a first step, multiple axial T1-weighted images of the right lower leg (turbo spin echo sequence with TR = 650 ms, TE =16 ms, 6 mm slice thickness, matrix size 256 x 256, FoV 180 x 180 mm^2, receiver bandwidth = 250 Hz/pixel, echo train length 3, and axial orientation) were recorded. For *in vivo* diffusion imaging, one single slice with 6 mm thickness was chosen positioned at the level with maximum cross-sectional area of the calf. Further sequence parameters of the twice-refocused

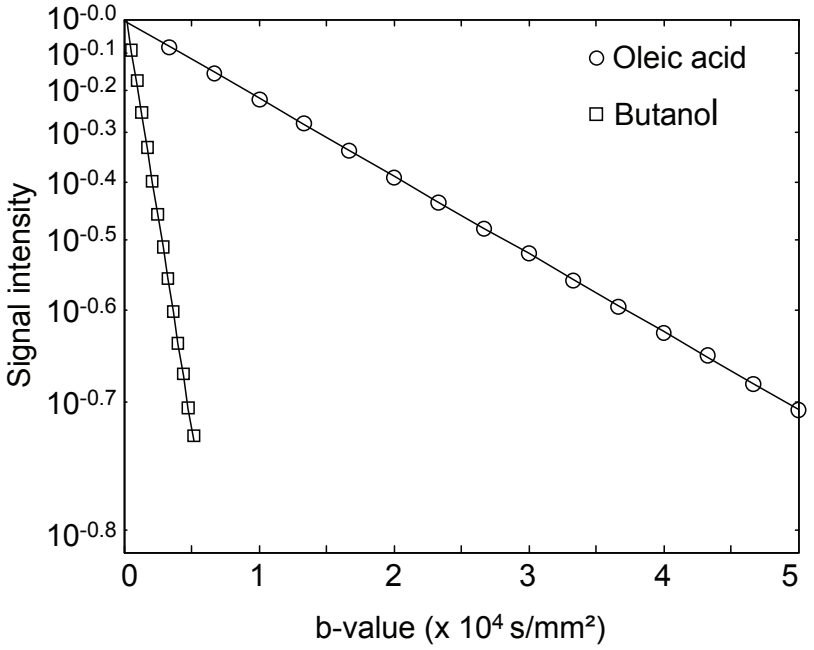

Figure 1: *Semilogarithmic plots of the signal decay against the b-factor from oleic acid and 1-butanol. Solid lines show the mono-exponential fits to the data. Diffusion weighting was along the body axis, yielding diffusion coefficients of (3.36 ± 0.09) × 10^{-5} mm^2/s and (42.0 ± 1.2) × 10^{-5} mm^2/s, respectively.*

spin-echo EPI sequence were TR = 1500 ms, TE = 240 ms, matrix 128 x 128, FoV 256 x 256 mm^2, receiver bandwidth = 1502 Hz/pixel, and eight averages.

To enhance the accuracy of apparent diffusion coefficient (ADC) measurements, data were acquired with 64 instead of 16 equally spaced b-values (as chosen for the *in vitro* experiments) from 0 to 50000 s/mm^2 with a maximal diffusion gradient strength of 32.1 mT/m. Directions of the diffusion gradients were strictly parallel and orthogonal along the main axes of the scanner. Total measurement time was 12:53 min for one diffusion direction.

A maximal b-value of 50000 s/mm^2, which is approximately the inverse of the expected diffusion coefficient, was used for the *in vivo* experiments to obtain distinct signal attenuation for higher b-values. Evaluation of mean ADC values was

performed in ROIs located within the tibial bone marrow, where pixels containing marginal vessels were excluded. Further ROIs were selected in areas of pure subcutaneous adipose tissue and analysed appropriately.

4.2.4 Post-Processing

Diffusion weighted images were analysed offline on a PC using home-made routines written with Matlab (The Mathworks, Inc., Natick, MA, USA). After signal averaging, noise correction was applied to the magnitude signal S_{orig} of each picture element with $S_{\text{corr}} = \sqrt{\left|S^2_{\text{orig}} - \sigma^2\right|}$ where σ^2 is the variance of the noise [20]. For σ^2, an unbiased estimator with minimum variance can be derived by $\sigma^2 = \frac{1}{2}\left\langle R^2 \right\rangle$, where $\left\langle R^2 \right\rangle$ is the spatial average of the squared magnitude data out of a region in the image without MR proton signals [21]. To avoid artificial values in the ADC maps in regions outside the object under measurement (plastic bottle for the *in vitro* measurements and lower leg for the *in vivo* measurements) and to save computing time, a binary filter was applied, which considered only pixels containing signal of the object. The binary filter was defined by a polygon, tracing the outer contours of the object. For the pixels outside the polygon, signal was set to zero. A pixel wise fit with an exponential function was applied to calculate the ADC values for the three diffusion directions. For a better visualization, ADC-maps were color-encoded. Mean ADCs were calculated for the selected ROIs within bone marrow and subcutaneous adipose tissue.

4.3 Results

Diffusion experiments performed *in vitro* in fluids consisting of a well-defined chemical compound revealed logarithmic signal attenuation for increasing b-values. Fig. 1 shows semilogarithmic plots of the signal decay against the b-value from oleic acid and 1-butanol. Signals were taken from circular ROIs with a diameter of about

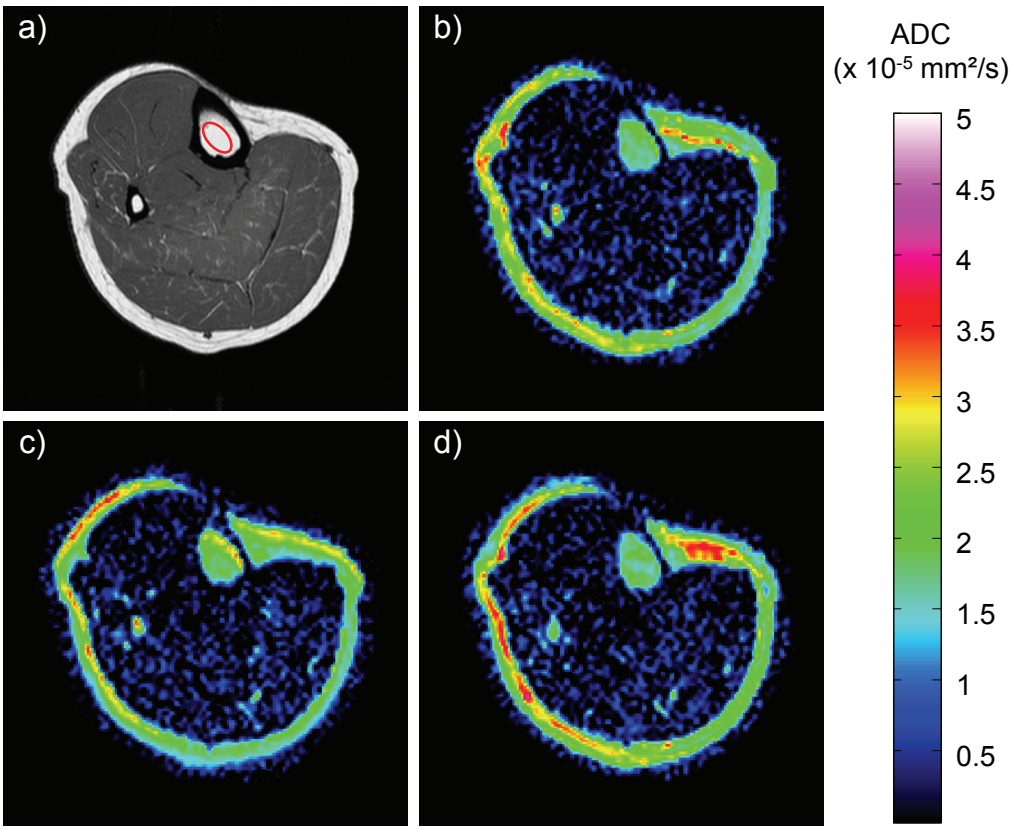

Figure 2: *Transversal images of the lower leg of one volunteer: T1-weighted image for anatomical orientation a). ADC maps determined from the diffusion weighted images in left-right- b), anterior-posterior- c) and head-feet- direction d). The ROI for evaluation of the ADC within the tibial bone marrow is indicated by a red ellipse in Figure part a).*

50 mm centrally placed within the plastic bottles filled with the two organic compounds, respectively. Solid lines show the monoexponential linear fits, which are in good agreement with the measured data. Diffusion weighting along the magnet axis yielded ADCs of (3.36 ± 0.09) × 10^{-5} mm^2/s and (42.0 ± 1.2) × 10^{-5} mm^2/s for oleic acid and 1-butanol, respectively. Diffusion weighting in perpendicular direction led to comparable results with ADCs of (3.46 ± 0.11) × 10^{-5} mm^2/s (horizontal) and (3.37 ± 0.10) × 10^{-5} mm^2/s (vertical) for oleic acid and (40.5 ± 1.2) × 10^{-5} mm^2/s (horizontal) and (41.3 ± 1.2) × 10^{-5} mm^2/s (vertical) for 1-butanol,

respectively.

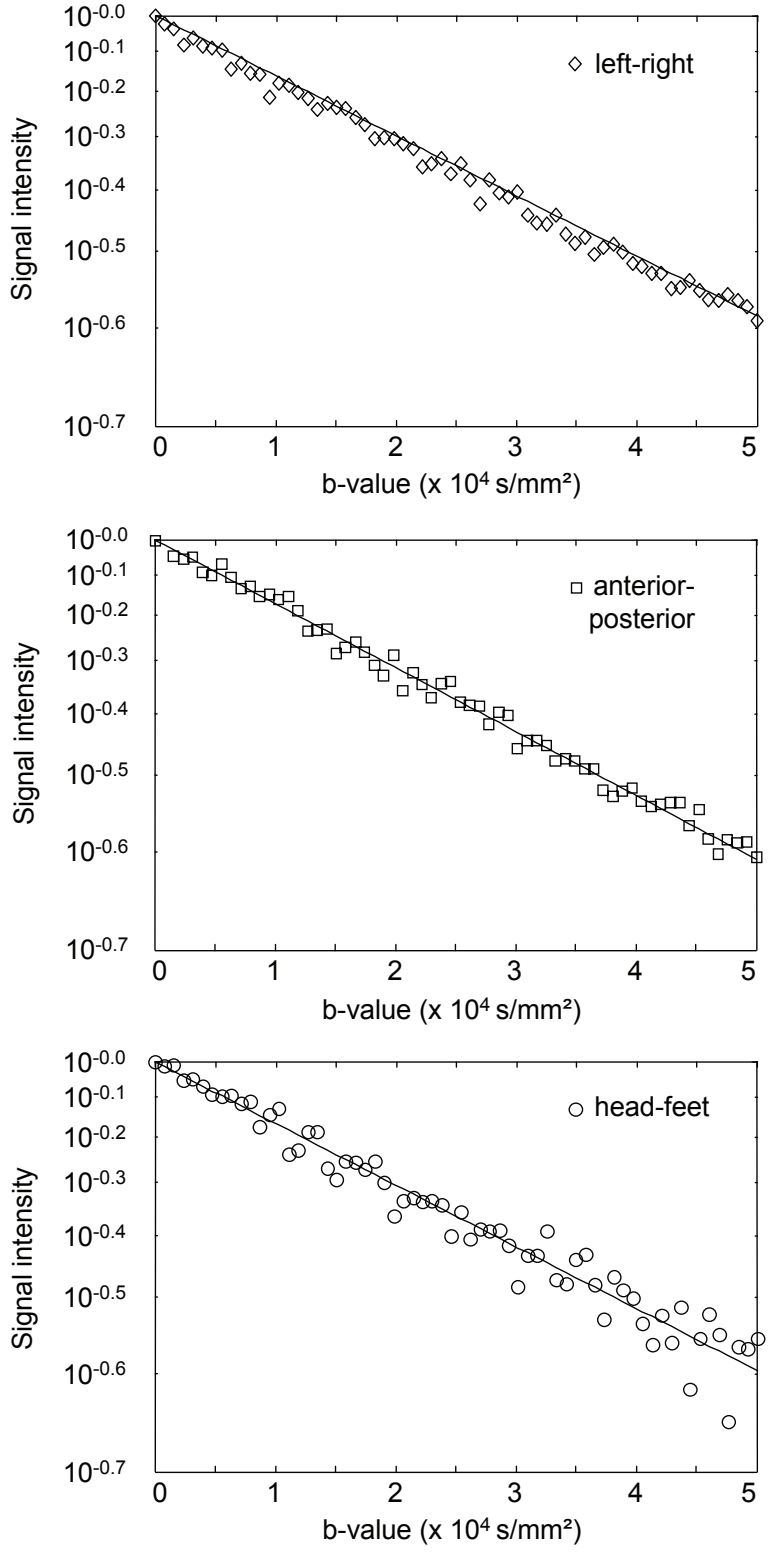

Figure 3: *Semilogarithmic plots of the signal decay against the b-value from ROIs within tibial bone marrow of one volunteer for all three diffusion directions. Solid lines show the mono-exponential fits to the data, yielding diffusion coefficients of* $(1.69 \pm 0.11) \times 10^{-5}$ *mm²/s,* $(1.86 \pm 0.13) \times 10^{-5}$ *mm²/s and* $(1.81 \pm 0.16) \times 10^{-5}$ *mm²/s, respectively.*

Transverse T1-weighted images and corresponding series of diffusion weighted images were recorded in six volunteers. Fig. 2 shows a transverse T1-weighted image of the lower leg (Fig. 2a) of a 43 year-old male volunteer (#2 in Table 1) and according ADC maps determined from the diffusion weighted images with diffusion sensitizing along three orthogonal directions (Fig. 2b-d). While ADC values of tibial bone marrow fat appear rather homogeneous, some regions in the subcutaneous adipose tissue reveal higher ADC values, partly depending on the direction of the diffusion gradients. Fig. 3 shows semilogarithmic plots of the signal decay against the b-value from ROIs within yellow tibial bone marrow of the same volunteer for all three diffusion directions. Solid lines show the monoexponential fits to the data, yielding diffusion coefficients of $(1.69 \pm 0.11) \times 10^{-5}$ mm^2/s, $(1.86 \pm 0.13) \times 10^{-5}$ mm^2/s and $(1.81 \pm 0.16) \times 10^{-5}$ mm^2/s, respectively. For the diffusion directions perpendicular to the static magnetic field, b-value dependent signal decays in bone marrow were nearly perfectly fitting monoexponential functions. Data with the diffusion sensitizing gradient along the static field B_0 were more scattered around the mono-exponential fit, especially for higher b-values. The finding of more pronounced scattering of the data for diffusion weighting along the magnet axis could be observed for all volunteers. One possible explanation for this observation may be the fact that the table of the scanner has more play along the scanner axis than in perpendicular direction. Therefore, vibrations of the table during application of the diffusion gradients may lead to additional axial movements of the volunteer's trunk, which are transferred to the lower leg. With diffusion encoding along the z-direction, this may lead to a more pronounced scattering of data for higher b-values. However, these supplemental motions seem to be too weak to significantly increase the derived mean ADC values for diffusion sensitizing in z-direction in comparison to the perpendicular directions. Negligible diffusion anisotropy effects in bone marrow are indicated. Table 1 provides ADC values from tibial bone marrow of all volunteers for all diffusion directions.

Table 1: *ADC values of tibial yellow bone marrow for all subjects in units of $10^{-5}mm^2/s$: Mean values and standard deviation are given for diffusion sensitizing along orthogonal directions for a representative ROI. (The values in the second column denote the number of pixels.)*

Subject	ROI size	left-right	anterior-posterior	head-feet	mean
#1	32	1.95 ± 0.21	2.12 ± 0.28	2.28 ± 0.27	2.12 ± 0.17
#2	27	1.69 ± 0.11	1.86 ± 0.13	1.81 ± 0.16	1.79 ± 0.09
#3	30	1.72 ± 0.23	2.01 ± 0.25	2.04 ± 0.23	1.92 ± 0.18
#4	46	1.86 ± 0.12	1.98 ± 0.15	1.84 ± 0.13	1.89 ± 0.08
#5	21	1.76 ± 0.20	1.87 ± 0.15	2.01 ± 0.18	1.88 ± 0.13
#6	21	1.88 ± 0.19	1.91 ± 0.18	1.76 ± 0.11	1.85 ± 0.08
mean	30 ± 9	1.81 ± 0.10	1.96 ± 0.10	1.96 ± 0.20	1.91 ± 0.15

In contrast to the ADC values from tibial bone marrow, diffusion coefficients in subcutaneous adipose tissue showed a more heterogeneous behaviour. Diffusion coefficients in some subcutaneous adipose tissue areas were in the same range as in tibial bone marrow (Fig. 2). On the other hand, areas with distinctly higher ADC values up to 4.2×10^{-5} mm^2/s occurred. It should be mentioned that, especially in those regions with increased ADC values data presented low signal intensity and pronounced scattering around the fit curve for higher b-values.

4.4 Discussion and Conclusions

Since the apparent diffusion coefficients of fatty acids and triglycerides are about two orders of magnitude smaller than the diffusion coefficient of water, long-lasting diffusion gradients have to be applied to achieve sufficient diffusion related signal attenuation. For testing of the proposed methodical approach, substances with high molecular weight were employed for calibration purposes. Similar procedures were conducted in the earlier studies of Ababneh et al. [17] and Lehnert et al. [18]. ADC

values obtained in our phantom studies for 1-butanol and oleic acid are in good agreement with the results in [17] and [18]. Slight differences between ADC values for 1-butanol and oleic acid reported by Ababneh and Lehnert and the results in the present work can be explained by different temperatures of the fluids.

Diffusion maps revealing ADC values of fatty compartments in the lower leg show good quality and reasonable results. Fatty tibial bone marrow led to a mean ADC value of $(1.91 \pm 0.15) \times 10^{-5}$ mm^2/s with low variation within the cohort of 6 subjects. No significant dependence on the orientation of diffusion sensitizing gradients was found, indicating that there is no pronounced anisotropy in bone marrow tissue. Based on these consistent findings, the method is considered suitable for a precise determination of fat diffusion coefficients *in vivo*. Furthermore, the ADC values are very similar to the results of Ababneh et al., who measured fat diffusion coefficients in rat bone marrow.

As mentioned in the Results section, isolated regions in the subcutaneous adipose tissue show distinctly higher diffusion coefficients in comparison to the findings in tibial bone marrow. Assuming a rather homogeneous distribution of fat diffusion coefficients in both tibial bone marrow and subcutaneous adipose tissue, an accurate determination of ADC values in these regions may be hampered by not yet identified problems. One possible reason could be fibrous connective tissue or vessels causing pronounced field inhomogeneities and signal voids in their vicinity. Furthermore, phase shifts caused by incoherent motion could lead to additional signal attenuation for high b-values and therefore to overestimated ADC values. There are several possible sources for incoherent motion: First, pulsation in blood vessels located in or adjacent to the fat tissue. To constrain this effect, an additional diffusion measurement with electrocardiogram (ECG) triggering was accomplished for one volunteer. Measurements without ECG triggering and with ECG triggering with diffusion sensitizing in the diastole led to rather similar ADC maps, in contrast to a recent work of Brandejski et al. concerning spectroscopy-based diffusion mea-

surements of intramyocellular lipids [22]. Second, vibrations or small movements of the table due to forces present during gradient switching could lead to incoherent motion of tissue under examination. In an additional experiment, it was tried to decouple those small table movements due to gradient switching from the lower leg by hanging up the leg and fixing it on a hook, which should be not affected by motion problems of the table. However, no changes in the derived ADC maps could be obtained in comparison to the conventional bedding of the lower leg in the extremity coil.

High b-values up to 50000 s/mm^2 required very long TE of 240 ms for *in vivo* measurements. The maximal gradient strength on our 1.5 T MR system was restricted to 32.1 mT/m by the safety monitor of the scanner. However, due to the relatively long transverse relaxation time T2 of methylene signals from adipose tissue of about 90 ms [18], SNR was sufficient for an accurate calculation of ADC values. The relatively short longitudinal relaxation time T1 of methylene signals of approx. 300 ms [18] allows a short TR leading to a moderate total measurement time, despite several averages were recorded for each image in a series with 64 different b-values. If necessary, the total measurement can further be distinctly shortened to 6:29 min. or 3:17 min. by choosing only 32 or 16 b-values, respectively.

Restricted diffusion in the presence of impermeable barriers might lead to non-Gaussian diffusion characteristics, especially if long lasting diffusion gradients are applied. With a mean diffusion coefficient D = 2×10^{-5} mm^2/s for fat and a total diffusion time $T = \delta_1 + \delta_2 + \delta_3 + \delta_4 = 207.68$ ms, mean squared displacement $\left\langle z^2 \right\rangle = 2DT$ for a fat molecule in one direction is only about 3 μm, which is small compared to the mean size of fat vacuoles in adipocytes of white fat (size approx. 100 μm). For this reason, it can be assumed that diffusion in white adipose tissue is not restricted and the probability density of the displacements is Gaussian. Usual equations for calculating the b-values as used in Reese et al. [19] were applicable, and results

showed a linear reduction of signal intensity for increasing b-values on a logarithmic scale.

In contrast to the study of Ababneh et al., diffusion gradients were only applied in one orthogonal direction for each single measurement and not simultaneously along all three directions. Of course, using all three directions for diffusion weighting would lead to a distinctly shorter minimal TE of 170 ms for the same maximal b-value and therefore higher SNR. However, simultaneous application of gradients in y- and z-direction induces additional cross-term fields $G_y G_z yz/2B_0$ [23–25]. For the twice-refocused diffusion weighted spin-echo EPI sequence with long-lasting diffusion gradients and high amplitudes, these cross-terms lead to a net zero-order gradient moment, causing an echo shift in k-space and a signal loss in the image, especially for slices with an offset from the isocenter [26]. In our measurements, slice positions were chosen close to the isocenter, while an offset y_0 of 80 mm was necessary in phase direction. This effect, together with the relatively long echo time, could be the reason for distortions and signal losses in images with high b-values, when a tetrahedral encoding scheme was applied in some test measurements.

In Ababneh et al., it was postulated that diffusion preparation with stimulated-echo instead of spin-echo may be more adequate to achieve high b-values with sufficient SNR by keeping TE as short as possible to limit T2 decay signal loss with clinical scanners. Indeed, it can be shown that for water diffusion in skeletal muscle, signal yield will be higher for a stimulated echo in comparison to the twice-refocused spin-echo technique used in this work [27]. However, the optimal choice for diffusion preparation with minimum relaxation dependent signal losses depends on the ratio of T1 to T2 of the examined tissue [28]. While for water in musculoskeletal tissues with a high ratio T1/T2, stimulated echo is more advantageous, the situation for fat is distinctly different: Due to the relatively long T2 and the rather short T1 of main fat signals (T2 = 90 ms and T1 = 300 ms for the methylene [18] and T2 = 170 ms and T1 = 500 ms for the methyl signals [29]), spin echo preparation is superior

even for b-values as high as 50000 s^2/mm. In this case, optimized values for the stimulated echo would be echo time TE = 170 ms and mixing time TM = 130 ms for the methylene signals and TE = 175 ms and TM = 115 ms for the methyl signals. When compared to the spin-echo preparation, optimal stimulated echo preparation would lead to 30% and 40% less signal yield, respectively.

It may be worthwhile to examine diffusion of adipose tissue in other regions of the human body, for example of subcutaneous and/or visceral adipose tissue in abdomen or thorax. However, due to the more pronounced field inhomogeneities in these body regions in comparison to the extremities, single-shot EPI may not be the adequate tool for diffusion weighted imaging and the LSDI technique [15–17] may be a suitable alternative in this case.

The presented experiments show that MR imaging of diffusion in adipose tissue *in vivo* is feasible in relatively short measuring time and one may ask, whether there is any motivation for investigations into diffusion properties of fatty tissue. However, several potential applications of those measurements show up at the horizon:

First, temperature measurements in fatty tissue: Usual temperature measurement based on the temperature dependent shift of the water resonance is not applicable on fatty tissue. On the other hand, size and molecular weight of triglycerides inside fatty tissue can be expected to be rather constant. So, temperature can be considered as main determinant of measured ADC values. Diffusion of lipids could be a potential indicator of temperature inside the body for example during hyperthermia, if current problems with physiological movements or movements generated by the MR scanner are overcome.

Second, assessment of the share of triglycerides and fatty acids in adipose tissue: Fatty acids and triglycerides play an important role in metabolism. It is well known that storage of fat (mainly as triglycerides in the large vacuoles of white adipocytes) and transportation of fat (mainly as fatty acids in blood and through the cytoplasm)

are of interest for studies in subjects with diseases as type 2 diabetes or obesity. The molecular weight of free fatty acids is roughly one third of the molecular weight of triglycerides, resulting in faster diffusion of fatty acids. In cases with very high lipolysis in adipose tissue one might expect an increased fraction of free fatty acids inside the cells and potentially a second component visible in the b-value dependent diffusion signal curve.

Third: Differentiation of brown versus white adipose tissue: In recent publications [30–32] it was reported that the amount of brown fat in humans is higher than assumed before, and the amount (and/or activity) of brown fat is reduced in subjects with obesity. Therefore, the amount of brown adipose tissue may be of importance for normal human physiology and a target for the research on obesity and diabetes. The lipid vacuoles in (plurivacuolar) brown fat are clearly smaller than in (monovacuolar) white fat. Therefore, lipid diffusion could be different in the small vacuoles of brown cells compared to the clearly larger vacuoles in white cells.

Fourth: Differentiation of microvesical versus macrovesical steatosis of the liver: Lipids can be stored in liver parenchyma in vesicles of different size inside hepatocytes. In patients with steatosis, fat fraction can be clearly higher than 10% and diffusion measurement of lipids by MR could get feasible. Nowadays only histology allows distinguishing macrovesicular and microvesicular steatosis. This distinction is clinically important. Fat selective MRI or MRS can only determine the total fat fraction, but not the microscopic distribution. Movement of lipids in very small vesicles is expected to be more restricted, but the vesicles themselves might be able to move inside the cytoplasm of the hepatocytes. Measuring diffusion properties of those hepatic lipids, which is more demanding than in pure adipose tissue, could lead to clinically interesting results.

Fifth: Mobility and spatial distribution of intramyocellular lipids: A further example for restricted diffusion probably occurs for intramyocellular lipids, which are settled as little droplets with a diameter of clearly less than 1 μm in close apposi-

tion to mitochondria in the cytoplasm of myocytes [33]. Analysis of the size of the droplets and their mobility inside the cytoplasm is interesting, since their availability for oxidation seems to be individually variable. The volume share of lipids within myocytes is often less than one per cent. Therefore, the low signal-to-noise ratio is really challenging and needs further methodical development to obtain increased sensitivity for reliable diffusion measurements.

All those possible applications of lipid diffusion measurements are still speculative, but have currently no suitable non-invasive 'competitors' in terms of providing similar diagnostic information. The diagnostic information is usually only available using biopsies or by implantation of probes (e.g., for temperature measurements). Altogether, there are several areas of motivation for measuring diffusion of lipids in adipose tissues or in fatty compartments of organs as liver and musculature.

References

[1] Le Bihan, D., R. Turner and J.R. Macfall: *Effects of intravoxel incoherent motions (IVIM) in steady-state free precession (SSFP) imaging: application to molecular diffusion imaging*. Magn. Reson. Med., 10:324–337, 1989.

[2] Müller, M.F., P.V. Prasad, B. Siewert and R.R. Edelman: *The* in-vivo *diffusion measurements of the liver, kidneys, spleen and m. erector with an echo-planar imaging system in normal subjects*. Rofo. Fortschr. Geb. Rontgenstr. Neuen. Bildgeb. Verfahr., 161(3):233–236, 1994.

[3] Müller, M.F., P.V. Prasad, D. Bimmler, A. Kaiser and R.R. Edelman: *Functional imaging of the kidney by means of measurement of the apparent diffusion coefficient*. Radiology, 193(3):711–715, 1994.

[4] Dietrich, O., J.G. Raya, J. Sommer, M. Deimling, M.F. Reiser and A. Baur-Melnyk: *A comparative evaluation of a RARE-based single-shot pulse se-*

quence for diffusion-weighted MRI of musculoskeletal soft-tissue tumors. Eur. Radiol., 15:772–783, 2005.

[5] Pierpaoli, C., P. Jezzard, P.J. Basser, A. Barnett and G. Di Chiro: *Diffusion tensor MR imaging of the human brain*. Radiology, 201:637–648, 1996.

[6] Reese, T.G., R.M. Weisskoff, R.N. Smith, R. Rosen, R.E. Dinsmore and J. van Wedeen: *Imaging myocardial fiber architecture* in vivo *with magnetic resonance*. Magn. Reson. Med., 34:786–791, 1995.

[7] Doorn, A. van, P.H. Bovendeerd, K. Nicolay, M.R. Drost and J.D. Janssen: *Determination of muscle fiber orientation using diffusion weighted MRI*. Eur. J Morphol., 34:5–10, 1996.

[8] Ries, M., R.A. Jones, F. Basseau, C.T.W. Moonen and N. Grenier: *Diffusion tensor MRI of the human kidney*. J. Magn. Reson. Imaging, 14:42–49, 2001.

[9] Sinha, U. and L. Yao: In vivo *diffusion tensor imaging of human calf muscle*. J. Magn. Reson. Imaging, 15:87–95, 2002.

[10] Sinha, S. and U. Sinha: In vivo *diffusion tensor imaging of human prostate*. Magn. Reson. Med., 52:530–537, 2004.

[11] Gilbert, R.J. and V.J. Napadow: *Three-dimensional muscular architecture of the human tongue determined in vivo with diffusion tensor magnetic resonance imaging*. Dysphagia, 20:1–7, 2005.

[12] Meder, R., S.K. de Visser, J.C. Bowden, T. Bostrom and J.M. Pope: *Diffusion tensor imaging of articular cartilage as a measure of tissue architecture*. Osteoarthr. Cartil., 14:875–881, 2006.

[13] Posse, S., C.A. Cuenod and D. Le Bihan: *Human brain: proton diffusion MR spectroscopy*. Radiology, 188:719–725, 1993.

[14] Boden, G.: *Free fatty acids, insulin resistance, and type 2 diabetes mellitus*. Proc. Assoc. Am. Physicians, 111:241–248, 1999.

[15] Gudbjartsson, H., S.E. Maier, R.V. Mulkern, I.A. Morocz, S. Patz and F.A. Jolesz: *Line scan diffusion imaging*. Magn. Reson. Med., 36:509–518, 1996.

[16] Mulkern, R.V., H. Gudbjartsson, C.-F. Westin, H.P. Zengingonul, W. Gartner, C.R.G. Guttmann, R.L. Robertson, W. Kyriakos, R. Schwartz, D. Holtzman and F.A. Jolesz: *Multi-component apparent diffusion coefficients in human brain*. NMR Biomed., 12:51–62, 1999.

[17] Ababneh, Z.Q., H. Beloeil, C.B. Berde, A.M. Ababneh, S.E. Maier and R.V. Mulkern: *In vivo lipid diffusion coefficient measurements in rat bone marrow*. Magn. Reson. Imaging, 27:859–864, 2009.

[18] Lehnert, A., J. Machann, G. Helms, C.D. Claussen and F. Schick: *Diffusion characteristics of large molecules assessed by proton MRS on a whole body MR system*. Magn. Reson. Imaging, 22:39–46, 2004.

[19] Reese, T.G., O. Heid, R.M. Weisskoff and V.J. Wedeen: *Reduction of eddy-current-induced distortion in diffusion MRI using a twice-refocused spin echo*. Magn. Reson. Med., 49:177–182, 2003.

[20] Gudbjartsson, H. and S. Patz: *The Rician distribution of noisy MRI data*. Magn. Reson. Med., 34:910–914, 1995.

[21] Sijbers, J., A.J. den Dekker, E. Raman and D. van Dyck: *Parameter estimation from magnitude MR images*. Int. J. Imag. Syst. Tech., 10:109–114, 1999.

[22] Brandejsky, V., R. Kreis and C. Boesch: *Optimization of spectroscopy-based measurements of intramyocellular lipids*. In proceedings of the Joint Annual Meeting of ISMRM-ESMRMB, page 855, 2010.

[23] Bernstein, M.A., X.J. Zhou, J.A. Polzin, K.F. King, A. Ganin, N.J. Pelc and G.H. Glover: *Concomitant gradient terms in phase contrast MR: analysis and correction*. Magn. Reson. Med., 39:300–308, 1998.

[24] Zhou, X.J., Y.P. Du, M.A. Bernstein, H.G. Reynolds, J.K. Maier and J.A. Polzin: *Concomitant magnetic-field-induced artifacts in axial echo planar imaging*. Magn. Reson. Med., 39:596–605, 1998.

[25] Du, Y.P., X.J. Zhou and M.A. Bernstein: *Correction of concomitant magnetic field-induced image artifacts in nonaxial echo-planar imaging*. Magn. Reson. Med., 48:509–515, 2002.

[26] Meier, C., M. Zwanger, T. Feiweier and D. Porter: *Concomitant Field Terms for Asymmetric Gradient Coils: Consequences for Diffusion, Flow, and Echo-Planar Imaging*. Magn. Reson. Med., 60:128–134, 2008.

[27] Steidle, G. and F. Schick: *Echoplanar diffusion tensor imaging of the lower leg musculature using eddy current nulled stimulated echo preparation*. Magn. Reson. Med., 55:541–548, 2006.

[28] Schick, F.: *Signal losses in diffusion preparation: Comparison between spin-echo, stimulated echo and SEASON*. Magn. Reson Mater. Phy. (MAGMA), 6:53–61, 1998.

[29] Schick, F., B. Eismann, W.-I. Jung, H. Bongers, M. Bunse and O. Lutz: *Comparison of localized proton NMR signals of sceletal muscle and fat tissue* in vivo. Magn. Reson. Med., 29:158–167, 1993.

[30] Nedergaard, J., T. Bengtsson and B. Cannon: *Unexpected evidence for active brown adipose tissue in adult humans*. Am. J. Physiol. Endocrinol. Metab., 293:E444–E452, 2007.

[31] van Marken Lichtenbelt, W.D., J.W. Vanhommerig, N.M. Smulders, J. Drossaerts, G.J. Kemerink, N.D. Bouvy, P. Schrauwen and J. Teule: *Cold-*

activated brown adipose tissue in healthy men. N. Engl. J. Med., 360:1500–1508, 2009.

[32] Pfannenberg, C., M.K. Werner, S. Ripkens, I. Stef, A. Deckert, M. Schmadl, M. Reimold, H.-U. Häring, C.D. Claussen and N. Stefan: *Impact of age on the relationships of brown adipose tissue with sex and adiposity in humans*. Diabetes, 59:1789–1793, 2010.

[33] Boesch, C., J. Slotboom, H. Hoppeler and R. Kreis: *In vivo determination of intramyocellular lipids in human muscle by means of localized ^{1}H-MR-spectroscopy*. Magn. Reson. Med., 37:484–493, 1997.

5 General Discussion

Magnetic resonance imaging is a powerful tool for non-invasively mapping of characteristics of internal structures of biological objects. Manifold possibilities exist for creating suitable contrast between different soft tissues in the human body. Besides basic MRI techniques using spin density or relaxation properties of examined tissues, special techniques being sensitive to incoherent motion or self diffusion of water molecules are used to indirectly gain information about microstructure of tissue, which hinders or restricts free motion of water molecules. Most applications of MR diffusion imaging focus on diagnosis of non-oncological pathologies as for example liver fibrosis or liver cirrhosis, but it can also be applied for tumour staging and grading. Advanced diffusion tensor imaging is mostly used in brain to monitor nerve fibres in white matter tissue. Besides MR imaging, *in vivo* MR spectroscopy gains more and more importance as additional tool in metabolic studies. Within the scope of this thesis, new MR scan methods were developed providing more precise information about geometrical micro-architecture or physiological composition of skeletal muscle and of fat tissue.

The first method described in Chapter 2 concerns the determination of the magnetic field distribution of intra- and extramyocellular lipids out of MR spectra by deconvolution. Amount of IMCL is an important indicator in physiological and pathological lipid metabolism in skeletal musculature and, therefore, an accurate determination with high reproducibility is important. Deconvolution allows a more precise identification of IMCL quantity in comparison to standard fitting routines, especially due to the fact that the magnetic field distribution of EMCL can show a rather asymmetrical lineshape not covered by common fitting routines with fixed lineshapes.

In Chapter 3, a new method was implemented for diffusion tensor imaging in skeletal musculature with optimized signal-to-noise ratio and a significant reduction of

eddy current related image distortions. Although MR diffusion tensor imaging was restricted to the lower leg in this study, application of this method to skeletal musculature in other human body regions is possible.

In Chapter 4, a first attempt to measure fat diffusion in human tissue by echo planar MRI was waged. Possible application may be an alternative method to separate IMCL and EMCL by a more restricted diffusion of IMCL in the little fat droplets inside muscle cells, since basic fat MRI is not capable to distinguish between IMCL and EMCL.

A continuing development of MR scanners and RF coil techniques by the manufacturers and the use of higher magnetic fields increasing signal-to-noise ratio may be a fertile soil for further efforts in MR research to augment the state of knowledge in radiological diagnosis.

Appendix[†]

Table A: *The apparent diffusion coefficients (ADC) [$\times 10^{-3}$ mm^2/s] calculated as trace of the diffusion tensor divided by three, the eigenvalues λ_1, λ_2 and λ_3 [$\times 10^{-3}$ mm^2/s] of the diffusion tensor and the T2 values [ms] of the four subjects (Sub), for the muscles gastrocnemius medialis (GM), gastrocnemius lateralis (GL), soleus (SOL) and tibialis (TA). The ADC value was lowest in GL and highest in SOL for all subjects. These deviations between GL and SOL are based on a distinctly low eigenvalue λ_3 in GM and a distinctly high eigenvalue λ_2 in SOL. After workload, diffusion values increased most significantly in GM for all four subjects, whereas in the TA no significant changes could be observed.*

		GM				
Sub	load	ADC	λ_1	λ_2	λ_3	T2
#1	before	1.49 ± 0.04	2.10 ± 0.06	1.31 ± 0.04	1.11 ± 0.04	48.3 ± 2.4
	after	1.57 ± 0.02	2.19 ± 0.04	1.39 ± 0.03	1.19 ± 0.03	58.8 ± 2.7
#2	before	1.38 ± 0.03	1.74 ± 0.08	1.29 ± 0.04	1.13 ± 0.09	44.5 ± 2.0
	after	1.43 ± 0.02	1.79 ± 0.04	1.35 ± 0.03	1.17 ± 0.03	48.8 ± 3.1
#3	before	1.31 ± 0.05	1.87 ± 0.10	1.13 ± 0.05	0.99 ± 0.03	40.6 ± 2.2
	after	1.41 ± 0.03	2.01 ± 0.05	1.24 ± 0.02	1.02 ± 0.05	48.8 ± 2.5
#4	before	1.30 ± 0.04	1.76 ± 0.05	1.19 ± 0.08	0.99 ± 0.05	42.0 ± 2.5
	after	1.45 ± 0.02	2.10 ± 0.18	1.32 ± 0.05	0.98 ± 0.14	49.0 ± 2.5
mean	before	1.37 ± 0.09	1.87 ± 0.17	1.23 ± 0.08	1.01 ± 0.08	43.9 ± 3.4
	after	1.47 ± 0.07	2.02 ± 0.17	1.33 ± 0.06	1.09 ± 0.10	51.4 ± 5.0

Table A – continued on next page

[†]See subsection 3.3.3.

Table A – continued from previous page

GL

Sub	load	ADC	λ_1	λ_2	λ_3	T2
#1	before	1.35 ± 0.04	2.00 ± 0.04	1.32 ± 0.04	0.75 ± 0.08	48.6 ± 6.7
	after	1.51 ± 0.02	2.08 ± 0.07	1.41 ± 0.06	1.08 ± 0.04	55.1 ± 7.0
#2	before	1.33 ± 0.03	1.83 ± 0.07	1.24 ± 0.04	0.96 ± 0.03	42.7 ± 2.9
	after	1.40 ± 0.02	1.90 ± 0.03	1.26 ± 0.03	1.07 ± 0.04	48.2 ± 10.1
#3	before	1.26 ± 0.05	1.78 ± 0.04	1.18 ± 0.04	0.86 ± 0.05	38.4 ± 2.7
	after	1.36 ± 0.03	1.94 ± 0.05	1.19 ± 0.05	0.99 ± 0.04	46.5 ± 3.3
#4	before	1.24 ± 0.04	1.77 ± 0.05	1.11 ± 0.06	0.87 ± 0.05	37.2 ± 6.9
	after	1.42 ± 0.02	2.11 ± 0.25	1.29 ± 0.04	0.91 ± 0.17	46.4 ± 3.1
mean	before	1.30 ± 0.09	1.85 ± 0.11	1.21 ± 0.09	0.86 ± 0.09	41.7 ± 5.2
	after	1.42 ± 0.07	2.01 ± 0.10	1.29 ± 0.09	1.01 ± 0.08	49.0 ± 4.1

SOL

Sub	load	ADC	λ_1	λ_2	λ_3	T2
#1	before	1.50 ± 0.04	1.98 ± 0.12	1.57 ± 0.09	1.00 ± 0.05	40.9 ± 1.2
	after	1.81 ± 0.04	2.16 ± 0.10	1.88 ± 0.06	1.44 ± 0.04	50.7 ± 1.9
#2	before	1.40 ± 0.03	1.87 ± 0.06	1.33 ± 0.06	1.04 ± 0.04	44.5 ± 3.6
	after	1.47 ± 0.02	1.96 ± 0.05	1.37 ± 0.06	1.11 ± 0.05	48.8 ± 5.1
#3	before	1.42 ± 0.03	1.77 ± 0.07	1.40 ± 0.07	1.11 ± 0.05	41.5 ± 2.2
	after	1.44 ± 0.03	1.90 ± 0.05	1.34 ± 0.04	1.11 ± 0.05	47.1 ± 7.6
#4	before	1.38 ± 0.03	1.94 ± 0.04	1.24 ± 0.04	0.98 ± 0.05	43.2 ± 1.6
	after	1.49 ± 0.02	2.11 ± 0.08	1.42 ± 0.07	0.98 ± 0.04	49.8 ± 2.4
mean	before	1.43 ± 0.05	1.89 ± 0.09	1.39 ± 0.14	1.03 ± 0.06	42.5 ± 1.6
	after	1.55 ± 0.17	2.03 ± 0.12	1.50 ± 0.25	1.16 ± 0.20	49.1 ± 1.5

Table A – continued on next page

Table A – continued from previous page

TA

Sub	load	ADC	λ_1	λ_2	λ_3	T2
#1	before	1.41 ± 0.03	1.97 ± 0.05	1.28 ± 0.06	1.02 ± 0.06	42.2 ± 3.8
	after	1.43 ± 0.04	1.96 ± 0.08	1.32 ± 0.05	1.02 ± 0.05	42.3 ± 5.7
#2	before	1.39 ± 0.04	1.87 ± 0.09	1.30 ± 0.06	1.02 ± 0.07	46.8 ± 7.0
	after	1.37 ± 0.03	1.91 ± 0.05	1.27 ± 0.06	0.97 ± 0.07	43.2 ± 6.6
#3	before	1.36 ± 0.03	1.94 ± 0.14	1.21 ± 0.03	0.97 ± 0.04	38.5 ± 1.8
	after	1.41 ± 0.01	2.01 ± 0.04	1.25 ± 0.04	1.01 ± 0.03	40.6 ± 2.8
#4	before	1.38 ± 0.02	2.02 ± 0.06	1.19 ± 0.05	0.98 ± 0.04	40.0 ± 4.4
	after	1.39 ± 0.02	1.97 ± 0.07	1.22 ± 0.06	1.00 ± 0.03	39.2 ± 1.6
mean	before	1.39 ± 0.02	1.95 ± 0.06	1.25 ± 0.05	1.00 ± 0.03	41.9 ± 3.6
	after	1.40 ± 0.03	1.96 ± 0.04	1.27 ± 0.04	1.00 ± 0.02	41.3 ± 1.8

List of Publications

International Journals

[P1] Eibofner, F., **G. Steidle**, R. Kehlbach, R. Bantleon and F. Schick: *Utilizing echo-shifts in k-space for generation of positive contrast in areas with marked susceptibility alterations*. Magn. Reson. Med., 2011. doi: 10.1002/mrm.24133.

[P2] Werz, K., H. Braun, D. Vitha, G. Bruno, P. Martirosian, **G. Steidle** and F. Schick: *Relaxation times T1, T2, and T2* of apples, pears, citrus fruits, and potatoes with a comparison to human tissues*. Z. Med. Phys., 21:206–215, 2011.

[P3] Springer, F., **G. Steidle**, P. Martirosian, R. Syha, C.D. Claussen and F. Schick: *Rapid assessment of longitudinal relaxation time in materials and tissues with extremely fast signal decay using UTE sequences and variable flip angle method*. Invest. Radiol., 46(10):610–617, 2011.

[P4] **Steidle, G.**, F. Eibofner and F. Schick: *Quantitative diffusion imaging of adipose tissue in the human lower leg at 1.5 T*. Magn. Reson. Med., 65(4):1118–1124, 2011.

[P5] Springer, F., **G. Steidle**, P. Martirosian, C.D. Claussen and F. Schick: *Effects of in-pulse transverse relaxation in 3D ultrashort echo time sequences: Analytical derivation, comparison to numerical simulation and experimental application at 3T*. J. Magn. Reson., 206(1):88–96, 2010.

[P6] Schwenzer, N., **G. Steidle**, P. Martirosian, C. Schraml, F. Springer, C.D. Claussen and F. Schick: *Diffusion tensor imaging of the human calf muscle: distinct changes in fractional anisotropy and mean diffusion due to passive muscle shortening and stretching*. NMR Biomed., 22(10):1047–1053, 2009.

[P7] Schwenzer, N., P. Martirosian, J. Machann, C. Schraml, **G. Steidle**, C.D. Claussen and F. Schick: *Aging effects on human calf muscle properties assessed by MRI at 3 Tesla.* J. Magn. Reson. Imaging, 29(6):1346–1354, 2009.

[P8] Rossi, C., A. Boss, P. Martirosian, **G. Steidle**, S. Capuani, C.D. Claussen, B. Maraviglia and F. Schick: *Influence of steady background gradients on the accuracy of molecular diffusion anisotropy measurements*. Magn. Reson. Imaging, 26:1250–1258, 2008.

[P9] Ludescher, B., J. Effelsberg, P. Martirosian, **G. Steidle**, B. Markert, C.D. Claussen and F. Schick: *T2- and diffusion-maps reveal diurnal changes of intervertebral disc composition: an in vivo MRI study at 1.5 Tesla*. J. Magn. Reson. Imaging, 28:252–257, 2008.

[P10] Rossi, C., A. Boss, **G. Steidle**, P. Martirosian, U. Klose, S. Capuani, B. Maraviglia, C.D. Claussen and F. Schick: *Water diffusion anisotropy in white and gray matter of the human spinal cord*. J. Magn. Reson. Imaging, 27:476–482, 2008.

[P11] Graf, H., **G. Steidle** and F. Schick: *Heating of metallic implants and instruments induced by gradient switching in a 1.5 Tesla whole-body unit*. J. Magn. Reson. Imaging, 26:1328–1333, 2007.

[P12] Rossi, C., A. Boss, T.M. Lindig, P. Martirosian, **G. Steidle**, W. Mätzler, C.D. Claussen, U. Klose and F. Schick: *Diffusion tensor imaging of the spinal cord at 1.5 and 3.0 Tesla*. Rofo. Fortschr. Geb. Rontgenstr. Neuen. Bildgeb. Verfahr., 179:219–224, 2007.

[P13] **Steidle, G.** and F. Schick: *Echoplanar diffusion tensor imaging of the lower leg musculature using eddy current nulled stimulated echo preparation*. Magn. Reson. Med., 55:541–548, 2006.

[P14] GRAF, H., **G. Steidle**, P. MARTIROSIAN, U. LAUER and F. SCHICK: *Effects on MRI due to altered rf polarization near conductive implants of instruments*. Med. Phys., 33:124–127, 2006.

[P15] GRAF, H., **G. Steidle**, P. MARTIROSIAN, U. LAUER and F. SCHICK: *Metal artifacts caused by gradient switching*. Magn. Reson. Med., 54:231–234, 2005.

[P16] GRAF, H., **G. Steidle**, U. LAUER and F. SCHICK: *Rf enhancement and shielding in MRI caused by conductive implants: Dependence on electrical parameters for a tube model*. Med. Phys., 32:337–242, 2005.

[P17] MÜLLER-BIERL, B., H. GRAF, **G. Steidle** and F. SCHICK: *Compensation of magnetic field distortions from paramagnetic instruments by added diamagnetic material: Measurements and numerical simulations*. Med. Phys., 32:76–84, 2005.

[P18] **Steidle, G.**, J. SCHÄFER, H.P. SCHLEMMER, C.D. CLAUSSEN and F. SCHICK: *Two-dimensional parallel acquisition technique in 3D MR colonography*. Rofo. Fortschr. Geb. Rontgenstr. Neuen. Bildgeb. Verfahr., 176:1100–1105, 2004.

[P19] **Steidle, G.**, H. GRAF and F. SCHICK: *Sodium 3-D MRI of the human torso using a volume coil*. Magn. Reson. Imaging, 22(2):171–180, 2004.

[P20] MÜLLER-BIERL, B., H. GRAF, U. LAUER, **G. Steidle** and F. SCHICK: *Numerical modeling of needle tip artifacts in MR gradient echo imaging*. Med. Phys., 31:579–587, 2004.

[P21] MACHANN, J., **G. Steidle**, C. THAMER, I. MADER and F. SCHICK: *In vivo proton NMR studies in skeletal musculature*. Ann. Rep. NMR Spect., 50:1–74, 2003.

[P22] **Steidle, G.**, J. MACHANN, C.D. CLAUSSEN and F. SCHICK: *Separation of intra- and extramyocellular lipid signals in proton MR-spectra by determination of their magnetic field distribution*. J. Magn. Reson., 154:228–235, 2002.

Conference Proceedings

[A1] **Steidle, G.** and F. Schick: *Pulsed-gradient spin-echo magnetic resonance imaging of restricted diffusion between reflecting parallel walls at a whole body scanner*. On CD of 26th Annual Scientific Meeting of the ESMRMB electronic supplement to Magn Reson Mater Phy (MAGMA), 2009. DOI: 10.1007/s10334-009-0178-y.

[A2] **Steidle, G.** and F. Schick: *Diffusion tensor magnetic resonance imaging of the lower leg musculature during exercise*. On CD of 25th Annual Scientific Meeting of the ESMRMB electronic supplement to Magn Reson Mater Phy (MAGMA), 2008. DOI: 10.1007/s10334-008-0126-2.

[A3] **Steidle, G.** and F. Schick: *Diffusion tensor imaging of the kidney with a single-shot TSE sequence*. On CD of 22th Annual Scientific Meeting of the ESMRMB electronic supplement to Magn Reson Mater Phy (MAGMA), 2005. DOI: 10.1007/s10334-005-0116-6.

[A4] **Steidle, G.**, C.D. Claussen and F. Schick: *In-vivo-Diffusionsmessungen in der menschlichen Unterschenkelmuskulatur vor und nach Belastung*. Fortschr. Röntgenstr., 177 Suppl.:323, 2005.

[A5] **Steidle, G.**, M. Lichy and F. Schick: *Eliminierung von Wirbelstrom-Effekten in einer diffusionsgewichteten STEAM-EPI Sequenz*. Fortschr. Röntgenstr., 177 Suppl.:456, 2005.

[A6] **Steidle, G.** and F. Schick: *Eddy current-nulled diffusion tensor imaging by a STEAM-EPI sequence at 3.0 Tesla*. in Abstract Book of the RSNA: 90th Scientific Assembly and Annual Meeting, 188, 2004.

[A7] **Steidle, G.**, J. Schäfer, H.P. Schlemmer, C.D. Claussen and F. Schick: *3D MR Colonography using two-dimensional parallel acquisition technique*. On

CD of 21th Annual Scientific Meeting of the ESMRMB electronic supplement to Magn Reson Mater Phy (MAGMA), 2004.

[A8] **Steidle, G.**, G. HELMS and F. SCHICK: *Minimization of eddy current artifacts in diffusion tensor imaging by a STEAM-EPI sequence at 3.0 Tesla*. Proc. Intl. Soc. Mag. Reson. Med., 2004.

[A9] **Steidle, G.** and F. SCHICK: *Reduction of eddy current artifacts in echo planar diffusion tensor imaging with a stimulated echo preparation*. Eur. Radiology, 14 Suppl. 2:518, 2004. C-871.

[A10] **Steidle, G.**, J. MACHANN, F. SCHICK and C.D. CLAUSSEN: *Quantification of lipids in 1H MR spectra recorded at 3.0 T? Improvements in metabolic studies*. Eur. Radiology, 14 Suppl. 2:518, 2004. C-871.

[A11] **Steidle, G.** and F. SCHICK: *Eddy current-nulled diffusion tensor imaging by a STEAM-EPI sequence*. Magn Reson Mater Phy (MAGMA), 16 Suppl. 1:276, 2003.

[A12] **Steidle, G.** and F. SCHICK: *Eliminierung von Wirbelstrom-Effekten in einer diffusionsgewichteten STEAM-EPI Sequenz.* in Abstract Book: 34. Jahrestagung der Deutschen Gesellschaft für Medizinische Physik (DGMP), page 360, 2003.

[A13] **Steidle, G.**, H. GRAF and F. SCHICK: *3D MR imaging of sodium by using a volume coil*. Proc. Intl. Soc. Mag. Reson. Med., page 2436, 2003.

[A14] **Steidle, G.**, H. GRAF, C.D. CLAUSSEN and F. SCHICK: *3D MR Bildgebung von Natrium unter Verwendung einer Volumenspule*. Fortschr. Röntgenstr., 175:269, 2003.

[A15] **Steidle, G.**, H. GRAF, F. SCHICK and C.D. CLAUSSEN: *Comparison and optimization of 3D gradient echo technique in MR imaging for visualization of extracellular sodium*. Eur. Radiology, 13 Suppl. 1:541, 2003. C-0940.

[A16] **Steidle, G.**, H. Graf and F. Schick: *Comparison and optimization of 3D gradient echo technique in MR imaging for visualization of extracellular sodium*. Magn. Reson. Mater. Phy. (MAGMA), 15 Suppl. 1:213, 2002.

[A17] **Steidle, G.**, J. Machann, K. Brechtel, C.D. Claussen and F. Schick: *Regional differences of the magnetic field distribution of IMCL and EMCL signals from human calf muscles*. Proc. Intl. Soc. Mag. Reson. Med., page 1073, 2001.

[A18] **Steidle, G.**, K. Brechtel, A. Niess, S. Jacob, J. Machann, H.U. Häring, H.H. Dickhuth, C.D. Claussen and F. Schick: *1H-MR-spectroscopy of intramyocellular lipids (IMCL) in calf musculature of well trained male runners during exercise*. Magn. Reson. Mater. Phy. (MAGMA), 11 Suppl. 1:271, 2000.

[A19] **Steidle, G.**, J. Machann, C.D. Claussen and F. Schick: *Differentiation of IMCL and EMCL signals in spectra from human calf muscles by deconvolution and determination of the magnetic field distribution*. Magn. Reson. Mater. Phy. (MAGMA), 11 Suppl. 1:82, 2000.

Danksagungen

Mein ganz besonderer Dank gilt Prof. Dr. Dr. Fritz Schick. Er hat mich stets in inspirierender und motivierender Weise unterstützt und hatte immer ein offenes Ohr für all meine Fragen und auftretenden Probleme bei der Erstellung dieser Arbeit.

Allen anderen Mitarbeiterinnen und Mitarbeitern der Sektion für Experimentelle Radiologie – insbesondere Dr. Hansjörg Graf, Dr. Jürgen Machann, Dr. Petros Martirosian und Frank Eibofner – ein herzliches Dankeschön für das hervorragende, kollegiale und freundschaftliche Arbeitsklima und die vielen, fruchtbaren und hilfreichen Anregungen, Ratschläge und Diskussionen.

Auch für die Bereitschaft meiner Bekannten und Freunde sich regelmäßig als Probanden für die Messungen an den Kernspintomographen zur Verfügung zu stellen, kann ich nicht genug danken.

Ohne die nicht nur in finanzieller Hinsicht tatkräftige Unterstützung durch meine Eltern und meine Geschwister, wäre ich nicht in der Lage gewesen, mein Studium erfolgreich abzuschließen und damit die notwendigen Voraussetzungen für diese Dissertation zu schaffen. Ihnen gilt mein ganz besonderer Dank.

Ganz lieben Dank an Angie.

ﻢﻜﺣ ﻪﻠﻟﺍﺪﺒﻟﺍ ﺎﻘﺣ ﻞﻟ ﻢﻜﺣ

Curriculum Vitae

Name:	Günter Steidle
geboren:	am 05. Oktober 1966 in Balingen, Zollernalbkreis
Schulausbildung:	
1973 – 77:	Grund- und Hauptschule in Nusplingen
1977 – 83:	Progymnasium in Meßstetten
1983 – 86:	Gymnasium in Albstadt-Ebingen
20. Juni 1986:	Allgemeine Hochschulreife
Studium	
10/1986 – 12/1993:	Studium der Physik an der Eberhard-Karls-Universität Tübingen
21. März 1989:	Vorprüfung in der Diplom-Prüfung in Physik
03/1992 – 09/1993:	Anfertigung der Diplomarbeit „Operatoralgebraische Quantenfeldtheorie der Josephson-Mikrowellenstrahlung“ am Institut für Theoretische Physik der Eberhard-Karls-Universität Tübingen
22. Dezember 1993:	Diplom in Physik
10/1997 – 09/1999:	Fernstudium an der Universität Kaiserslautern „Medizinische Physik und Technik“
22.08.1999:	Abschluss mit Universitätszertifikat
ab 04/2004:	Anfertigung der Dissertation in Physik mit dem Thema „Magnetic Resonance Techniques for Sensitive Assessment of Microscopic Properties of Muscular and Adipose Tissue“ bei Prof. Dr. Dr. Fritz Schick in der Sektion für Experimentelle Radiologie, Abteilung für Diagnostische und Interventionelle Radiologie, Universitätsklinikum Tübingen

Tätigkeiten:

04/1990 – 07/1993:	Wissenschaftliche Hilfskraft in der Lehre am mathematischen Institut der Eberhard-Karls-Universität Tübingen
01/1994 – 12/1999 :	Technischer Angestellter in der Abteilung Entwicklung und Konstruktion von Wintergärten bei der Firma Glasbau Wäschle in Meßstetten
ab 01/2000 :	Technischer Angestellter in der Abteilung für Diagnostische und Interventionelle Radiologie des Universitätsklinikums Tübingen

Meine akademischen Lehrer während des Physikstudiums waren:
Arendt, Baumann, Clement, Dittrich, Ebert, Fäßler, Gönnenwein, Herrmann, Hübener, Kasper, Kramer, Kümmerer, Lenz, Lichte, Lutz, Mack, Mathieu, Mertens, Rieckers, Schief, Strähle, Stumpf, Wagner, Wolff